Exciton Dynamics in Perfluoropentacene Single Crystals

Dissertation

zur Erlangung des Doktorgrades
der Naturwissenschaften
(Dr. rer. nat.)

dem Fachbereich Physik
der Philipps-Universität Marburg

vorgelegt von

Kolja Kolata

aus

Bremen

Marburg, 2014

Vom Fachbereich Physik der Philipps-Universität Marburg
als Dissertation angenommen am:

Erstgutachter:	PD Dr. S. Chatterjee
Zweitgutachter:	Prof. Dr. G. Witte

Tag der mündlichen Prüfung:

Für Phaedra

Inhaltsverzeichnis

Zusammenfassung

Seit der Herstellung des ersten funktionsfähigen Transistors im Jahre 1948 von Bardeen, Brattain und Shockley, hat die Halbleiterindustrie einen damals ungeahnten Siegeszug vollzogen. Heutzutage bilden Halbleiterbauelemente den Grundstein für fast jedes elektronische Gerät. Insbesondere der Computer, welcher den Alltag der Menschen revolutioniert hat, basiert vor allem auf Entwicklungen aus der Halbleiterforschung. Halbleiter werden nicht nur in Form von Schaltelementen in elektrischen Kreisen eingesetzt, sie besitzen auch sehr nützliche, optische Eigenschaften und kommen z.B. als Leuchtdioden (LEDs), als Laserdioden, als CCD[1]-Chips oder als Solarzellen in unserem täglichen Leben zum Einsatz.

Über Jahrzehnte lag der Fokus der Halbleiterforschung auf anorganische Materialsysteme, wobei Silizium einen exklusiven Part einnahm, aufgrund seiner bedeutsamen Stellung in der Mikroelektronik. In den letzten Jahren allerdings, wächst vermehrt der Anteil der Forchung an organischen Halbleitern. Vor allem die organischen LEDs (OLEDs) haben mitlerweile den Einzug in die kommerzielle Anwendung gefunden, und werden bevorzugt als Basis für Smartphone-Displays verwendet. Ihre Vorteile gegenüber LCDs[2] liegen dabei im Farbkontrast, sowie in der Biegsamkeit.

Andererseits, blieben Solarzellen auf Basis von organischen Halbleitern bisher ihre Praxistauglichkeit schuldig. Grundsätzlich bieten sie die Möglichkeit der kostengünstigen Massenproduktion auf flexiblen Substraten, auch mit innovativen Herstellungsverfahren, wie das Tintenstrahldrucken. Allerdings konnten sie bisher zwei fundamentale Voraussetzungen nicht ausreichend erfüllen: die Langzeitstabilität, sowie die Quanteneffizienz. Organische Solarzellen degenerieren meist aufgrund von Oxidation oder

---

[1] charged coupled device: in etwa „ladungsgekoppeltes Bauelement“

[2] liquid crystal display: Flüssigkristall Display

Reduktion, was dann erheblich die Photon-zu-Ladungsträger Konversioneffizienz herabsetzt. Hier gilt es, für die organische Chemie, neue Materialsysteme zu synthetisieren, die robuster gegenüber den weltlichen Witterungen sind.
Die Quanteneffizienz hängt unmittelbar von der Energieumsetzung eines einzelnen Photons in einen Ladungsträger ab und wie effizient dieser entnommen wird. Der bestimmende Faktor sind die Grenzflächenzustände zwischen aktiven Material und Kontakt; die Überschussenergie zwischen dem Leitungsband des aktiven Materials und des Grenzflächenzustandes geht beim Übergang als Wärme verloren. Genauso verhält es sich mit Photonenenergien, die die Bandlücke weit übersteigen, auch diese Energie geht typischerweise als Wärme verloren. Diese beschränkende Energiekonversions-Eigenschaft ist bekannt als Shockley-Queisser Limes und gilt grundsätzlich für alle einfachen Halbleiter-Solarzellen. In organischen Solarzellen kommt es außerdem verstärkt zur Ladungsträgerrekombination. Diese ergibt sich aus der hohen Bindungsenergie der erzeugten Exzitonen und dem damit zusammenhängenden großen räumlichen Überlapp. Das führt zu geringen Diffusionslängen im Material, so dass ein großteil der Exzitonen nicht zum Photostrom beitragen.
Ein Weg, die Überschussenergie zu nutzen, ist die gezielte Vervielfachung der Ladungsträger nach optischer Anregung. In organischen Halbleitern bietet die Singlet-Exziton-Spaltung eine solche Möglichkeit. Hierbei wird ein Singlet-Exziton in zwei Triplet-Exzitonen aufgespalten. Dieser Prozess erfolgt exotherm, sobald die Singlet-Exzitonen Energie mehr als das Zweifache der Triplet-Exzitonen Energie übersteigt. Ist diese Bedingung erfüllt, erfolgt die Aufspaltung in wenigen hundert Femtosekunden nach der optischen Anregung.
In dem Kapitel 5 wird anhand des Modelsystems von Perfluoropentacen (PFP) Einkristallen, die Singlet-Exziton-Aufspaltung, zum ersten Mal, entlang aller Kristallachsen mit Hilfe der Anrege-Abfrage-Spektroskopie vermessen. Dies wird ermöglicht durch das besondere Kristallwachstum von PFP, welches auf Naf(100) eine stehende Geometrie einnimmt und auf KCl(100) eine Liegende. Dadurch sind alle Achsen in normaler Transmissions-Geometrie adressierbar. Die Messungen ergeben, dass die intermolekulare Kopplung primär entlang der versetzten π-Stapelung, bzw. entlang der $\vec{b}$-Achse erfolgt. Diese Beobachtung entspricht der Vorhersage der Theorie, welche in

diesem Aspekt bestätigt wird. Zusätzlich wird der kohärente Zustand zwischen Singlet-Exziton und Triplet-Exzitonen, das sogenannte Triplet-Paar (^{1}TT), als direkt nach der Anregung induzierte Fano-Resonanz entlang der $\vec{a}$-Achse beobachtet. Die asymmetrische Resonanz resultiert aus der Interferenz der Übergangsamplituden von $T_1 \rightarrow T_4$, der neun einzelnen, nicht-entarteten Sublevels des Triplet-Paars. Nach 15 ps ist die kohärente Überlagerung der beiden Triplet-Exzitonen aufgehoben und der $T_1 \rightarrow T_4$ Übergang ist als symmetrische Resonanz zu sehen. Während der Aufspaltung, relaxiert das Triplet-Paar in einen Excimer-artigen Zustand, dessen Übergänge sich in Form von einer breitbandig induzierten Absorption entlang der $\vec{b}$-Achse manifestieren. Ein Großteil der Triplet-Paare relaxiert strahlend zurück in den Grundzustand, sichtbar als Photolumineszenz 300 meV unterhalb der untersten Exziton-Resonanz. Die Rekombination der Triplet-Exzitonen, welche nach Dephasierung des Triplet-Paares als individuelle Exzitonen agieren, erfolgt auf Nanosekunden-Skala aufgrund des nötigen Spin-Umklapp-Prozesses.

In Kapitel 4 zeigen polarisationsabhängige Absorptionsmessungen der PFP Einkristalle eine schwache Davydov-Aufspaltung von 25 meV. Die Davydov-Aufspaltung ist, in erster Näherung, ein Resultat der Dipolkopplung zwischen den nicht-Translations-invarienten Basis-Molekülen. Da diese im PFP Kristall fast einen rechten Winkel aufspannen, ist die Kopplung klein. Jedoch existiert, wie schon erwähnt, eine starke Kopplung entlang der $\vec{b}$-Achse, welche als H- und J-Aggregate-artige Absorption bei höheren Energien beobachtet wird. Interessanterweise kann durch angeregte Ladungsträger diese Kopplung gehemmt werden, was sich in den Anrege-Abfrage Messungen zeigt.

Im letzten Ergebnis-Kapitel, Kapitel 6, wird mit Hilfe von kohärenten Oszillationen die Dephasierungszeit von exzitonischen Resonanzen in Ge/SiGe Quantenfilmen ermittelt. Kohärente Oszillationen treten bei Anrege-Abfrage-Messungen kurz vor dem Zeitüberlapp von Anrege- und Abfrage-Impuls auf. Aus der Transiente dieses kohärenten Effekts, lässt sich die Dephasierung der entsprechenden Resonanz extrahieren. Dementsprechend, kann bei der Ladungsträger-Analyse, im Anrege-Abfrage-Experiment, die Dephasierungszeit der adressierten Übergänge mitgemessen werden. Die Methode wird auf eine Reihe von Ge/SiGe Quantenfilm Proben angewandt, welche nominell die selben Wachstumsparameter besitzen. Es zeigt sich, dass der Dephasierungsprozess durch

den intrinsischen Streukanal von Γ- zu L-Tal dominiert ist und somit lediglich eine maximale Dephasierungszeit von 300 fs erreicht werden kann. Die beste Probe zeigt eine Dephasierungszeit von 250 fs und somit eine homogene Verbreiterung über den gesamten, untersuchten Temperaturbereich.

1 Introduction

The realization of the first bipolar junction transistor in the year 1948 by Bardeen, Brattain and Shockley [1] sparked off the semiconductor industry, which gradually revolutionized the way we live. Nowadays, semiconductors are the fundamental building blocks of every high-tech electronic device, most notably the computer which has become an inescapable part of our daily lives. Besides voltage and current control capabilities, semiconductors exhibit intriguing opto-electronic properties; the best known and commercially most successful applications are light emitting diodes (LEDs), laser diodes, charged coupled devices (CCD) and solar cells.[2, 3, 4] Due to the broad variety of material systems, they cover virtually the complete optical spectrum while simultaneously being cost-efficient and easy to miniaturize.

Until the late 90ies, commercially available devices were exclusively based on inorganic semiconductors, primarily on Silicon. However, over the last decade, the class of organic semiconductors has gained an increasing amount of interest, e.g., now one of the most popular smartphone's display[1] is based on OLED[2]-technology. Flexibility upon stress and deeper color contrasts are typically named as their main advantages over conventional liquid crystal displays (LCD).

While organic semiconductor devices are already well established as light emitters, they are still in research state as light harvesters. In general, organic solar cells offer high photon cross sections in combination with similar flexibility as OLED displays. Additionally, they exhibit the potential for low-cost mass-production, including innovative and versatile procedures such as ink-jet printing.[6, 7] However, two major challenges still exist which need to be addressed before organic solar cells become compatible:

---

[1] Galaxy S5: 5.1 in (130 mm) 1920x1080 px (432 ppi) Full HD Super AMOLED.[5]

[2] organic light emitting diode

the long-term stability and the quantum efficiency.[8] The fast degradation of organic solar cells is caused by oxidation, reduction and thermal instabilities. Research in this field focuses on the synthesis of new organic molecules, thus, it can be assigned to the organic chemistry sector. Quantum efficiencies are determined by the microscopic photon to carrier conversion, i.e., the photovoltaic effect, therefore, it is predominantly a research topic of solid state physics.

This thesis focuses mainly on aspects of the quantum efficiency in the polyacene Perfluoropentacene (PFP) and its underlying decay processes, namely the electronic relaxation dynamics after optical excitation. In particular, the process of singlet exciton fission is analyzed which promises to double the quantum efficiencies, as it converts one singlet exciton into two triplet excitons.[9] Excitons are correlated electron and hole pairs: neutral excitations of the crystal after absorption of a photon. Singlet exciton fission was first proposed in 1968 in order to explain the drastic photoluminescence quench of Tetracene crystals compared to Anthracene crystals.[10] It has gained renewed attention lately, due to its potential application in the growing field of organic solar cells. However, the microscopic understanding is still in its infancy which hampers essential progress in this field; for instance, the influence of the geometrical order of the molecules within the crystal on singlet exciton fission has only been analyzed theoretically. The reason is the lack of single crystal samples allowing for the correlation of molecular packing and electronic dynamics.[9] This issue is resolved in Chapter 5 for the model system of PFP single crystals, where for the first time the singlet exciton fission dynamics are observed along the three crystal axes by polarization-resolved pump-probe spectroscopy. Moreover, the efficient coupling direction is identified as well as the preceding electronic species of the two triplet excitons.

Although spectroscopic analysis on polyacenes date back to the 40ies [11], lack of computational power and interest lead to the sad state that even interpretations of the linear absorption are still debated today. However, basic knowledge of the linear absorption is essential in order to interpret the non-linear dynamics. Therefore, Chapter 4 serves as a precursor, where the linear absorption of the PFP samples is interpreted using phenomenological models. Here, first indications are given for a dominant coupling direction within the PFP crystal which are then confirmed in Chapter 5.

Furthermore, the amount of exciton splitting in PFP is determined, also known as the Davydov-splitting.[12] It is induced by dipole coupling between the two basis molecules of the crystal lattice during excitation.

In Chapter 6 the focus is shifted to inorganic semiconductors. The chapter introduces a fast and convenient method to determine dephasing times of induced coherent exciton polarizations with more precision than a common lineshape analysis of the absorption spectrum. In pump-probe spectroscopy, the transients of the coherent oscillations are exploited to serve as phase indicators for the several excitonic transitions. These transients are observed during the coherent regime before pump and probe pulses perfectly overlap in time.[13] As a proof of principle, the methodology is applied to a set of Germanium quantum well samples and evaluated in respect to their optical quality. In addition, the main dephasing mechanism in Germanium quantum wells is identified.

These three chapters capture the results of the thesis and are preceded by introductory chapters covering basic light-matter interactions and experimental details; they are succeeded by a conclusion chapter summarizing the essential findings.

2 Basics of Light Matter Coupling in Semiconductors

A basic introduction to fundamentals of light matter coupling in molecules and in-/organic semiconductors is given. The Frank-Condon principle in single molecules is reviewed as well as the singlet and triplet spin systems typically relevant in optical processes with weak spin-orbit coupling. The second part focuses on optical excitations within crystals, with emphasis put on the quasi-particle description of Coulomb bound electron hole pairs, so called excitons. Their distinction into three different classes, namely Frenkel-, Charge-Transfer and Wannier-excitons, is introduced. For a detailed description the reader is referred to one of the many textbooks covering these topics.[14, 15, 13, 16, 17]

2.1 Introduction

Starting from classic macroscopic electrodynamics, where a sinusoidal electromagnetic wave $\vec{E}(\vec{r},t)$ is irradiated on a medium, a polarization $\vec{P}(\vec{r'},t')$ is induced according to the susceptibility $\chi_{ij}(\vec{r},\omega)$ tensor inherent in the medium:

$$P_i(\vec{k},\omega) = \chi_{ij}(\vec{k},\omega)E_j(\vec{k},\omega), \tag{2.1}$$

where the Fourier transforms are given, after applying the convolution theorem.[14] Typically, for comparison with experiments the dieelectric tensor is used defined as the material parameter of the electric displacement induced by the electric field and the polarization and related to the susceptibility as follows:

$$\epsilon(\vec{k},\omega) = 1 + 4\pi\chi_{ij}(\vec{k},\omega). \tag{2.2}$$

Assuming an isotropic medium, where relevant dimensions for excitation such as lattice spacings are significantly smaller than the excitation wavelength, i.e., the photon wavevector can be approximated to be zero, the dieelectric tensor simplifies to the scalar dieelectric function $\epsilon(\omega)$. It is related to the complex refractive index $\tilde{n}$ by:

$$\epsilon(\omega) = \tilde{n}^2. \tag{2.3}$$

Since they are the Fourier components of the real space quantities, they can be complex quantities. Generally, the complex component of $\tilde{n}$ is referred to as the extinction coefficient κ capturing the amount of light damped in the material. It is proportional to the absorption coefficient α of Beer's Law:

$$\alpha = \frac{4\pi}{\lambda_0}\kappa, \tag{2.4}$$

where λ_0 is the vacuum wavelength. This quantity and its change under excitation is predominantly determined throughout this thesis.

On a microscopic scale, a system's energy is quantized due to its wave nature, i.e., below an excitation continuum the system exhibits discrete eigenstates corresponding to standing waves confined within the related potential. Depending on the coupling mechanism, transitions between these states can be induced when distinct criteria are matched, most notably the energy difference between these states. This intrinsic feature of nature is the origin, for instance, of the discrete spectral lines observed in Neon light tubes. Since this thesis covers optical spectroscopy of semiconductors, transitions between the system's states occur in first approximation exclusively through dipole coupling.

Considering a dipole allowed transition from the groundstate $|0\rangle$ of a system to the i$_{th}$

excited state $|i\rangle$ of the system with dipoles polarized along the x-axis the first order susceptibility can be given by:[15]

$$\chi^{(1)}(\omega) = \frac{N}{\epsilon_0 \hbar} \sum_i \left[\frac{\langle 0 \,|\hat{\mu}_x|\, i\rangle \langle i \,|\hat{\mu}_x|\, 0\rangle}{\Omega_i - \omega} + \frac{\langle 0 \,|\hat{\mu}_x|\, i\rangle \langle i \,|\hat{\mu}_x|\, 0\rangle}{\Omega_i + \omega} \right], \tag{2.5}$$

where $\Omega_i = (E_i - E_0)/\hbar$ is the angular transition frequency of the state $|i\rangle$ and $\hat{\mu}_x$ is the dipole moment along the x-axis. With the introduction of the oscillator strength:

$$f_i = \frac{2m}{e^2 \hbar} \Omega_i \left| \langle 0 \,|\hat{\mu}_x|\, i\rangle \right|^2, \tag{2.6}$$

Eq. 2.5 is simplified to:

$$\chi^{(1)}(\omega) = \frac{Ne^2}{m\epsilon_0} \sum_i \frac{f_i}{\Omega_i^2 - \omega^2}. \tag{2.7}$$

The oscillator strength has to fulfill the important sum rule:

$$\sum_i f_i = N_e, \tag{2.8}$$

where N_e is the number of valence electrons. Realistically, the induced polarization by the electric field is a damped oscillation, hence, a damping factor γ is introduced in Eq. 2.7 and with the relation of Eq. 2.2 the following form is reached:

$$\epsilon(\omega) = 1 + \frac{Ne^2}{m\epsilon_0} \sum_j \frac{f_j}{\Omega_j^2 - \omega^2 - i\omega\gamma_j}. \tag{2.9}$$

Following Eq. 2.4, where the imaginary part of Eq. 2.9 yields the absorption, and assuming a single resonance, we get:

$$\kappa(\omega) = \frac{\omega\gamma f}{(\Omega_i^2 - \omega^2)^2 + \omega^2\gamma^2}. \tag{2.10}$$

This is the typical Lorentzian line-shape often observed in absorption spectra where inhomogeneous broadening is negligible. The homogeneous broadening of the resonance is determined by the damping factor γ, which is physically the decay of the induced

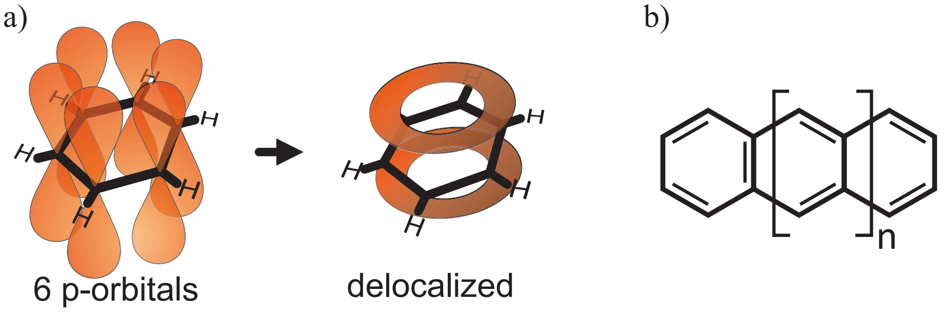

Abbildung 2.1: (a) Delocalized π-system formed by the six p_z-orbitals of the carbon atoms oriented perpendicular to the molecular plane in benzene. From Ref. [18]. (b) Molecules of the acene-class.

polarization, i.e., the reciprocal of the dephasing time ($\gamma = 1/T_2$).

2.2 Optical Properties of Single Molecules

The building block of the acenes, such as pentacene and perfluoropentacene, are benzene molecules which are linearly „fused“ (Fig. 2.1 (b)). Benzene exhibits an sp^2-hybridization where the six carbon atoms form a planar ring with six σ-bonds in an angle of 120°. The remaining six p_z-orbitals are oriented perpendicular to the plane and do not participate in the σ-bonds (see Fig. 2.1 (a)). These dangling orbitals overlap and form a π-system, where the electrons delocalize over the entire ring (see Fig. 2.1 (a)). Hence, these type of molecules are also called unsaturated or conjugated.[15] In first approximation, σ- and π-electrons are decoupled where the σ-electrons are considered as core electrons predominantly responsible for the bonding. Due to the weaker bonding character of the π-orbitals, they constitute the HOMO and LUMO orbitals. Transitions between bonding and antibonding π-orbitals lie within a few eV (1-3 eV) whereas transitions between σ-orbitals often exceed 10 eV. Consequently, optical properties of acenes are well described by π-electron models where the σ-electrons and core electrons are treated as a background screening potential. There are many different models with different approximations trying to describe quantitatively the physical properties of π-systems; the most famous are given below:[15]

- Hückel-model:
  Noninteracting electrons with a fixed geometry

- Su-Schrieffer-Heeger-model (SSH):
  Noninteracting electrons with dynamic nuclei

- Peierls-model:
  Static-nuclear limit of the SSH-model

- Pariser-Par-Pope-model (P-P-P):
  Interacting electrons with a fixed geometry

and their combinations. After having determined the several π-orbitals the optical properties can be calculated by evaluating the transition dipole moment $\langle I \left|\hat{\mu}\right| J\rangle$. Probably, its most prominent treatment is covered in the next section.

2.2.1 Franck Condon Principle

Essentially, optical transitions between molecular orbitals are described by the transition dipole moments $\langle I \left|\hat{\mu}\right| J\rangle$. As the states $|I\rangle$ and $|J\rangle$ have many degrees of freedom including positions of electrons and nuclei, calculations would be typically too complex to be performed. Therefore, besides considering only the π-system electrons, further approximations have to be applied. One of the earliest, most drastic and probably best known approximation is the Franck-Condon principle. It adapts the Born-Oppenheimer approximation, where the electronic motion is considered to be too fast for the nuclei to follow. In Fig. 2.2 (a) the simplified adiabatic energy potentials for two electronic states of a molecule are sketched as a function of the general coordinate R[1]. Typically, the minimum of the higher electronic states are at a different R than in the groundstate potential, due to the changed electronic distribution. The offset between the minima

---

[1] In the simplest case known as the diatomic model, R describes the inter-molecular distance.

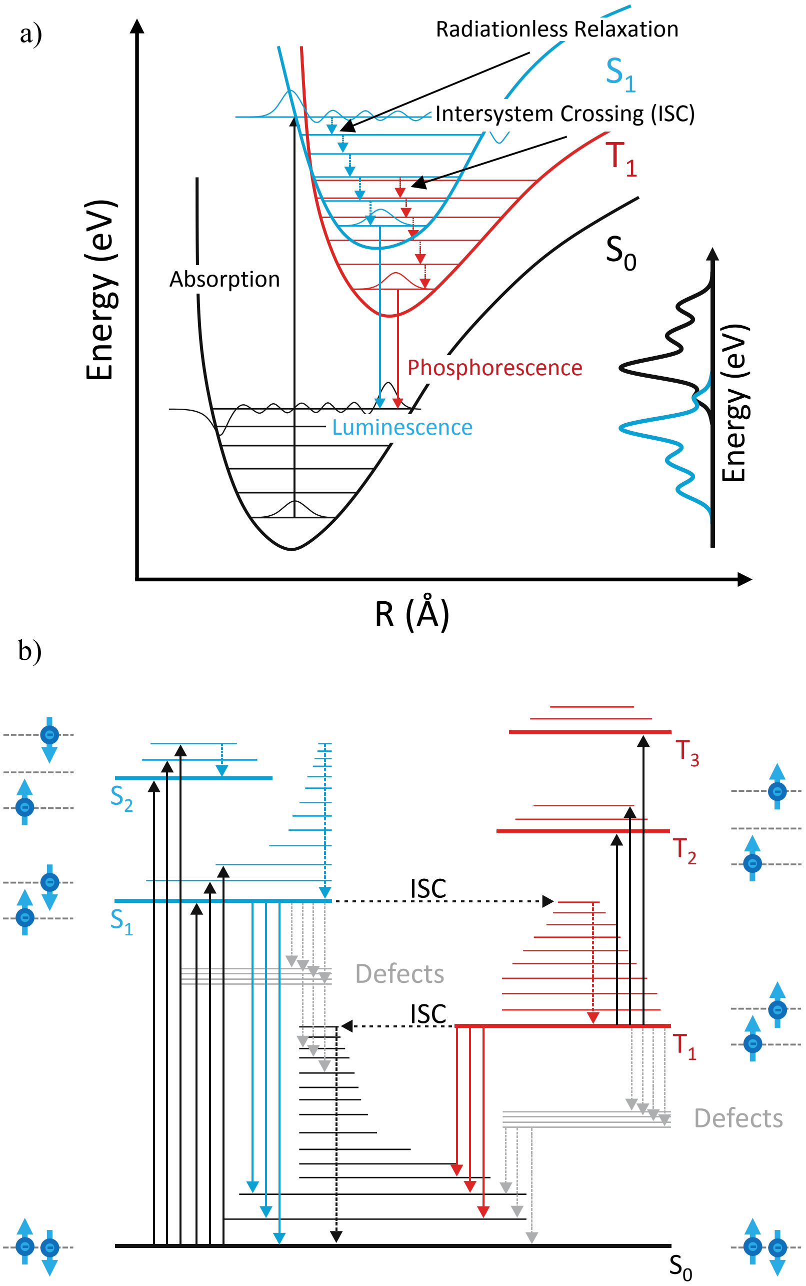

Abbildung 2.2: (a) Franck-Condon energy level scheme with possible relaxation channels in a single molecule. (b) Single particle energy levels in an organic crystal with possible relaxation channels after optical excitation.

is characterized by the Huang-Rhys parameter which is given by:

$$S = \frac{M\omega}{2\hbar}(R_i - Rj)^2, \tag{2.11}$$

where $R_{i,j}$ denote the minima of the potentials, M the molecular mass and ω the radial eigenfrequency of the vibron. Following the approximation of vanishing nuclear motion during optical transitions, excitations occur vertical within this scheme, i.e., R is not changed. As always, the effective overlap between initial and final state governs the transition rate and, accordingly, the oscillator strength. Since both energy potentials differ, an electronic excitation is predominantly accompanied by a vibronic excitation. Consequently, the resonance with the highest oscillator strength is not the $\nu_0 \rightarrow \nu_0^{'}$ transition but, in general, some higher transition $\nu_0 \rightarrow \nu_n^{'}$ (marked with a black vertical arrow in Fig. 2.2 (a)).

In first approximation the electronic states can be assumed as the product of electronic and vibrational wavefunction:[15]

$$|J\rangle = |j;R\rangle\,|\nu_j\rangle\,, \tag{2.12}$$

where $|j;R\rangle$ is the electronic state parametrized by R and $|\nu_j\rangle$ is the vibrational state. Then, the dipole operator for an optical transition can be treated as the sum of electronic and nuclear dipole moments:

$$\hat{\mu} = \hat{\mu}_e + \hat{\mu}_N. \tag{2.13}$$

Eventually, the total transition dipole moment is given by:

$$\begin{aligned} \langle I\,|\hat{\mu}|\,J\rangle &= \langle i;R|\,\hat{\mu}_e\,|j;R\rangle\,\langle\nu_i|\,\nu_j\rangle + \langle i;R|\,j;R\rangle\,\langle\nu_i|\,\hat{\mu}_N\,|\nu_j\rangle\,, && (2.14)\\ &= \langle i;R|\,\hat{\mu}_e\,|j;R\rangle\,\langle\nu_i|\,\nu_j\rangle\,. && (2.15)\end{aligned}$$

As $|i;R\rangle$ and $|j;R\rangle$ are ortho-normal, the second term on the *RHS* of Eq. 2.14 vanishes. Thus, the transition probability is given by the electronic dipole moment scaled by the overlap integral of both nuclear wavefunctions at the same general coordinate R. The measured intensity of a transition is given by the square of the total dipole moment, so that we end up with the scaling factor $F_{ij} = \langle \nu_i | \, \nu_j \rangle^2$ for the oscillator strength, which is also known as the Franck-Condon factor.

After excitation the excited molecule relaxes towards the lowest vibrational level within the excited electronic potential; this internal conversion happens non-radiatively, and in general on a picosecond timescale. When the lowest vibrational level is reached, typically the molecule returns to its electronic groundstate by radiative emission, again, according to the Franck-Condon principle (blue arrow in Fig. 2.2 (a)). Similar to the absorption process, the overlap integral betwen nuclear wavefunctions plays the crucial role of the observed intensity distribution. As a result, a mirror image of the absorption is observed in the photoluminescence spectrum (cf. inset Fig 2.2 (a)).

The spectrum of many conjugated molecules is dominated by a stretching mode positioned at an energy around 175 meV.[19] However, in complex systems such as acenes, a manifold of Raman-active vibrons exist which are superimposed in the absorption spectrum. Consequently, the observed vibronic progression is severely broadened with significant asymmetric lineshapes which hamper a precise determination of the eigenfrequency. In the crystal phase, coupling between the basis molecules introduces sidebands which are observed as Davydov-split resonances in IR-spectroscopy.[20] Additionally, low energy crystal lattice excitations (≈ 9 eV) are present further broadening the spectrum. Anyhow, schematically the Franck-Condon principle is also applied here, shown in Fig. 2.2 (b).

2.2.2 Singlet and Triplet System

In acenes the spin-orbit coupling is weak, and considered to be negligible. This is reasonable, since the spin-orbit coupling scales with the cube of the atomic number, which is low in Hydrogen, Carbon and Fluor. Therefore, spin is still a good quantum number in these systems. As mentioned before, optical excitation in acenes occurs in the conjugated π-system, where the HOMO constitutes the initial state and the anti-bonding π-orbitals, mainly the LUMO, constitute the final states. In acenes, the HOMO is saturated, i.e., it is populated with two electrons with opposite spin. The total electronic wavefunction is antisymmetric under the exchange of two electrons, a consequence of their fermionic nature. Since spin-orbit coupling is negligible, the total wavefunction can be written as the product of spatial and spin wavefunction:

$$\Phi(\vec{r},\vec{\sigma}) = \varphi(\vec{r})\chi(\vec{\sigma}). \tag{2.16}$$

Either one of them is antisymmetric while the other is symmetric in order to get an overall antisymmetric wavefunction. Hence, the groundstate is a singlet state where the spin function is antisymmetric and the electrons populate the same orbital:

$$^{1}\Phi(\vec{r},\vec{\sigma}) = \varphi_1(1)\varphi_1(2)\left\{\chi_\uparrow(1)\chi_\downarrow(2) - \chi_\downarrow(1)\chi_\uparrow(2)\right\}, \tag{2.17}$$

where $\varphi_i(j)$ denotes the orbital and $\chi_{\downarrow\uparrow}(j)$ the spin state of electron j. The next higher states are the triplet states where the spin function is symmetric and the spatial wavefunction is antisymmetric. As a consequence, three spin settings with nearly degenerate eigenenergies are possible where both electrons cannot populate the same orbital anymore:

$$^{3}\Phi(\vec{r},\vec{\sigma}) = \left\{\varphi_1(1)\varphi_2(2) - \varphi_1(2)\varphi_2(1)\right\}\chi_\uparrow(1)\chi_\uparrow(2), \tag{2.18}$$

$$^{3}\Phi(\vec{r},\vec{\sigma}) = \left\{\varphi_1(1)\varphi_2(2) - \varphi_1(2)\varphi_2(1)\right\}\chi_\downarrow(1)\chi_\downarrow(2), \tag{2.19}$$

$$^{3}\Phi(\vec{r},\vec{\sigma}) = \left\{\varphi_1(1)\varphi_2(2) - \varphi_1(2)\varphi_2(1)\right\}\left\{\chi_\uparrow(1)\chi_\downarrow(2) + \chi_\downarrow(1)\chi_\uparrow(2)\right\}. \tag{2.20}$$

Due to spin conservation during dipole transitions, optical excitations are restricted to one spin system. However, the strict rule in an ideal system is weakened in the real system, so that transitions from the singlet groundstate into an excited triplet state is possible, however, with virtually vanishing probability. The same holds true for the system relaxation after optical excitation. Accordingly, in Fig. 2.2 (a) we also see the intersystem crossing (ISC) as a relaxation channel, i.e., non-radiative relaxation into the triplet system, e.g., $S_1 \rightarrow T_1$, with consecutive phosphorescence into the groundstate. The term phosphorescence is used to highlight the average lifetime of the excited triplet state, which occasionally lasts for many hours and is then considered as metastable. In Ch. 5 an unusual relaxation process in Perfluoropentacene crystals is analyzed, where the excited singlet excitons relax into the triplet state on an ultrafast timescale (below 100 fs) by exciting another triplet exciton on an adjacent lattice site. This so called singlet exciton fission process promises to double the light to carrier conversion efficiency.

2.3 Optical Properties of Single Crystals

Changing from the single molecule to the crystal, the picture of a single excitation is replaced by a collective excitation of the crystal. Consequently, the eigenstates of the molecule are no longer valid; they are replaced by eigenstates , which comply the symmetries of the crystal. This also implies the formation of bands due to the interaction of the discrete atomic or molecular levels. Optical transitions in crystals are then treated as electron-hole excitations, where dealing with the complete set of valence electrons is avoided by describing the electron vacancy effectively as a positive hole in the valence band. Due to their Coulomb attraction they form electron-hole pairs, so called excitons which are subdivided into the three classes (see Fig. 2.3): Frenkel, Charge-Transfer and Wannier. Roughly speaking, they are classified according to their electron-hole correlation length, i.e., their binding energy. The Frenkel exciton exhibits the highest binding energy with around 1 eV and is the extreme case of a completely localized excitation on one lattice site. The other extreme is the Wannier exciton which exhibits an exciton Bohr radius of 10 nm with a binding energy of around 4.5 meV in the prototypical model system GaAs and is considered as completely delocalized upon several hundred lattice sites. The charge-transfer exciton is considered as the transition between both extremes. The spatial extension of electron and hole is not confined on one lattice site but distributed over nearest neighbors. In the following a short introduction to the three exciton types is given.

2.3.1 Frenkel Excitons

The Frenkel exciton is the limit of neutral excitation completely localized on one lattice site which is sometimes considered to be the lowest optical transition in organic acene

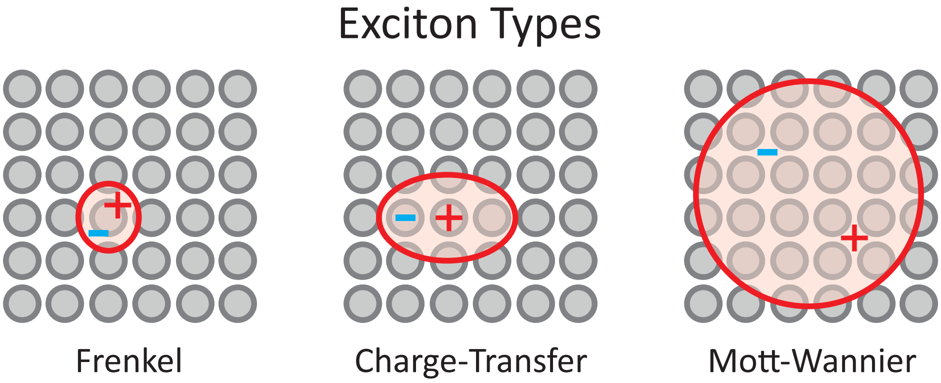

Abbildung 2.3: The three prevailing types of excitons commonly found in semiconductors: Frenkel- and Charge-Transfer excitons in organic semiconductors; Wannier excitons in inorganic semiconductors.

crystals. In these crystals bonding is mediated by weak van der Waals interaction alone, which leads to low dispersion and consequently high probability of localization. Correspondingly, the excited electron-hole pair does experience very weak screening effects by other excited carriers which explains their strong Coulomb correlation, i.e., their typically large binding energies. One of the first treatments of the optical excitation has been done by A. S. Davydov, whose work gave a qualitative understanding of the split exciton resonance in organic crystals with two basis molecules.[12]
Starting with the simple case of one basis molecule in the unit cell of the crystal with no intermolecular interaction the groundstate is the direct product of the molecular groundstate $|GS\rangle_i$ at crystal site i:

$$|GS\rangle = \prod_{i=1}^{N} |GS\rangle_i \,. \tag{2.21}$$

Now an electron-hole pair excitation is considered at lattice site m ($|EX\rangle_m$):

$$|EX\rangle = |EX\rangle_m \prod_{i=1}^{N-1} |GS\rangle_i \,. \tag{2.22}$$

However the exciting photon is delocalized according to its wavelength, hence, the excitation is also delocalized, i.e., it is a crystalline excitation with periodic boundary conditions. The generally applied solution is the Bloch-wave ansatz, which yields:

$$\psi_k(\vec{r}) = \frac{1}{\sqrt{N}} \sum_{n=1}^{N} \Phi_n(\vec{r}) \exp\left(-ikna\right), \tag{2.23}$$

with the local exciton function $\Phi_n(\vec{r}) \equiv \langle \vec{r} | \, EX \rangle$, the wavevector k and the lattice parameter a. Consequently, in the case of zero coupling every state which differs in k would be degenerate.

Although, the coupling within organic crystals is weak, it is not negligible and leads to the observation of exciton band dispersion and splitting which is known as the Davydov-splitting.

Davydov-Splitting

The Davydov splitting describes the excitonic band splitting due to the transition dipole coupling of adjacent molecules. Coupling is induced by the Coulomb interaction and is treated by the Coulomb correlation term H_{mn}^{e-e} in the system hamiltonian. Considering resonant exciton transfer between molecules, which is the case in optical transitions[2], the system is transfered from the initial $|I\rangle$ to the final state $|F\rangle$ described by the transfer integral W_{mn}:

$$W_{mn} = \langle F | \, H_{mn}^{e-e} \, | I \rangle \tag{2.24}$$

$$\text{with } \; |I\rangle = |EX\rangle_m \, |GS\rangle_n \prod_{i}^{N-2} |GS\rangle_i \tag{2.25}$$

$$\text{and } \; |F\rangle = |GS\rangle_m \, |EX\rangle_n \prod_{i}^{N-2} |GS\rangle_i \, . \tag{2.26}$$

Now, only dimer coupling is treated, where exchange exciton transfer is ignored ($W_{mn} \rightarrow J_{mn}$), i.e., triplet exciton transfer. Thus, in second quantization the transfer integral

---

[2] The exciton transfer time is shorter than the phonon and/or vibron scattering time.

yields:

$$J_{mn} = \sum_{i\in m, j\in n} V_{ij} \left[_m \langle GS| \, (\hat{N}_i - 1) \, |EX\rangle_m\right] \left[_n \langle EX| \, (\hat{N}_j - 1) \, |GS\rangle_n\right], \tag{2.27}$$

where $\hat{N}_{i,j}$ are the particle number operator and

$$V_{ij} = \frac{e^2}{|\vec{r}_i - \vec{r}_j|}$$

the matrix elements of the Coulomb potential. In order to evaluate the transfer integrals the dipole approximation is applied:

$$\sum_{i\in m, j\in n} \frac{1}{|\vec{r}_i - \vec{r}_j|} \approx \frac{\sum \tilde{\vec{r}}_i \cdot \sum \tilde{\vec{r}}_j}{|\vec{R}_{mn}|^3} - \frac{3\left(\sum \vec{R}_{mn} \cdot \tilde{\vec{r}}_i\right)\left(\sum \vec{R}_{mn} \cdot \tilde{\vec{r}}_j\right)}{|\vec{R}_{mn}|^5} \tag{2.28}$$

where $\vec{R}_m$ and $\vec{R}_n$ are the center of mass coordinates of molecule m and n and $\tilde{\vec{r}}_{i(j)}$[3] are the site coordinates relative to the centre-of-mass. Now Eg. 2.27 can be separated in a directional term (κ_{mn}) and a term J^0_{mn} describing the interaction of the dipole matrix elements:

$$J_{mn} = \underbrace{\left(\vec{e}_{r_m} \cdot \vec{e}_{r_n} - 3\left(\vec{e}_{R_{mn}} \cdot \vec{e}_{r_m}\right)\left(\vec{e}_{R_{mn}} \cdot \vec{e}_{r_n}\right)\right)}_{\kappa_{mn}} \times \underbrace{\frac{[_m \langle GS| \, \hat{\mu}_m \, |EX\rangle_m] \, [_n \langle EX| \, \hat{\mu}_n \, |GS\rangle_n]}{|\vec{R}_{mn}|^3}}_{J^0_{mn}} \tag{2.29}$$

with the unit vectors $\vec{e}_{r_{n(m)}}$ and $\vec{e}_{R_{mn}}$ and the dipole operators $\hat{\mu}_{m(n)}$[4]. Accordingly, Eq. 2.29 describes the coherent transfer of dipole allowed excitons within this approximation. Due to the coupling new eigenstates occur:

$$|\pm\rangle = |EX\rangle_m \, |GS\rangle_n \pm |GS\rangle_m \, |EX\rangle_n \tag{2.30}$$

---

[3] $\tilde{\vec{r}}_{i(j)} = \vec{r}_{i(j)} - \vec{R}_{m(n)}$

[4] $\hat{\mu}_m = e \sum \tilde{\vec{r}}_i \left(\hat{N}_i - 1\right)$

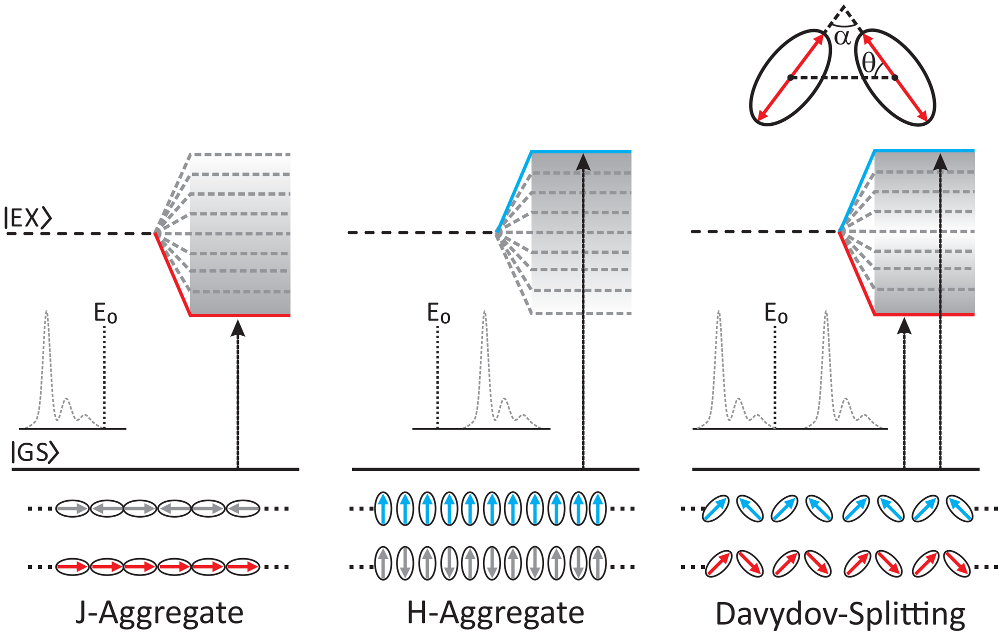

Abbildung 2.4: The three prevailing cases of dipole coupling within an organic crystal.

with the eigenenergies $E_{DS} = E_0 \pm J_{mn}$ and hence, an energy spltting (Davydov splitting) of $\Delta E = 2J_{mn}$.

A typical evaluation of the Davydov splitting is performed by another simplification; only the coupling of two dipoles is considered geometrically oriented within a plane, as it is shown in the top right corner of Fig. 2.4. Then the geometrical term κ_{mn} can be parametrized by the angles α and θ and the Davydov splitting is given by:

$$\Delta E = \frac{2 \cdot |\langle GS| \, \hat{\mu} \, |\pm\rangle|^2}{|\vec{R}_{mn}|^3} (\cos\alpha - 3\cos^2\theta), \tag{2.31}$$

where additionally the dipole moments of both basis molecules are considered to be equal. Accordingly, in polarization dependent linear absorption measurements, a $\cos^2\theta$ dependence is observed. A distinction is drawn between the three cases shown in Fig. 2.4. The first two are the extreme cases of the Davydov-splitting, also known as J- and H-aggregate. Within both aggregates, in linear absorption no exciton band splitting is observed, since anti-phase dipole coupling leads to destructive interference

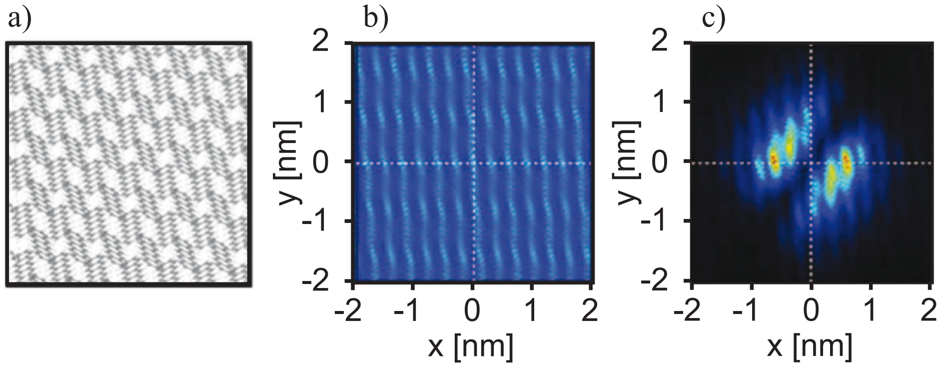

Abbildung 2.5: (a) Crystal structure of Pentacene within the *ab*-plane. (b) Two-dimensional electron-hole correlation function for the non-interacting electron-hole wavefunction. (c) Electron-hole correlation function for the singlet exciton. In both cases the position of the hole is fixed to the center. Adapted from Ref. [21].

and dark states. Concerning the J-aggregate, the evaluation of Eqs. 2.29 and 2.31 leads to a negative value ($-2J^0_{mn}$), hence, a reduction of the transition energy. The reverse situation is found in the H-aggregate, here, a the evaluation yields a positive value (J^0_{mn}) and consequently a shift of the transition to higher energies.

2.3.2 Charge-Transfer Excitons

The Davydov description of excitons in organic crystals gives only qualitative results concerning the exciton band splitting.[19] In addition, without the knowledge of the ground and excited wavefunctions no calculation can be performed. Thus, the major challenge lies within their determination.

In the following, a rough description of an *ab initio* method is given which has proven to be a versatile and powerful tool to calculate absorption spectra correctly for a wide range of material systems, e.g., pentacene single crystals or carbon nanotubes.[22, 23] In pentacene crystals for instance, it revealed the strong charge transfer character of even the lowest excitonic resonances, shown in Fig. 2.5.[21] The short description is taken from Ref. [22] and can be read in full detail in Ref. [24].

The theoretical treatment is sepparated into three steps:

1. The groundstate of the interacting many-electron system is determined by density functional theory (DFT) by solving a set of effective, self-consistent, single-body equations.[25, 22]

2. The excited single particle states are corrected by the GW-approximation of the non-local self-energy.[26] The adjusted states are valid for single particle excitation, e.g., the addition or removal of an electron.

3. The GW corrected states are used to calculate bound two-particle states with the Bethe-Salpeter Equation (BSE).[24] They yield the excitonic states observed in the absorption spectra.

Accordingly, the solution of the Kohn-Sham equations lay the foundation for the theoretical description of the system under consideration:

$$\left[-\frac{\hbar^2\nabla^2}{2m}+V_{ion}(\vec{r})+V_H(\vec{r})+V_{xc}(\vec{r})\right]\phi_j(\vec{r})=\epsilon_j\phi_j(\vec{r}), \tag{2.32}$$

where $\phi_j(\vec{r})$ are the Kohn-Sham orbitals, V_{ion} is the Coulomb interaction between electrons and atomic nuclei, V_H is the Coulomb repulsion between an electron and the field generated by the average electronic distributionon, i.e., the Hartree level, and V_{xc} is an exchange-correlation potential that encodes the complex, quantum electron-electron interactions. In order to solve the equations, typically a few approximations need to be performed, which are reviewed in Ref. [27]. Especially V_{xc} is tricky to handle, and a standard approach is the local density approximation (LDA) where long-range and energy dependent interactions are ignored. It yields accurate results for the groundstate, however, grossly wrong results for excited states. This issue is tackled by many-body perturbation theory, where firstly the one-particle Green's function provide the correct quasi-particle properties of excited electrons or holes within the system and secondly the two-particle Green's function handles the Coulomb interaction between electron and hole which are both created at an absorption incident. The quasiparticle

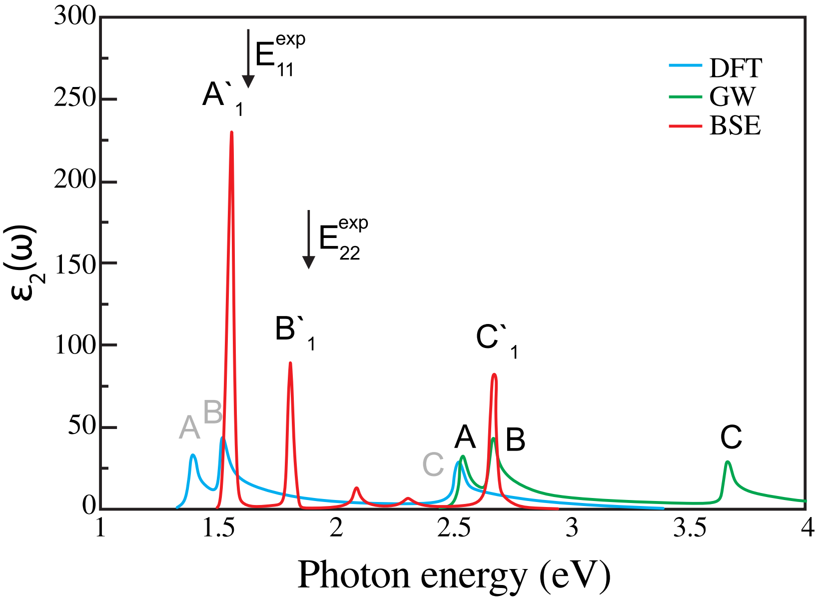

Abbildung 2.6: Calculated absorption spectra for carbon nanotubes with increasing Coulomb correlation accuracy. Adapted from Ref. [22].

energies and amplitudes are determined by the self-consistent Dyson equation:

$$\left[-\frac{\hbar^2\nabla^2}{2m} + V_{ion}(\vec{r}) + V_H(\vec{r})\right]\psi_j(\vec{r}) + \int d\vec{r\prime}\sum\nolimits_{xc}(\vec{r},\vec{r\prime},\epsilon_j)\,\psi_j(\vec{r\prime}) = \epsilon_j\psi_j(\vec{r}). \tag{2.33}$$

Here, the local, energy-independent exchange-correlation potential $V_{xc}(\vec{r})$ of Eq. 2.32 is substitued by $\sum_{xc}(\vec{r},\vec{r\prime},\epsilon_j)$ which encodes the non-local, energy-dependent exchange-correlation potential for an excited quasiparticle induced by the surrounding electronic medium. However, in practice, the exact $\sum_{xc}(\vec{r},\vec{r\prime},\epsilon_j)$ potential is approximated by the GW-method.[26] It approximates the exchange-correlation function as the convolution of the screened Coloumb interaction $W(\vec{r},\vec{r\prime};\epsilon_j)$ and the one-particle Green function $G(\vec{r},\vec{r\prime};\epsilon_j)$:[23]

$$\sum\nolimits_{xc} = iG_1W. \tag{2.34}$$

Typically, a band energy accuracy of $\approx 0.1-0.2\,\text{eV}$ is achieved. In case of high exciton binding energies the GW-bandgap deviates significantly from the optical gap, e.g., in carbon nanotubes or organic crystals. As excitons are two-particle quantities they can be described by a two-particle Green's function approach. The corresponding equation of motion is the Bethe-Salpeter equation, describing bound states of the two-particle Dyson equation:

$$\left(\epsilon_c - \epsilon_v\right) A^S_{cv} + \sum_{c'v'} K\left(\Omega_S\right)_{cv,c'v'} A^S_{c'v'} = \omega_S A^S_{cv}, \tag{2.35}$$

where $\epsilon_{c;v}$ are the GW-energies for valence and conduction band, A^S_{cv} are the electron-hole correlation coefficients of the exciton wavefunction, Ω_S are the exciton energies for the various exciton states S and $K\left(\Omega_S\right)_{cv,c'v'}$ is the so called electron-hole interaction kernel which includes an attractive long-range screened Coulomb interaction as well as a short-range repulsive „exchange“ interaction.[22] The exciton wavefunction $\chi_S\left(\vec{r}_e, \vec{r}_h\right)$ is treated within the Tamm-Dancoff approximation:

$$\chi_S\left(\vec{r}_e, \vec{r}_h\right) = \sum_{cv} A^S_{cv} \psi_c\left(\vec{r}_e\right) \psi^*_v\left(\vec{r}_h\right), \tag{2.36}$$

it is the sum over the free GW electron and hole states where A^S_{cv} allow for correlation and entanglement of the electron and hole and the formation of excitons. By solving the BSE the desired quantities Ω_S and A^S_{cv} are determined, so that excitonic spectrum and relative electron-hole positions can be analysed.

The relative electron-hole wavefunction change from single particle GW-states to two-particle states (BSE) is shown in Figs. 2.5 (b) and (c) in the case of pentacene, where the hole is fixed to the center. Apparently, without two-particle correlation the electron wavefunctions are Bloch-waves according to the lattice potential, however, with two-particle correlation excitons are formed with an increased localization of electron and hole. Nevertheless, a significant amount of the electron wavefunction is extended over neighbouring lattice sites, i.e., they form charge-transfer excitons. Hence, ab initio calculation show that even the excitons with the highest binding energy are no pure Frenkel excitons.[21]

An overview of the transition energies for each calculation step is given in Fig. 2.6 for carbon nanotubes. As expected, DFT calculations severely underestimate the band gap which is corrected by GW. However, strong Coulomb correlation shifts the transitons back to lower energies. In general, the BSE-GW approach achieves an agreement with experiment in the range of 0.1-0.2 eV.

2.3.3 Wannier Excitons

For an inorganic, direct gap semiconductor valence and conduction band are considered to be parabolic at the direct transition, which are typically located at the highest symmetry point of the reciprocal lattice, the Γ-point. Due to the strong delocalized nature of electrons and holes it is valid to apply the effective mass approximation which captures the quasi free carriers within the periodic lattice potential. Again, Coulomb interaction leads to bound excitonic states, however, with between one or two orders of magnitude lower binding energies, e.g., GaAs ≈4.5 meV in comparison to speculated ≈0.5 eV in Pentacene.[28, 29]
We start with the exciton wavefunction which is comparable to Eq. 2.36 considering Bloch waves:

$$\begin{aligned}\chi\left(\vec{r}_e,\vec{r}_h\right) \cong & u_{c_0}u_{v_0}\underbrace{\sum_{\vec{k}_e,\vec{k}_h} A(\vec{k}_e,\vec{k}_h)e^{i\vec{k}_e\cdot\vec{r}_e}e^{i\vec{k}_h\cdot\vec{r}_h}}_{\Phi(\vec{r}_e,\vec{r}_h)} && (2.37)\\ \cong & u_{c_0}u_{v_0}\Phi(\vec{r}_e,\vec{r}_h), && (2.38)\end{aligned}$$

where $\Phi(\vec{r}_e,\vec{r}_h)$ is the exciton envelope function and $u_{c_0}u_{v_0}$ the atomic functions which are considered to vary slowly with $\vec{k}$ and therefore are evaluated at the Γ-point.[28] The exciton envelope function describes the long range relative motion of electron and hole and obeys the two-particle Schrödinger equation with effective masses of electron and hole. Consequently, in the case of one excited exciton, the description is equal to the hydrogen atom. By changing to relative ($\vec{r}$) and center-of-mass ($\vec{R}$) coordinates the exciton envelope function can be separated:

$$\Phi(\vec{R},\vec{r}) = g(\vec{R})\phi(\vec{r}). \tag{2.39}$$

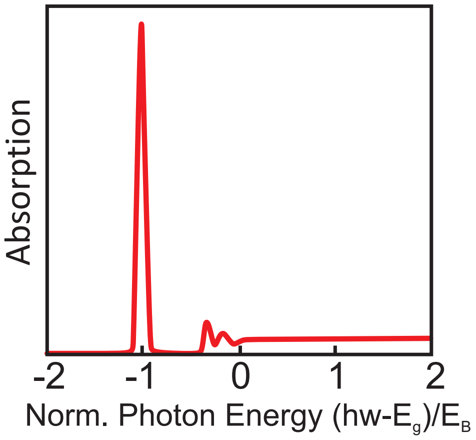

Abbildung 2.7: Calculated absorption spectrum with the Elliott formula for three dimensions. Clearly the transition from discrete to continuum states is observed. Adapted from Ref. [13]

It shows that the center of mass of the electron-hole pair moves like a free particle and the relative mass wavefunction obeys the Schrödinger equation of the relative mass hydrogen atom and is commonly known as the Wannier equation:[28]

$$\left[-\frac{\hbar^2}{2m_r}\nabla_r^2 - \frac{e^2}{\epsilon_0 \vec{r}}\right]\phi(\vec{r}) = E_r\phi(\vec{r}). \tag{2.40}$$

It is solved accordingly with the eigenenergies:

$$E_r \equiv E_{n,l,m} = \frac{m_r e^4}{2\hbar^2\epsilon_0^2}\left(\frac{1}{n^2}\right) = -\frac{\hbar^2}{2m_r a_B^2}\left(\frac{1}{n^2}\right), \tag{2.41}$$

where $a_B = \epsilon_0\hbar^2/m_r e^2$ is the exciton Bohr radius.
The transition probability W is calculated by evaluating the interband matrix elements between all combinations of electron-hole states that make the exciton wave packet according to Fermi's golden rule:

$$W \propto \left|\sum_{\vec{k}_e,\vec{k}_h} A(\vec{k}_e,\vec{k}_h)\int d\vec{r}(u_{c_0}e^{i\vec{k}_e\cdot\vec{r}_e})^*(e\cdot\vec{r})(u_{v_0}e^{i\vec{k}_h\cdot\vec{r}_h})\right|^2. \tag{2.42}$$

The absorption coefficient for excitons is then obtained by evaluating the Elliott formula which is derived from Eq. 2.42:[13]

$$\alpha(\omega) = \frac{8\pi^2\omega|d_{cv}|^2}{n_b c} \sum_n |\phi_n(\vec{r}=0)|^2 \, \delta\left(\hbar\omega - E_g + \frac{E_B}{n^2}\right) \tag{2.43}$$

with the interband dipole matrix element d_{cv}, the background refractive index n_b, the quasi particle bandgap energy E_g and the Coulomb enhancement factor $|\phi_n(\vec{r}=0)|^2$. Since $|\phi_n(\vec{r}=0)|^2$ is only nonzero for s states, these are the only states visible in the optical spectrum. A result of the Elliott formula for three dimensions is shown in Fig. 2.7.[13]

3 Experimental Details

This chapter shortly reviews the applied spectroscopic techniques used throughout this thesis. Furthermore, handling procedures are presented, which are necessary to get correct and low-noise data. The applied methods include linear absorption, CW photoluminescence spectroscopy and pump-probe spectroscopy.

3.1 Linear Spectroscopy

Linear spectroscopy is a fast method to gain insights of the dipole allowed excited states within the detected spectral range. Here, „linear“ refers to the regime, where the analyzed system's response is proportional to the intensity change of the analyzing electromagnetic field. Typically, it is assumed, that Coulomb and phonon scattering are negligible resulting in the completely re-emitted light of the induced polarization. Furthermore, continuous wave (CW) photoluminescence spectroscopy is introduced in this section, although strictly speaking, it is a non-linear spectroscopic method, applied to analyze the occupied state after excitation. However, both measurements are performed with the same time-integrating setup, suggesting for a combined treatment.

3.1.1 Linear Absorption

The linear absorption setup is depicted in Fig. 3.1. Exclusively, reflective aluminum optics are used, minimizing chromatic aberrations and enabling measurements within the

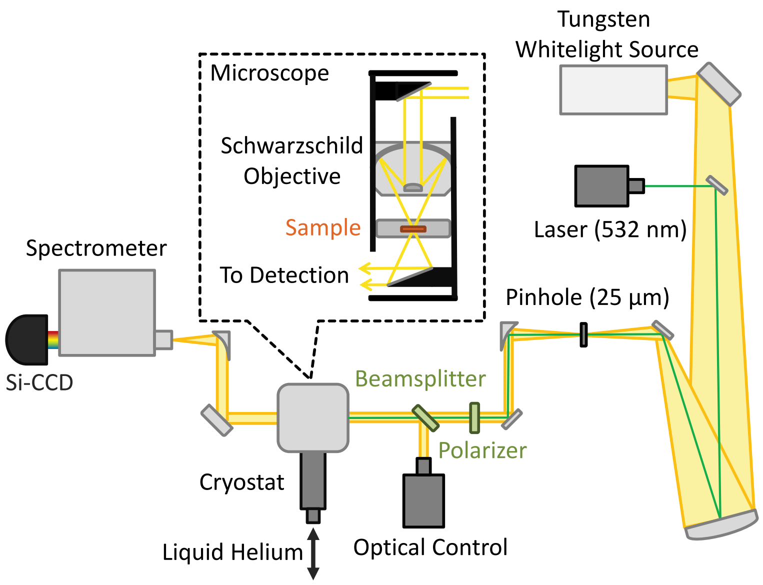

Abbildung 3.1: Linear absorption and CW photoluminescence setup. The customized microscope allows for high spatial resolution ($\leq 2\,\mu$m) and broadband spectral (300 nm-1100 nm) linear absorption measurements. Graphic adapted from Ref. [30].

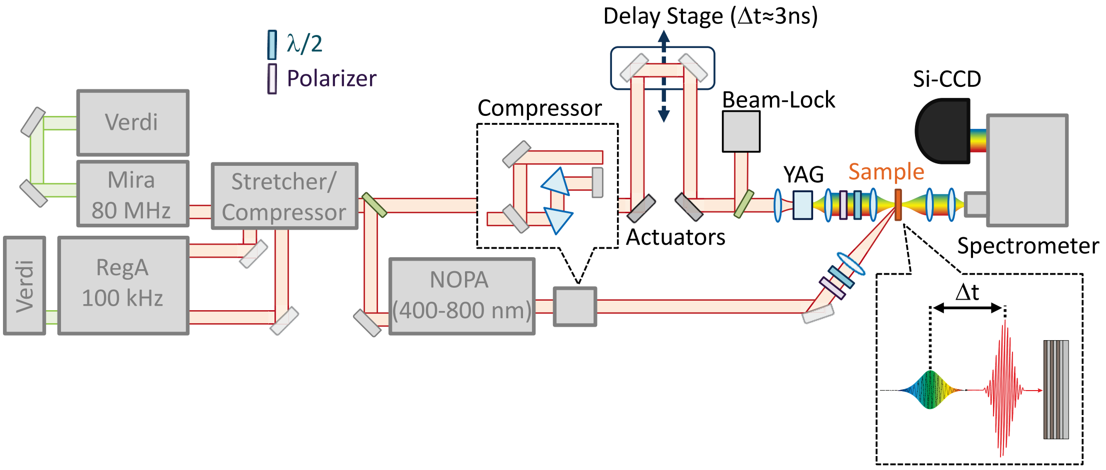

Abbildung 3.2: Schematic pump-probe setup used for time-resolved non-linear optical spectroscopy. It captures the carrier dynamics of the analyzed sample within the probed energy spectrum after optical excitation.

UV[1]-range. A white-light source, switchable between Tungsten filament and Deuterium arc-lamp, is focused onto a pinhole with a diameter of $25\,\mu$m. The pinhole serves as a spatial filter, in first approximation emitting elementary, spherical waves like a point-source. Consequently, after collimation with an off-axis parabolic mirror, where the focal point is positioned at the pinhole, the transmitted radiation is well described by plane waves. Then, the light is focused onto the sample by a Schwarzschild objective[2]. Accordingly, the pinhole is imaged on the sample with the ratio:

$$M \approx \frac{f_{Schw}}{f_{Coll}} = \frac{0.625\,cm}{5\,cm} = \frac{1}{8}. \tag{3.1}$$

As a result, the spotsize on the sample is around $3\,\mu$m. After passing through the sample, the transmitted light is focused on a spectrometer, where it is dispersed and detected by a thermo-electrically cooled (TE-cooled) Silicon charge coupled device (CCD) chip (1024x512px) with a spectral resolution of 1 nm.

The sample can be mounted into a customized liquid-Helium flow cryostat, where a temperature range from 10 K to 500 K can be mapped. Between collimating mirror and Schwarzschild objective, i.e., before the sample, additional optics can be included, such as polarizers and filters. Furthermore, an optical control is implemented, where the sample surface is imaged by a camera, using the Schwarzschild objective in combination with a beam-splitter. Especially, in the case of temperature dependent measurements, when the cryostat's cold finger contracts or expands and the sample position is inevitably changed, it is crucial to relocate the initial position in order to gain comparable results.

The absorption measurement is performed in normal incidence, eliminating angle-dependent polarization effects and simplifying the evaluation. In general, the absorption (A) is given by:

$$A = 1 - T - R, \tag{3.2}$$

---

[1] ultra-violet radiation (here, potentially 170 nm-380 nm)

[2] NA=0.35

with the transmission (T) and the reflection (R). In this setup, essentially the transmission of the sample is measured as follows:

$$\frac{T_{sample} - T_{Bg}}{T_0 - T_{Bg}}. \tag{3.3}$$

In first approximation, the reflection is considered as a flat constant background, which is subtracted after measurement. Then, by applying Lambert-Beer's law[31, 32]:

$$\begin{aligned} \frac{T_{sample}}{T_0} &= \exp\left(-\alpha L\right) \\ \rightarrow \quad -ln\left(\frac{T_{sample}}{T_0}\right) &= \alpha L \end{aligned} \tag{3.4}$$

the extinction αL^3 is determined, where α is directly related to the imaginary part of the refractive index (see Ch. 2).

3.1.2 Continuous Wave Photoluminescence

In the setup, a frequency-doubled Nd:YAG laser is implemented, which is aligned into the same optical path as the white-light by a flip-mirror (see Fig. 3.1). The laser combines two-aspects: firstly, it visualizes the analyzed sample position within the optical control, secondly, it is utilized as a pump source for photoluminescence measurements with an excitation energy of 2.33 eV. The intensity is tuned by neutral density filters placed between collimating off-axis parabolic mirror and Schwarzschild objective. Then, the emitted light is measured by the same detection scheme as the linear absorption, except for the band-pass filter, which eliminates transmitted and scattered laser stray-light resulting from the excitation.

The photoluminescence is detected in transmission geometry, i.e., the emitted photolumiscence of the sample is transmitted through the sample and its substrate before it is detected. As a result, the substrate needs to be transparent within the expected spectral region of the emitted photoluminescence. Otherwise, it is reabsorbed before

---

[3] In its application in solution, α is the product of the extinction coefficient ϵ_λ times the molar concentration c, while L refers to the length of the cuvette.

leaving the sample and cannot be detected. Nevertheless, even when the substrate is transparent, the sample, as the source of the photoluminescence, is not; the detected photoluminescence is spectrally shaped by the absorption of the sample, artificially enhancing the intensity distribution to the Stokes-shifted components. This effect is avoided in reflection geometry. Since, parts of this work deliberately covers only the Stokes-shifted components, this setup is sufficient.

Furthermore, by the evaluation of the detected photoluminescence, it has to be taken care of the wavelength to energy scale conversion. In the detection a grating is utilized for spectral resolution, making use of the wave properties of light. The dispersed light is then measured by the equidistant pixels of the CCD detector, hence, the detected light intensity is measured over equidistant wavelength intervals:

$$f(\lambda)d\lambda. \tag{3.5}$$

The wavelength to energy conversion is given by:

$$E = \frac{hc}{\lambda}, \tag{3.6}$$

accordingly, the detected intensity has to be converted as follows, applying energy conservation:

$$f(E)dE = f(\lambda)\lambda \tag{3.7}$$

$$\rightarrow \quad f(E) = f(\lambda)\frac{d\lambda}{dE} = f(\lambda)\frac{d}{dE}\left(\frac{hc}{E}\right) = -f(\lambda)\frac{hc}{E^2}. \tag{3.8}$$

The minus sign can be ignored, as it merely reflects the different directions of integration in wavelength and energy.[33] Consequently, both, scale and measured intensity have to be adapted when switching from wavelength to energy scale. However, this is only relevant for absolute measurements covering a broad spectral range, thus, absorption and change of absorption measurements as well as measurements of laser-line spectra are not affected.[34]

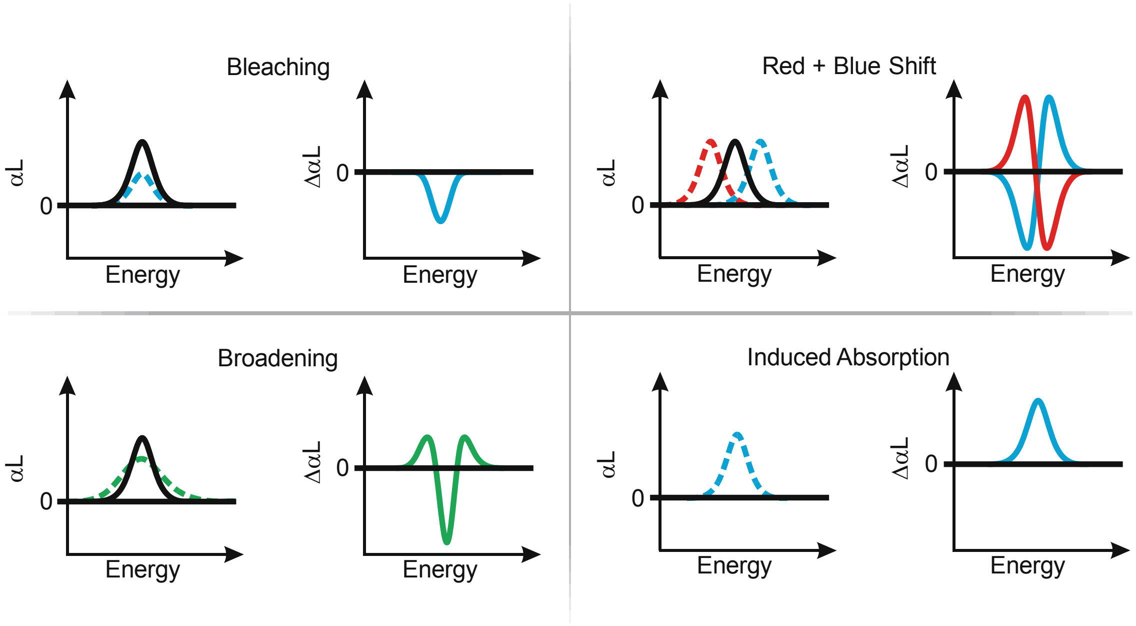

Abbildung 3.3: The four fundamental $\Delta\alpha$L-signals frequently observed in pump-probe-spectroscopy. Typically, a superposition of these signatures is measured increasing its complexity.

3.2 Pump-Probe Spectroscopy

Powerful tools to learn more about electronic excitations and their underlying dynamics are non-linear spectroscopic methods. As the term „non-linear“ suggests, high intensity light sources are necessary to conduct these experiments. Our goal is to analyze the carrier dynamics after optical excitation within a bulk material. Consequently, two conditions have to be fulfilled, besides the excitation of carriers: firstly, excited carriers have to be made „visible“ and, secondly, they have to be monitored time resolved. This is accomplished by time-resolved pump-probe spectroscopy, where two laser pulses are deployed to pump and probe the material system. The spectrally narrow, high intensity pump pulse excites the sample at a desired energy, so that the induced high polarization density within the material system experiences significant amount of scattering and incoherent carriers are created. The excited carriers invoke changes in the linear absorption of the sample, which are captured by the delayed broadband, weak probe pulse.

The principle of pump-probe spectroscopy with the experimental setup is depicted in Fig. 3.2. As an analogy, one can think of shaking a snow globe and filming the falling snow flakes; shaking the snow globe is equivalent to the excitation induced by the pump pulses, the stirred and falling snow flakes resemble the relaxing carriers and the recording camera shots are comparable to the delayed probe pulses.

The time delay between both laser pulses is set by a delay stage, tuning the optical path length in either the pump or the probe arm. In our case, the step size of the stage ($6\,\mu$m) allows for a potential time-resolution of 20 fs by a maximum adjustable time delay of 3 ns.

The actual measurement of the change of absorption ($\Delta\alpha$L) is performed as follows: the transmission of the sample (T_{pr}) is recorded by the probe pulse, while the pump pulse is blocked by a shutter. Then, the transmission of the excited sample is recorded (T_{ppr}), i.e., both, pump- and probe-arm are open. The $\Delta\alpha$L is determined by the ratio of both signals:

$$\frac{T_{ppr}/T_0}{T_{pr}/T_0} = \frac{T_{ppr}}{T_{pr}} = \frac{\exp\left(-(\alpha L + \Delta\alpha L)\right)}{\exp\left(-\alpha L\right)} = \exp\left(-\Delta\alpha L\right) \tag{3.9}$$

$$\rightarrow \quad \Delta\alpha L = -\ln\frac{(T_{ppr} - T_p)}{(T_{pr} - T_{bg})}, \tag{3.10}$$

where in the last row, additionally, the background (T_{bg}; both arms closed) and the pump background (T_p; probe arm closed) are subtracted, correcting for ambient light, as well as photoluminescence and Rayleigh scattering from the sample's surface.

Typically, the detected $\Delta\alpha$L-signals are complex differential absorption signatures demanding to interpret. As a starting point, essentially four fundamental $\Delta\alpha$L-signatures can be distinguished, sketched in Fig. 3.3 with their corresponding initial (solid line) and changed (dashed line) absorption resonances. When a resonance loses oscillator strength due to excited carriers, it is observed as a purely negative $\Delta\alpha$L-signal after spectral integration, and known as bleaching. Bleaching is a direct consequence of the fermionic nature of electrons, where the Pauli-principle inhibits occupation of identical quantum states. Typically it follows, that bleaching of a resonance indicates its population by excited carriers. However, in the case of excitonic transitions the population of the 1s-state also induces bleaching in the 2s-transition, yet, with a reduced factor.[35] Thus, bleaching of a transition does not necessarily mean, that it is occupied, but solely, that it is no longer available.

Further frequently observed signatures are shift signals, where the original resonance is either shifted to lower or higher energies. Here, the oscillator is strength is not changed resulting in $\Delta\alpha$L-signals with equal amounts of positive and negative amplitudes and the spectral integration yields a zero. Shift signals are observed, when the Coloumb potential is changed, in our case, due to excited carriers. In inorganic semiconductors, higher order Coloumb correlations can either induce blue- or red-shifts depending on the specific material system.[36, 37, 38]

Broadening of a resonance is the result of excitation induced dephasing (EID), i.e., the dephasing time of a polarization (T_2-time) is reduced due to increased Coloumb-scattering with excited density. Again, the oscillator strength is not changed and spectral integration yields a vanishing $\Delta\alpha$L-signal. A comparable effect is observed, when going from liquid-He temperatures to room temperature, where the resonances are severly broadened by phonon scattering.

The fourth fundamental signature is induced absorption; it can be considered as the reverse of bleaching, where new transitions emerge after excitation. Induced absorption originate from second order transitions, these include two photon absorptions or excitations of excited carriers into higher states. Hence, unlike the previous signatures, they are not correlated with any resonance of the linear response. Spectral integration yields an overall positive $\Delta\alpha$L-signal.

Unfortunately, nature is never simple and generally a superposition of the fundamental $\Delta\alpha$L-signals is observed. Therefore, extraction of transients from the $\Delta\alpha$L-signals have to be performed carefully, where spectral integration is usually inevitable in order to gain viable results.

3.3 Pump-Probe Setup

The pump-probe setup is seen schematically in Fig. 3.2. In this section the essential elements of the setup and their function are introduced. A Ti:Sapphire amplifier system serves as the source for the experiment. It starts with a frequency doubled, diode pumped Nd:YAG laser, which pumps the passively mode-locked Ti:Sapphire oscillator. The oscillator emits 100 fs short laser pulses with a tunable central wavelength between 700 nm-1000 nm and a repetition rate of 80 MHz. The output power is ≈1 W, where only one fifth is used for seeding the amplifier. The amplifier itself is a Q-switched, cavity-dumped Ti:Sapphire laser with a repetition rate tunable between 10 kHz and 100 kHz. Before the seed pulses are coupled into the amplifier, their pulse length is stretched by gratings in order to avoid laser crystal damage by the high electric fields. After amplification, the energy of the laser pulses are around $10\,\mu$J (100 kHz) in comparison to 12.5 nJ of the oscillator laser pulses. These high pulse energies are necessary to drive the non-linear processes essential for fs-pump whitelight-probe spectroscopy. The exiting pulses are compressed back to the 100 fs by gratings in reverse geometry.

3.3.1 Opto Parametric Amplifier

After the pulse compression the output pulses are split into pump and probe arm. In the pump arm it drives an opto parametric amplifier (OPA), which converts the input pulses with a central wavelength of 800 nm into pump pulses with a central wavelength tunable between 400 nm-800 nm. The tunable central wavelength of the pump pulse allows for excitation energy dependent experiments, furthermore, it guaranties flexibility concerning various material systems with different band-gap energies. The OPA utilizes the χ^2 opto-parametric amplification-process within a crystal, where the photon energy of the input pulse (the „pump“) is transferred to the two output pulses („signal“ and „idler“). In order to achieve high conversion efficiencies, a crystal with a lack of an inversion symmetry is chosen, exhibiting a high χ^2 factor[4]. In the non-

---

[4] Here, a $\beta - BaB_2O_4$ is the crystal of choice.

degenerate case, pump and signal[5] are co-linearly irradiated on the BBO-crystal, where initially difference frequency generation (DFG) generates the idler with the following frequency:

$$\omega_I = \omega_P - \omega_S. \tag{3.11}$$

Subsequently, both, signal and idler are further amplified by the pump, eventually reducing its amplitude. This is the actual opto-parametric amplification, which is described in the simple, stationary dispersion-theory as follows:

$$\frac{\partial A_I}{\partial r} \propto \chi^2 A_S A_P \exp\left(-\Delta k r\right), \tag{3.12}$$

$$\frac{\partial A_S}{\partial r} \propto \chi^2 A_I A_P \exp\left(-\Delta k r\right), \tag{3.13}$$

$$\frac{\partial A_P}{\partial r} \propto -\chi^2 A_I A_S \exp\left(-\Delta k r\right), \tag{3.14}$$

with the complex amplitudes $A_{I;S;P}$ and the phase matching $\Delta k = k_P - (k_S + k_I)$, with the wave-vectors of pump, signal and idler.[39] Evidently, Equation 3.14 shows, that the conversion efficiency is crucially dependent on the phase-matching. Due to the anisotropic dispersion relation ($k_{P;I;S} = \frac{\omega_{P;I;S}}{\nu_{Ph}}$) of the BBO-crystal, the frequency components of signal and idler can be tuned by adjusting the angle of incidence, i.e., adjusting the phase-matching. However, energy conservation (frequency relation in Eq. 3.11) is always fulfilled. At the end, the output pump pulses, now at the desired frequency, are compressed by a prism-pair, compensating for introduced chirp.

3.3.2 White-Light Supercontinuum

The probe pulse needs to be ultrafast (≈100 fs) for the time-resolution and spectrally broad (≈400 nm-1000 nm) for full coverage of the resonances of interest. The whitelight-supercontinuum by self-phase modulation (SPM) fulfills these requirements. It is generated in crystals with inversion symmetry and high χ^3 non-linearity, e.g., Sapphire

---

[5] The signal is selected by phase-matching from a whitelight supercontinuum (cf. Sec. 3.3.2), beforehand generated by the pump.

or Yttrium-Aluminum-Garnet (YAG), by intense laserpulses. Within the crystal the propagating laserpulse with slowly varying envelope $A(t, r)$ can be described in first order dispersion-theory as follows:[39]

$$\frac{\partial A(t,r)}{\partial r} + \frac{1}{\nu_G}\frac{\partial A(t,r)}{\partial t} \propto i\chi^3|A(t,r)|^2 A(t,r), \tag{3.15}$$

with the group velocity ν_G of the laser pulse. After performing the coordinate transformation $\eta = t - r/\nu_G$ a solution of Eq. 3.15 is given by:

$$A(\eta, r) \propto A_0(\eta)e^{i\chi^3|A_0(\eta)|^2 r}. \tag{3.16}$$

Consequently, the phase of the transmitted laser pulse is the following:

$$\varphi(\eta, r) = \chi^3 I_0(\eta) r. \tag{3.17}$$

The time derivative of the phase yields the instantaneous frequency of the propagating laser pulse:

$$\delta\omega(\eta, r) = -\frac{\partial\varphi(\eta,r)}{\partial t} = -\chi^3\frac{\partial I_0(\eta)}{\partial\eta}r. \tag{3.18}$$

Thus, the instantaneous frequency changes linearly with the time-dependent change of the laser pulse intensity. Since, in femtosecond pulses emitted by the amplfifier system the intensity changes rapidly with time, the transmitted probe pulse experiences strong spectral broadening covering several hundred nanometer around the initial central wavelength, typically referred to as whitelight supercontinuum. Additionally, the introduced strong spectral chirp is inevitably connected with strong temporal chirp, so, although spectral contributions of the whitelight supercontinuum exhibit their amplitude maximum only for tens of femtoseconds, overall the pulse length is stretched to over 2 ps.

After generation, the whitelight supercontinuum is focused onto the sample, transmitted, and eventually detected by a spectrometer combined with a TE-cooled Si-CCD camera. The probe spot profile on the sample is a Gaussian distribution with a FWHM

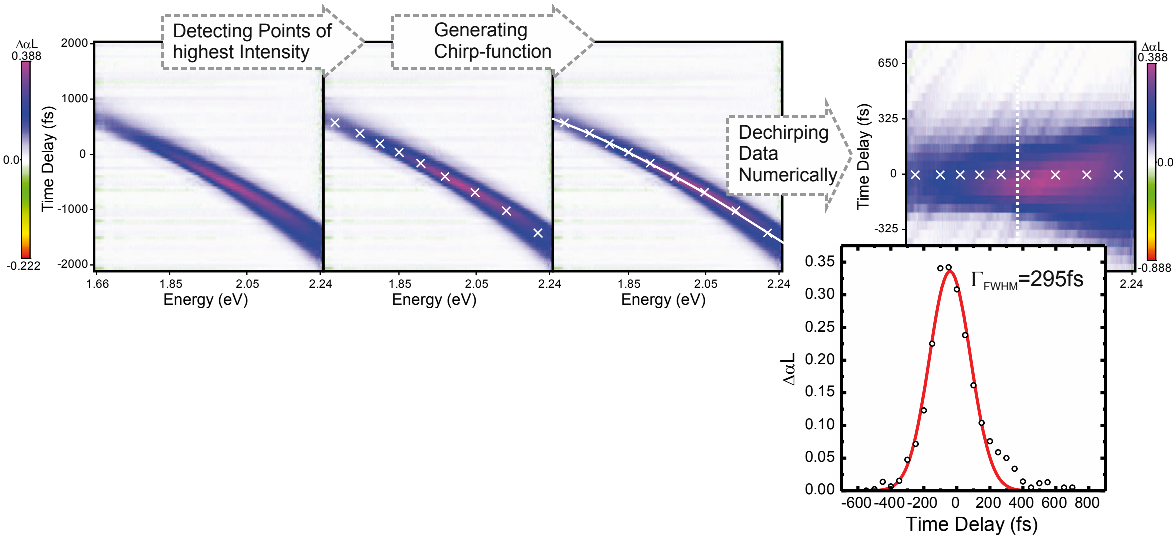

Abbildung 3.4: Evaluation of the whitelight-supercontinuum chirp by two-photon absorption in GaP and the subsequent numerically correction procedure. The extracted cross-correlation (open dots) is fitted with a Gaussian (solid red line) and reveals Γ_{FWHM} ≈295 fs; it gives a conservative estimate of the time-resolution inherent to the experiment.

of 20 μm, while the pump spot size is significantly larger in order to ensure homogeneous excitation within the probed region.

Glen-Laser polarizers in combination with broadband $\lambda/2$-waveplates in both arms are put directly in front of the focusing lenses before sample transmission; it allows for precise adjustment of the polarization state of pump and probe with a contrast of 100:1. Consequently, we can measure the change of absorption spectral-, time- and polarization-resolved.

3.3.3 Chirp

As mentioned in the previous section the generation of the white-light supercontinuum induces a non-linear chirp in the probe pulse. This means, at a distinct time delay not all spectral components within the probe pulse experience their amplitude maximum. In other words, the instantaneous frequency changes with time. Consequently, the time steps performed by the delay stage are not absolute for all spectral components, but relative for one. This leads to temporal distortions within the experimental data in time steps below the envelope function of the probe pulse, i.e., steps below 2 ps around time-zero. By measuring the cross correlation of the pump and probe pulse by two-photon absorption in GaP, the instantaneous frequency is determined by the $\Delta\alpha$L-maximum in the induced absorption at every spectral position (see Fig. 3.4). Then, the maximum of the two-photon absorption signal is set to time-zero correcting for all other optical elements. Consequently, after the correction, all spectral amplitude maxima are located on a horizontal line at zero time delay. The missing time steps at a distinct spectral position are interpolated. This method can be applied as long as the photon energy of the probe pulse lies below the indirect bandgap of GaP at 2.26 eV.[40]

However, the numerical corrections lead to diagonal stripe artefacts resulting from noise in the spectra and are ignored in the following. The whole procedure is shown step-by-step in Fig. 3.4. The determined chirp function is applied to all experimental data correcting for the temporal shifts within the spectral components. It should be noted, that this procedure has to be repeated when changing the spectral window of the probe pulse.

The cross-correlation of the corrected two-photon absorption data yields a Γ_{FWHM} of 295 fs which serves as a conservative estimate of the time resolution for the experimental response (see Fig. 3.4).

4 Frenkel and Charge-Transfer Excitons in Perfluoropentacene

In organic crystals consisting of closed shell molecules, typically, bonding between lattice sites is established by a groundstate energy reduction due to induced dipoles, quadrupoles or beyond, i.e., they consist of van der Waals bonds generally considered as weak. Consequently, in first approximation electron-hole pairs are localized to one lattice site and are referred to as Frenkel excitons. However, in a crystalline environment with the appropriate packing motif the short ranged van der Waals interactions lead to considerable inter-molecular coupling which lift strict localization and a variety of partially delocalized excitons emerge, known as charge-transfer excitons.

In this chapter the linear absorption of PFP single crystals is analyzed crystal axes resolved. A phenomenological interpretation of the various resonances will be given, partially in the context of the Davydov splitting of the exciton band. These analysis serve as a precursor for the following chapter, where the exciton dynamics are examined carefully.

4.1 Perfluoropentacene Single Molecules

Before the measurement and analysis of the linear response of the PFP crystal it is advisable to gain some fundamental insights into the molecule itself. This is especially important for van der Waals bond crystals, where lattice site interactions are weak

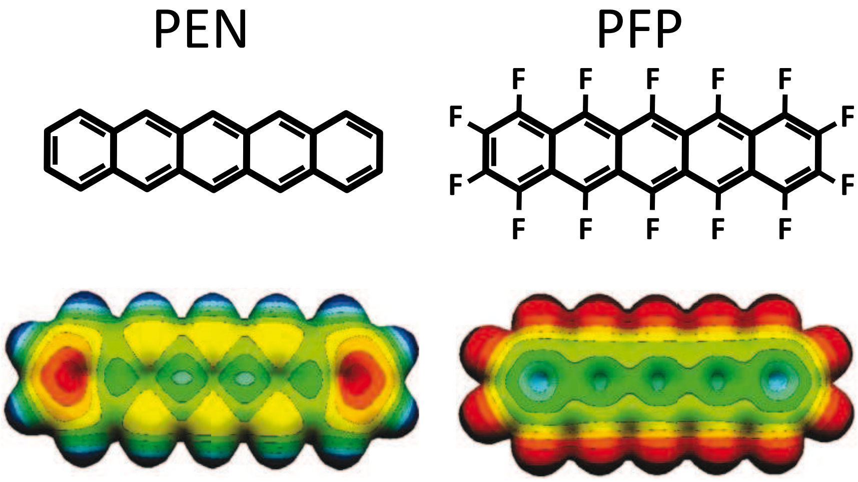

Abbildung 4.1: Schematic structures of PEN and PFP and the corresponding electronic densities mapped as the electrostatic surface potentials. Regions of higher electron density are shown in red and of lower electron density in blue. Adapted and extrapolated from Ref. [42].

and the crystal's linear response may still be dominated by the single molecule, e.g., in benzene crystals.[41] Consequently, a short introduction to the molecular properties of PFP is given followed by an analysis of its gasphase and solution absorption spectra.

4.1.1 Generals

PFP ($C_{22}F_{14}$) is the perfluorinated counterpart of Pentacene (PEN; $C_{22}H_{14}$) and was first synthesized in 2004 by Sakamoto et al.[43] It consists of five fluorinated benzene rings arranged in a planar row, therefore, exhibiting an inversion center. The schematic structures of both molecules PEN and PFP are depicted in Fig. 4.1. Due to the high electronegativity of Fluor in comparison to Carbon[1], the electron density of the delocalized π-system in PFP molecules predominantly reside on the Fluor shell-atoms of the molecule, in contrast to PEN, where the π-system is located on the benzene-rings, i.e.,

---

[1] F=4; C=2.6, on the Allred-Rochow-Scale[44]

the backbone of the molecule. This is shown in Fig. 4.1 below the schematic structures, where the electrostatic surface potential is mapped onto a surface of total electron density (B3LYP/6-1G** Calculation).[42] Another important difference between PFP and PEN is the atomic mass ratio of the basis atoms; Fluor is heavier than Carbon, as a consequence, the atomic-displacement oscillations in a PFP vibron occur mostly within the Carbon rings, whereas in PEN the situation with Hydrogen is vice versa.[20] Figuratively speaking, in PFP the tail wags the dog. Due to the inverse electronic properties of PFP in comparison to PEN, mixed crystals or/and heterostructures on the basis of both molecules potentially pave the way for high-performance, organic pn-junctions.[43]

4.1.2 Linear Absorption

The groundstate of PFP is a closed-shell singlet configuration with the triplet state as the next higher energy level, 0.62 eV above it.[47] Due to negligible spin-orbit coupling, spin is a good quantum number and dipole transitions, e.g. single photon excitations, occur within one spin-system. Consequently, linear absorption of PFP molecules takes place from singlet ground to singlet excited state, where the lowest dipole transition is oriented along the short axis of the molecule ($S_0 \rightarrow S_1$; $1^1A_g \rightarrow 1^1B_{2u}$).[48] In first approximation the triplet states are not addressable, thus, considered as dark states, which makes an experimental determination of their transition energies challenging. For instance, in PEN, the lowest triplet state is determined to be at 0.85 eV by electron energy loss spectroscopy.[49]

A straight forward approach to linear absorption of single PFP molecules is in solution, e.g., in Dichlorobenzene as a solvent. However, due to the dielectric environment of the surrounding solvent molecules, the transitions of PFP molecules experience a shift to lower energies, known as the solvent shift (cf. Ch. 2). In gasphase absorption the dielectric environment is eliminated and the absorption spectrum is solvent shift free with the draw-back of highly broadened resonances resulting from the high temperatures necessary for sublimation. For a rigorous single molecule study with the possibility to resolve rotational transitions, more effort has to be put into the experimental prepe-

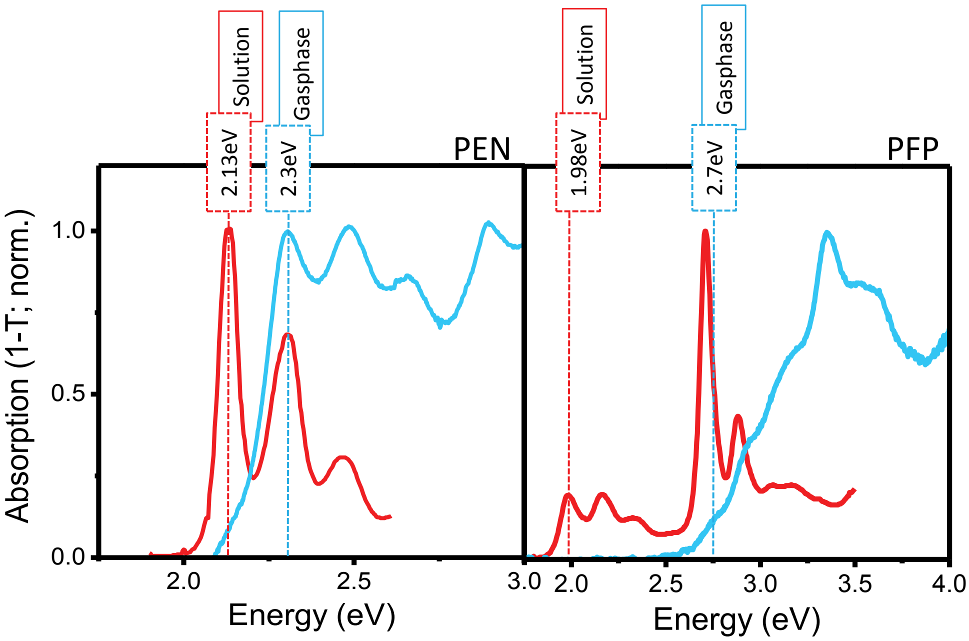

Abbildung 4.2: Solvent shift comparison of PEN and PFP. The gasphase absorption spectra were taken at a temperature of 600 K (adapted from Ref. [45]). The solution spectra were taken at room temperature with Dichlorbenzene as a solvent (adapted from Ref. [46]).

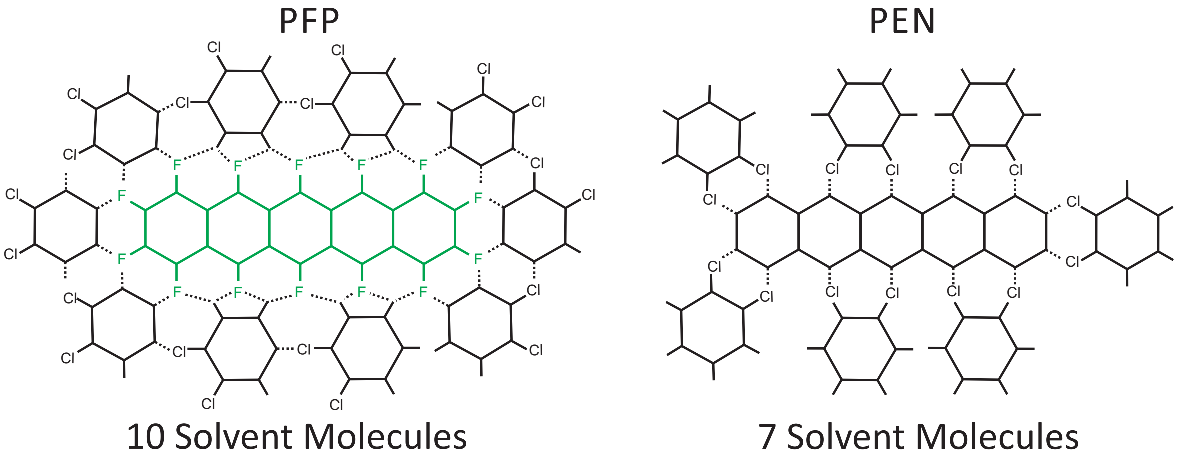

Abbildung 4.3: Tentative explanation for the larger solvent shift of PFP in Dichlorobenzene. 10 solvent molecules can be bound by hydrogen bonds in PFP in comparison to only 7 in PEN.

rations. Such methods are: molecular jet spectroscopy [50] (drawback: ensemble measurement), noble gas matrix spectroscopy [51] (drawback: partially ensemble measurement, dielectric environment) or near-field scanning microscopy of dispersed solution [52] (drawback: dielectric environment). Anyhow, solution and gasphase absorption are sufficient to get first insights into the linear response of single PFP molecules.

The results of the solution and gasphase absorption measurements are presented in Fig. 4.2 and compared to PEN. As expected, the PEN solution spectrum shows the well known solvent shift [53], which amounts to 170 meV. According to Ref. [54], in the situation where solvent and solute molecules are both non-polar the red shift is associated solely to the polarization effect of the surrounding solvent molecules, i.e., it depends on the refractive index of the solvent, while the vibrational progression is retained. In the case of PFP, with more than 700 meV the solvent shift is significantly larger, although the same solvent is used. Thus, the interaction of solvent and solute molecules goes beyond the polarization effects of a surrounding dielectric media. So called Hydrogen bonding is an explanation for the large solvent shift; it is also assumed to be responsible for different shifts of different electronic transitions within a solute molecule absorption spectrum.[54] In Fig. 4.3 the maximum amount of Hydrogen bonds are depicted for PFP and PEN in 1,2-Dichlorobenzene; apparently, more bonds are formed in the case of PFP where additionally a stabilization between the solvent molecules is established. This clustering increases the solvent-solute interaction and lowers the transition energy leading to a larger solvent shift in PFP.

In Fig. 4.4 (a) the gas phase absorption of PFP is shown with a Lorentzian fit of the second electronic transition. By subtraction of the Lorentzian the superimposed lowest electronic transition with its vibronic progression is gained; the result is shown in Fig. 4.4 (b).[2] The gas phase spectrum exhibits a vibronic spacing of $\approx 170 \pm 10$ meV which is 1372 cm^{-1} and corresponds well to the measured and calulated mode with one of the highest Huan-Rhys factors in PFP.[42][20][55] In solution (shown in Fig. 4.4 (c)) the spacing of the progression is slightly increased with the resonances being less broadened due to lower temperatures. As there are several modes involved in the optical response and the resolution is not sufficient, the direct origin of the slight increase

---

[2] This offset correction is only a qualitative guide-to-the-eye, since a correct correction requires a full vibronic Poisson model of both electronic transitions.

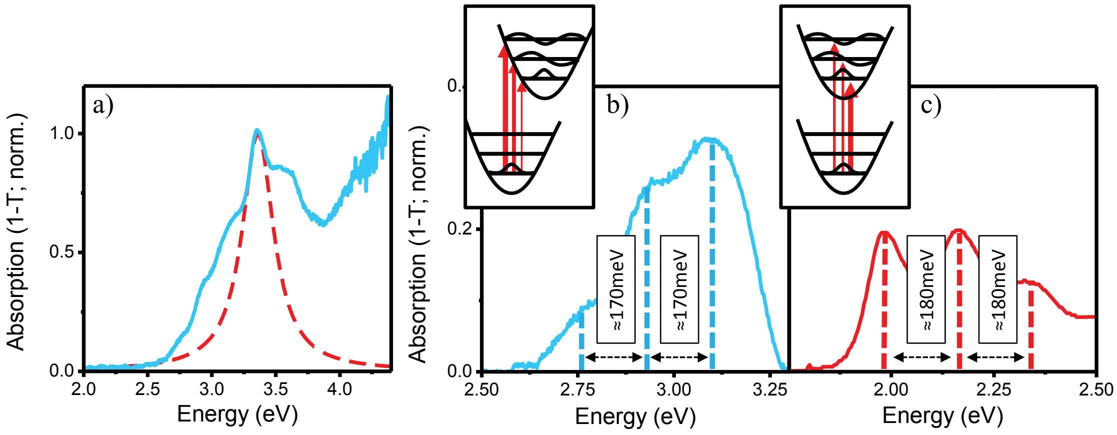

Abbildung 4.4: (a) Lorentzian fit (dashed red line) of the second dipole-allowed electronic transition ($S_0 \rightarrow S_3$) in the gasphase (solid blue line). (b) Extracted lowest electronic transition ($S_0 \rightarrow S_1$) with its vibronic progression in the gasphase by subtraction of the Lorentzian fit. (c) Lowest electronic transition ($S_0 \rightarrow S_1$) of PFP in Dichlorbenzene solution. The insets depict a tentative explanation for the redistribution of the oscillator strength in the context of the Franck-Condon principle.

remains unclear. Strikingly, in the gas phase, the distribution of oscillator strength between the three resonances is significantly altered. We observe a redistribution of oscillator strength to higher energies. Tentatively, it is attributed to a relative shift between the ground and excited state potential sketched in the insets of Figs. 4.4 (b) and (c). Accordingly, applying Franck-Condon's principle, the overlap integrals of ground and excited wavefunctions shift towards higher excited vibronic states which yields higher oscillator strength at higher energies. At the same time the overlap with lower vibronic states is reduced, hence, a reduction of the oscillator strength of the lower resonances is observed. The ratio of the peak amplitudes imply a high Huan-Rhys factor beyond 1. However, the Lorentzian subtraction is not the most elegant method, therefore, molecular jet spectroscopy at liquid helium temperatures would be necessary to verify this hypothesis.

4.2 Perfluoropentacene Single Crystals

Having established an idea of the single-molecule optical-response, we can focus on the single crystal response with its enriched complexity due to anisotropic coupling between nearest neighbor molecules and new crystal symmetries. One key question is the coupling of the translational unequal basis molecule within the unit cell, i.e., the Davydov splitting which has so far not been identified in PFP. The road to success will be polarization resolved linear absorption measurements of PFP single crystals grown on the alkali halide substrates NaF(100) and KCl(100). Unlike previous works the single crystal domains are large enough to optically address them and measure each crystal axis individually.[46] The PFP samples were grown and characterized by Dr. Tobias Breuer and Prof. Gregor Witte from the molecular solids group in Marburg.[56]

4.2.1 Growth and Characterization

PFP exhibits an inverted quadrupole-moment compared to PEN, which is a direct result of the inverted electron density distribution of the π-system. Nonetheless, on weakly interacting substrates, PFP adopts a herring-bone structure[3] within the thin film phase, similar to PEN.[43] Yet, the two basis molecules show a nearly rectangular herring-bone angle of 91.2° (e.g., see Fig. 4.5 (a)), which is considerably higher than the angle in PEN with 51.2°. It will be shown, that this feature has intriguing effects on the electronic excitations within the PFP crystal.

The PFP thin films are prepared on the alkali halide substrates NaF and KCl, where not only macroscopic PFP single crystal growth is possible, but also the crystals exhibit two different orientations (standing vs. lying[4], cf. Figs. 4.5 and 4.6). The growth procedure and characterization is given in detail in Ref. [56], in the following, only a small excerpt is given.

The alkali halide surfaces were prepared by cleaving slices of about 2 mm thickness

---

[3] Here, monoclinic lattice with crystal basis consisting of two translational nonequivalent molecules.

[4] Note, strictly speaking they exhibit four orientations with two on every substrate, however, within the substrate plane they are rotationally equivalent, e.g., see Fig. 4.5(c).

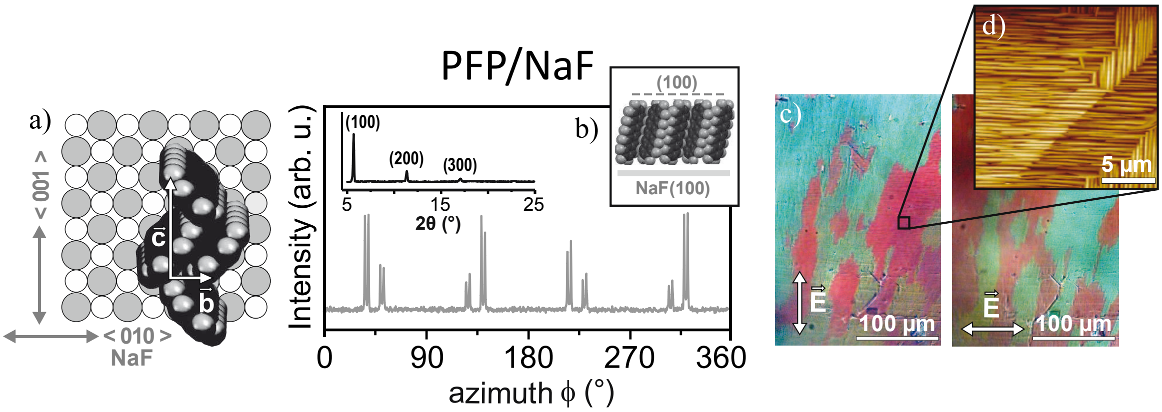

Abbildung 4.5: (a) Sketch of the PFP crystal orientation on the NaF(100) substrate. (b) X-Ray Diffraction patterns of the PFP thin film on NaF(100): specular scan (left inset) and azimuthal scans along $(112)_{PFP}$ and $(11\text{-}2)_{PFP}$. (c) Microscopic image for perpendicular set polarizations, revealing single crystal domains with 90° lateral rotation. (d) AFM micrographs of the PFP thin films. The image is aligned along the substrate's [100] direction. Adapted from Ref. [56].

from a single-crystal rod. Subsequently, the highly-crystalline PFP (purity $> 99\%$) thin films (150 nm) were prepared under ultra-high-vacuum conditions by molecular beam deposition onto KCl(100) and NaF(100) surfaces. The molecules assemble in an upright fashion with their $\vec{b}$- and $\vec{c}$-axes parallel to the surface on NaF(100) (cf. Fig. 4.5(a)) while a recumbent orientation is adopted on KCl(100) yielding the $\vec{a}$- and the $\vec{b}$-axes of the PFP lattice parallel to the substrate surface (cf. Fig. 4.6(a)).

The film morphology was characterized by atomic force microscopy at ambient conditions. Exemplary film morphologies are depicted in Figs. 4.5 (d) and 4.6(d). They show islands with preferred orientations along the NaF<100> and KCl<110> directions. Due to the fourfold symmetry of the substrates, four 90°-rotated domains are found.

The crystalline orientation of the samples was determined from X-Ray Diffraction (XRD) data. Bragg-Brentano scans of PFP/NaF(100) are given in Fig. 4.5 where the PFP(n00) diffraction peaks are clearly observed. These lattice planes correspond to uprightly oriented molecules as shown schematically in the inset. Additionally, azimuthal scans of lattice planes which are not parallel to the substrate have been performed

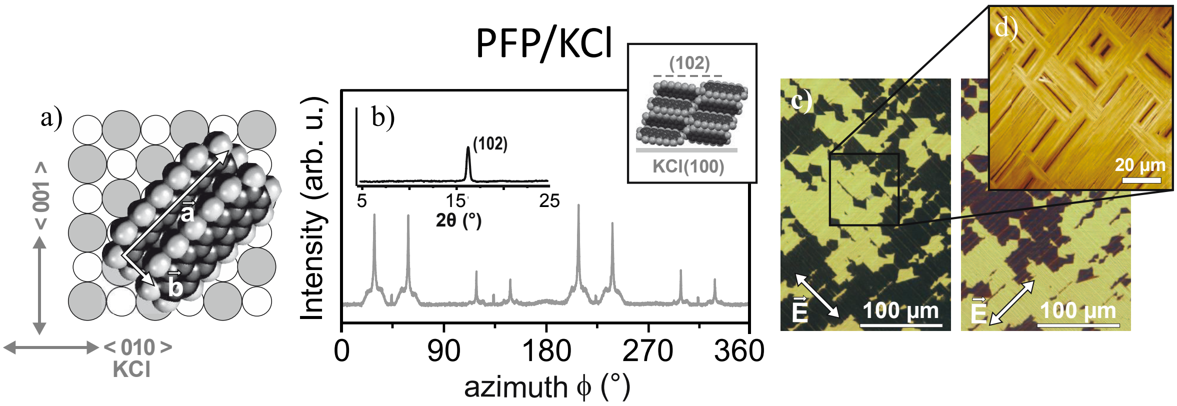

Abbildung 4.6: (a) Sketch of the PFP crystal orientation on the KCl(100) substrate. (b) X-Ray Diffraction patterns of the PFP thin film on KCl(100): specular scan (left inset) and azimuthal scans along $(112)_{PFP}$ and $(11\text{-}2)_{PFP}$. (c) Microscopic image for perpendicular set polarizations, revealing single crystal domains with 90° lateral rotation. (d) AFM micrographs of the PFP thin films. The image is aligned along the substrate's [100] direction. Adapted from Ref. [56].

to determine the exact lateral arrangement. A scan of the PFP(112) and (11-2) lattice planes (which are recorded simultaneously due to their similar lattice spacing) yields 16 peaks. After elimination of the peaks resulting from the fourfold-symmetry and the mirror-domains, two peaks with a mutual splitting of $\Delta\Phi$=3.1° remain. Subsequent consideration of the relative orientation between the projection of the lattice plane onto the PFP(100) lattice plane allows to determine the orientation of the unit cell axes on the surface. This yields that the molecular $\vec{b}$-axis are oriented along the [100] directions of the substrate with a slight misorientation of $\Phi = \pm 1.55°$. The epitaxial alignment of the film as well as the slight misorientation are attributed to the nearly perfectly equivalent values of the PFP $\vec{c}$-axis (4.49 Å) and the distance of two sodium atoms along the NaF <100> directions (4.62 Å).

Figure 4.6(b) presents the X-ray diffraction patterns of PFP deposited on KCl(100). Here, the (102) peak is observed, which corresponds to a lying orientation of the molecules. An evaluation of the azimuthal distribution of (012) and (01-2) peak intensities yields that the molecular $\vec{b}$- and $\vec{a}$-axis are oriented along the substrate's <110> direc-

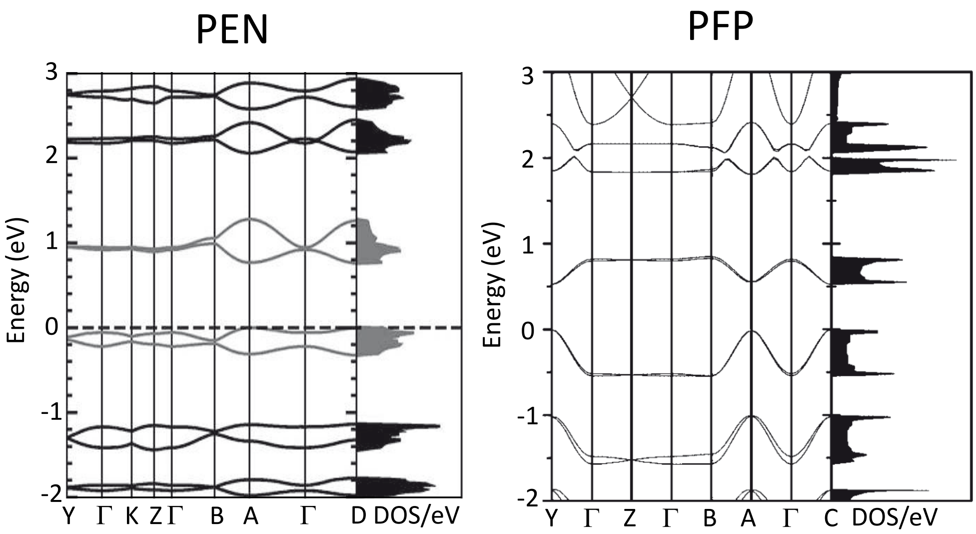

Abbildung 4.7: Bandstructure calculations of PEN (Campbell phase calculation from Ref. [57]) and PFP (thin film phase calculation from Ref. [42]) crystals.

tion. The adoption of a recumbent orientation on this surface is attributed to higher order commensurability in the following direction: $15d_{KK} = |4\vec{a}_{PFP} - 2\vec{c}_{PFP}|$. Figures 4.5 (c) and 4.6 (c) show microscope images of the sample taken by T. Breuer with a polarization filter. Clearly, the individual single crystal domains are seen extending over several tens of micrometers. Therefore, in combination with the experimental spot sizes, which are below $20\,\mu$m, it is possible to address the individual transition dipole moments along the three crystal axes in PFP. This has been successfully exploited to characterize the vibronic Davydov splitting in PFP.[20]

In ideal crystals with periodic boundary conditions electronic excitations can be expressed in terms of Bloch waves, i.e., the wavevector $\vec{k}$ of the electrons is a good quantum number. Accordingly, the dispersion relation (bandstructure) can be calculated along the high symmetry points within the first Brillouin zone. Such calculations have been performed for PEN and PFP and are shown in Fig. 4.7. Typical for organic semiconductors, the bandwidth of the HOMO and LUMO band are in both cases narrow with less than 500 meV. On the other hand, distinct differences are present between PEN and PFP. In PEN a clear splitting of the bands is observed, which is virtually absent in PFP. The bandsplitting in PEN is a direct consequence of the coupling between the two basis molecules, i.e., the Davydov splitting. Consequently, calculations predict a vanishing Davydov splitting for PFP crystals. Furthermore, the bands in PFP are predominantly flat except for symmetries along the slip stacked direction, where as far as organic semiconductors are concerned strong dispersion is predicted. In PEN such a monodirectional dispersion is not observed; the small dispersion present is distributed over several directions. Hence, in PFP we expect one-dimensional excitons partially delocalized along the slip stacked packing motif.

4.2.2 Polarization-Resolved Linear Absorption

The absorption measurements are performed with the setup shown in Fig. 3.1 at liquid Helium temperatures in order to reduce homogeneous broadening due to phonon scattering. At first, the measured linear responses are assigned to the three crystal axes. Due to the unique growth characteristic of PFP on NaF and KCl in normal incidence all three axes are accessable. Thus, the assignment is performed by comparing the linear responses of PFP on both substrates ($\vec{b}$- and $\vec{c}$-axis in PFP/NaF(100); $\vec{b}$- and $\vec{a}$-axis in PFP/KCl(100)) as it is shown in Fig. 4.8. Since the dipole moment of the HOMO-LUMO transition ($S_0 \rightarrow S_1$) resides within the short axis of the molecule, the absorption along the $\vec{a}$-axis virtually vanishes and therefore, is not included in this figure. The remaining response along the $\vec{b}$-axis of PFP/KCl(100) serves as the reference to identify the $\vec{b}$-axis in PFP/NaF(100). The blow out shows the high energy part of the spectra starting at 2.25 eV. Here, the $\vec{b}$-axis response of PFP/KCl(100) shows vanishing absorption, whereas one crystal axis spectrum of PFP/NaF(100) exhibits a clear absorption band with presumably a vibronic progression. Accordingly, the linear absorption with the high energy absorption band can be assigned to the $\vec{c}$-axis of PFP. Having successfully assigned the spectra, an overview of the linear absorptions along all three crystal axis of PFP is given in Fig. 4.9. Additionally, the solution absorption spectrum is included as a grey shaded area for reference. The transition at 1.95 eV in the crystal phase is attributed to the slightly red shifted HOMO-LUMO transition.[43]

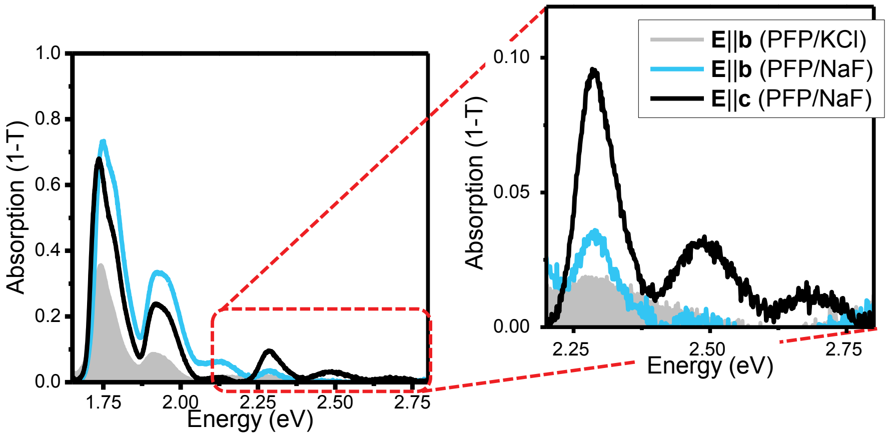

Abbildung 4.8: Crystal axes identification on the basis of the third absorption band in the linear absorptions of PFP/NaF(100) and PFP/KCl(100). A pronounced absorption in combination with a vibronic progression is only observed along one axis in PFP/NaF(100), ergo the $\vec{c}$-axis in PFP.

As mentioned above, the lowest transition virtually vanishes for polarization along the $\vec{a}$-axis, the residual signature is a result of the small tilt angle which the molecules adapt in respect to the $\vec{a}$-axis. The second electronic transition dipole moment is oriented along the long axis of the molecule, thus observed along the $\vec{a}$-axis with no apparent solvent to crystal shift. In the following we will focus on the lowest transitions in the spectral range from 1.6 eV to 2 eV.

Interpretation in the Context of the Davydov Formalism

A detailed view of the lowest transitions observed along the $\vec{b}$- and $\vec{c}$-axis is given in Fig. 4.10. Three distinct resonances are identified in the spectra, where the lowest two are attributed to the Davydov-split Frenkel excitons in the traditional manner between the two basis molecules (X_1 and X_2). In the scheme the dipole coupling is depicted as vector additions (in-phase and out-of-phase) of the molecular dipole moments resulting in two exciton bands, as described in Ch. 2. However, the splitting amounts to only 25 meV, which is significantly smaller than the 120 meV in PEN and corroborates

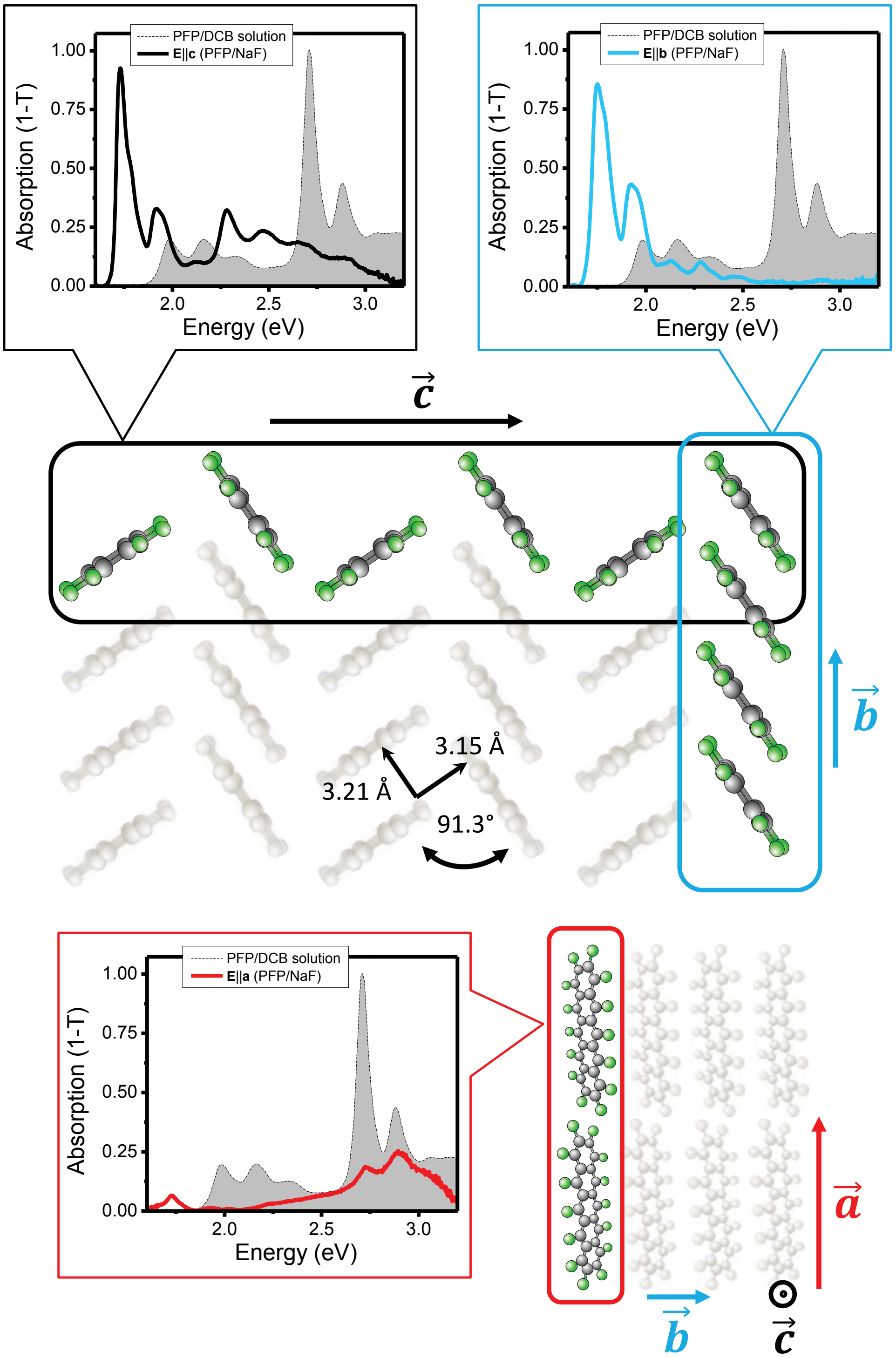

Abbildung 4.9: Overview of the linear absorptions along all three crystal axes.

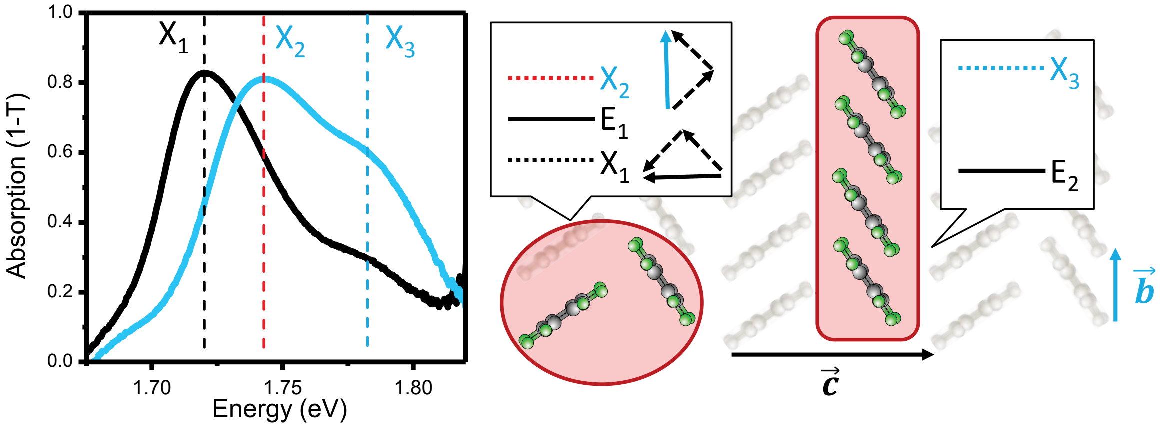

Abbildung 4.10: Three excitonic resonances identified in the polarization resolved linear absorption of PFP/NaF(100) single crystals with an interpretation in the context of the Davydov splitting.

the theoretical prediction of weak coupling between the basis molecules. It has been shown, that in theory, dipole coupling alone is not capable of quantitatively reproducing experimental results.[58] The second ingredient for the correct description of the Davydov splitting is mixture of Frenkel and charge transfer (CT) states between the two translational nonequivalent molecules. In Tetracene, not including charge transfer states lead to a minimal Davydov splitting of 4 meV (experiment 78 eV) and with the wrong sign. With the inclusion of CT-states quantitative agreement is achieved revealing CT admixture in the lowest transitions of up to 30%.[58] The decisive parameters for mixing between Frenkel and CT-states are the Frenkel exciton dissociation integrals D_e and D_h which are in good approximation the electron and hole resonance integrals t_{LUMO} and t_{HOMO} defined by the molecular orbitals between nearest neighbors.[58] For PFP crystals in Ref. [42] all nearest neighbor resonance integrals are performed revealing negligible charge transfer resonances between the two nonequivalent basis molecules. Consequently, the observed Davydov splitting solely originates from the dipole coupling explaining its factor 5 reduced splitting compared to PEN. Furthermore, it is highly improbable that CT states between these molecules exist. This is in contrast to PEN, where theoretical calculations predict a planar delocalization of the lowest excitons.[59][23][21]

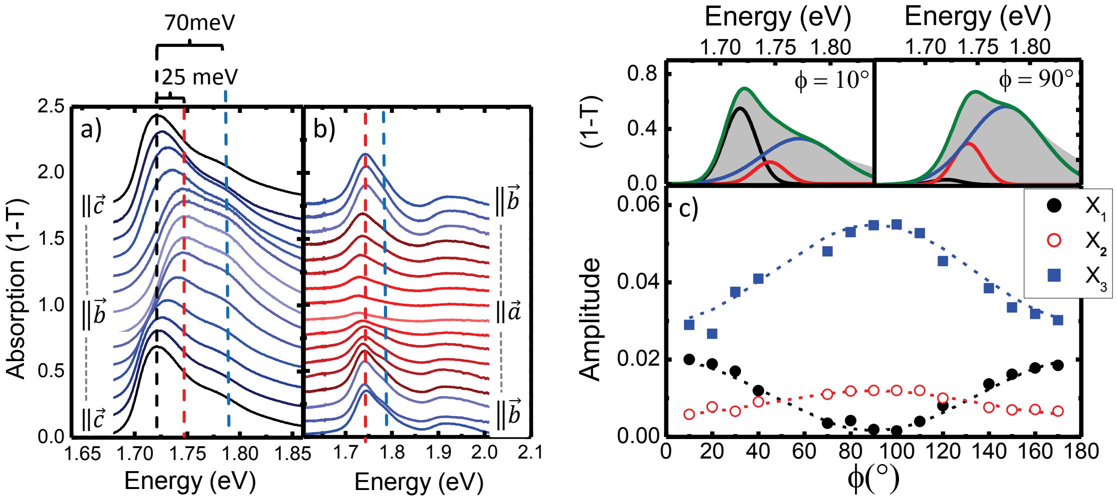

Abbildung 4.11: (a) Polarization resolved linear absorption of PFP/NaF(100) single crystals. (b) Polarization resolved linear absorption of PFP/KCl(100) single crystals. (c) Gaussian fits of the three identified exciton resonances with their amplitudes plotted over the polarization angle showing the $\cos^2(\phi)$ dependence typical for dipole coupling.

On the other hand, the resonance transfer integrals between molecules within a sublattice of PFP crystals exceed the ones in PEN by nearly a factor 2 (PFP: t_e=73 meV, t_h=-132 meV; PEN: t_e=81 meV, t_h=85 meV)[5].[42] Accordingly, both electron and hole are mobile within the slip stacked direction. Since the third peak does not coincide with an internal or external vibron it is attributed to an exciton resonance (X_3) partially delocalized along the $\vec{b}$-axis. Typically the oscillator strength of CT excitons are considered as weak [58], here however, the state resides only 45 meV above the Frenkel exciton resonances in comparison to 290 meV in PEN [60] which implies strong mixing between these states and therefore an increased oscillator strength. Along the $\vec{c}$-axis its oscillator strength is severely reduced and probably vanishes completely in ideal PFP crystals, hence, the dipole moment is predominantly oriented along the slip stacked direction as expected from the calculated transfer integrals.

In Fig. 4.11 the polarization dependent linear absorptions are given for PFP/NaF(100) and PFP/KCl(100) at 10 K. The three identified excitonic resonances are fitted with

---

[5] The maximum values from all crystalline directions are given.

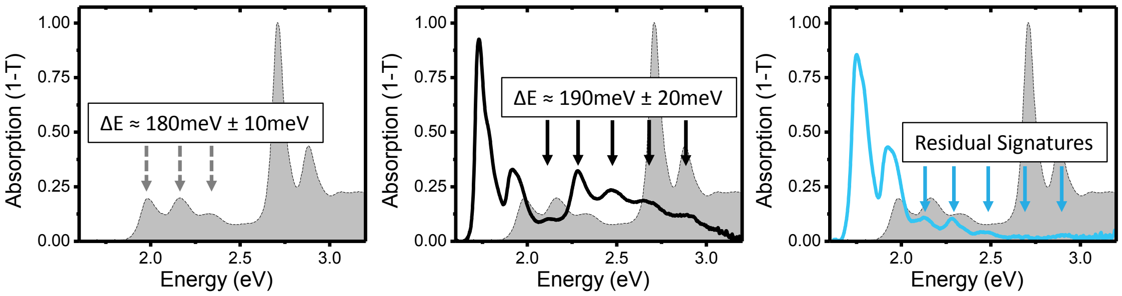

Abbildung 4.12: Comparison of the vibronic progression at 2 eV in solution and in crystalline phase along the $\vec{c}$-axis of PFP. Along the $\vec{b}$-axis these signatures are suppressed.

three Gaussian forms where all parameters are kept constant except for the amplitude. In Fig. 4.11 (c) the two fits along the $\vec{c}$- and $\vec{b}$-axis ($\phi = 10°$; $\phi = 90°$) are given as an example. The amplitudes of the three resonances extracted from the fits are plotted as dots against the polarization angle where polarization along the $\vec{c}$-axis is set to zero. They show a $\cos^2(\phi)$ behavior illustrated by the dashed-line fits in very good agreement with classical dipole coupling (cf. Ch. 2).

Now that the lowest excitonic resonances are identified we focus on the higher absorption band, which is dominant along the $\vec{c}$-axis. In Fig. 4.12 the two linear absorptions along the $\vec{b}$- and $\vec{c}$-axis are compared to the linear absorption of PFP in solution. Apparently, the absorption band at 2.3 eV present along the $\vec{c}$-axis resembles the lowest transition with its vibronic progression of PFP in solution, however, with shifted energy spacing between the progressions and an overall shift to higher energies. This is unexpected, since in a diffusive background with dense packing the increased polarizability of the surroundings typically induces a shift to lower energies, as it is the case from gas phase to solution absorption. Along the $\vec{b}$-axis only residual signatures of the higher band are present, yet, an increased oscillator strength at the 1.95 eV HOMO-LUMO transition is observed.

Again, considering the packing of the molecules and correspondingly the orientation of their dipole moments, the observed absorption signatures can be interpreted as H- and J-aggregate like transitions. The orientation of the dipole moments within the bc-plane is sketched in Fig. 4.13 with the projected dipole according to the polarization of the incident light. Taking into account dominant dipole coupling between the slip stacked molecules we see that along the $\vec{b}$-axis the dipoles are strung together in a J-aggregate fashion, whereas along the $\vec{c}$-axis an H-aggregate like arrangement is adopted. The J-aggregate (H-aggregate) can be viewed as an extreme case of the Davydov splitting where the higher (lower) transition is dipole forbidden, i.e., a dark state (cf. Ch. 2). On the right hand side of Fig. 4.13 theoretical calculations from Ref. [19] are shown for ideal J- and H-aggregate absorptions with increasing dipole coupling strength. In the calculation electronic coupling to the typically dominant vibron in Oligoacenes at around $1400\,\mathrm{cm}^{-1}$ is included. The corresponding calculated solution spectrum (single molecule absorption) is given as a grey shaded area for reference. The energy shift of the transition resulting from the solid state background is omitted in order to emphasize the effect of the aggregate. In the case of the J-aggregate, already for weak coupling, the progression is suppressed and the lowest transition gains oscillator strength. Furthermore, the absorption band is shifted towards lower energies. As the coupling is increased the vibronic progression virtually disappears and a single resonance prevails. A similar behavior is identified along the $\vec{b}$-axis where the oscillator strength of the transition at 1.95 eV is increased and the higher progressions are reduced in good agreement with the J-aggregate interpretation.

The calculation of an ideal H-aggregate reveals a shift of the absorption band to higher energies, additionally, the initially equidistant energy spacing between the resonances of the progression becomes irregular as well as the oscillator strength. In the case of strong coupling the progression is barely visible, similar to the J-aggregate with one single resonance dominating the spectrum, however, here the peak resides at higher energies. Correspondingly, the absorption band at 2.3 eV observed along the $\vec{c}$-axis is attributed to an H-aggregate like absorption with intermediate dipole coupling.

Due to the double molecular basis in PFP crystals an ideal J- or H-aggregate situation cannot capture the complexity of the absorption spectrum.[19] Nevertheless, both crystal axes exhibit qualitatively the expected features, leading us to the conclusion of enhanced dispersion along the slip stacked direction as it is predicted by theory.

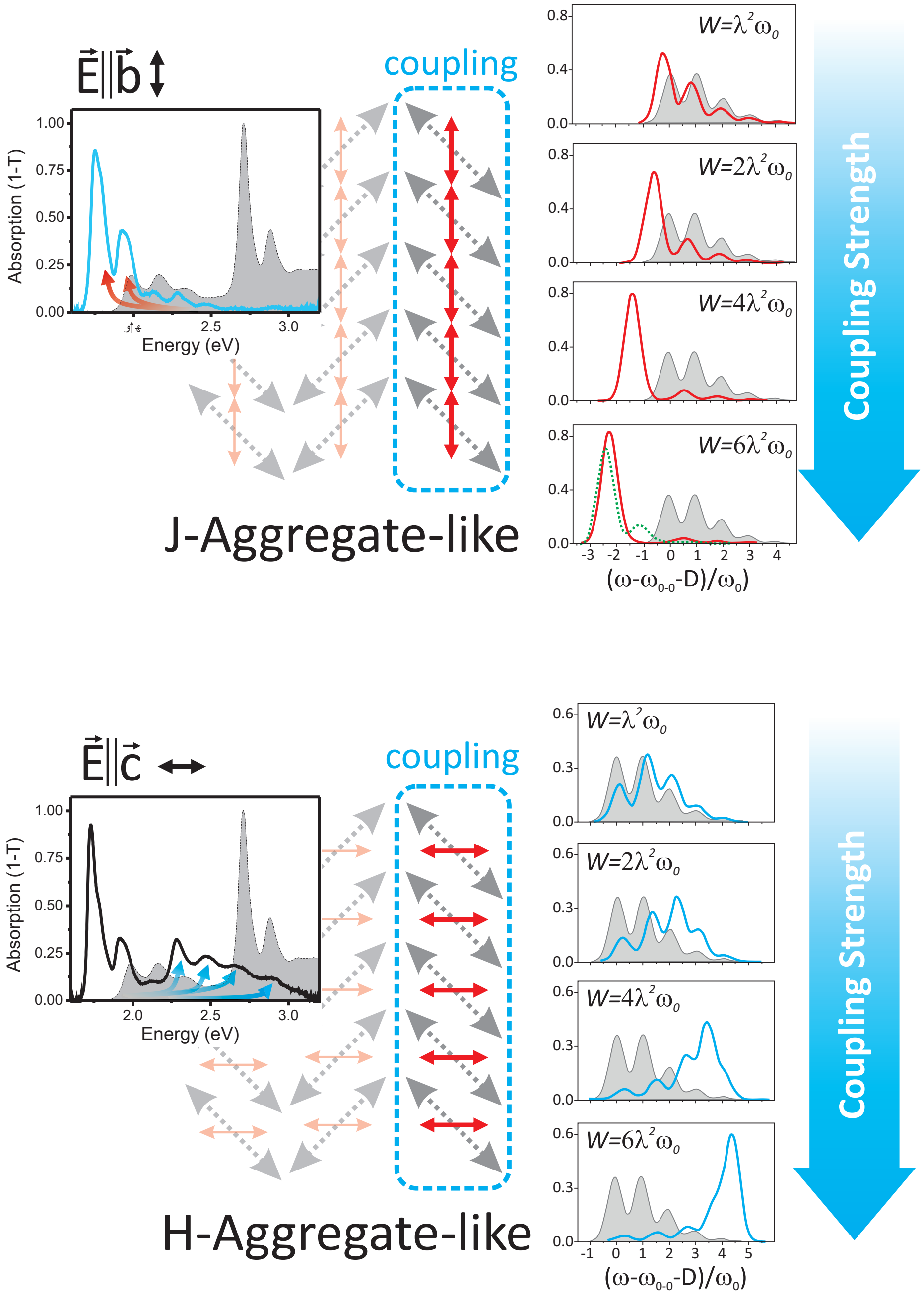

Abbildung 4.13: Polarization-dependent coupling of the slip-stacked molecules along the $\vec{b}$-axis. On the right hand side, theoretical absorption spectra for ideal J- and H-aggregates with increasing coupling strength J_0 are shown in comparison to solution spectra. Adapted from Ref. [19].

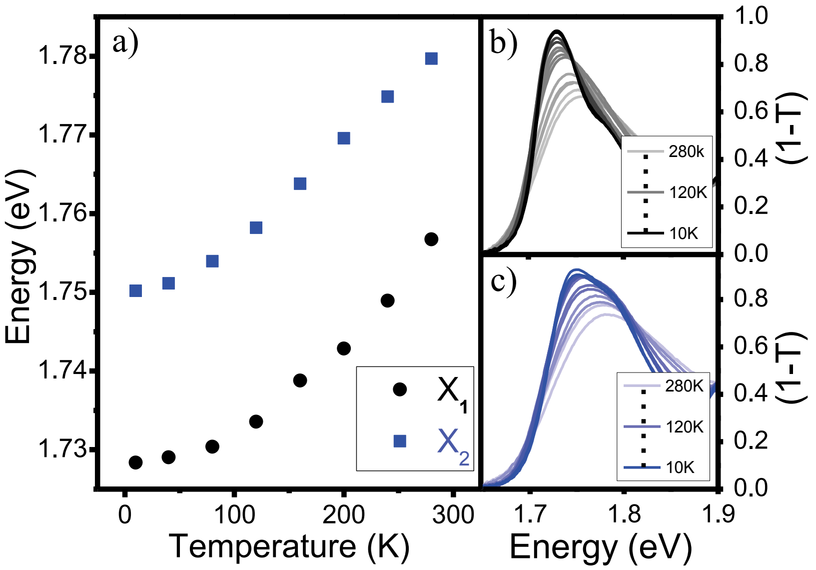

Abbildung 4.14: (a) Temperature dependence of the Davydov components along the $\vec{b}$- and $\vec{c}$-axis from 10 K to 280 K. (b) Temperature dependent linear absorption along the $\vec{c}$-axis. (c) Temperature dependent linear absorption along the $\vec{b}$-axis.

Organic semiconductor crystals have relatively large thermal expansion coefficients in comparison to inorganic semiconductors, e.g., Pentacene exhibits a thermal expansion coefficient along the $\vec{a}$-axis of $\alpha_{\vec{a}} = 1.1 \times 10^{-4}\,\mathrm{K}^{-1}$ in contrast to $\alpha_{ZnO} = 3 \times 10^{-6}\,\mathrm{K}^{-1}$ of ZnO[6].[61] In PFP comparable thermal expansion coefficients are expected because of their close relation. Besides the fact, that a decrease in temperature leads typically to an increased bandwidth [62] resulting from higher orbital overlap and consequently to a reduced bandgap [17], temperature dependent absorption measurements are interesting for possible changes in the crystalline phase which induce different intermolecular spacings and/or altered basis molecule angles. As a result, the modified inter-molecular coupling is directly observable in transmission measurements. For instance, slight changes of the Davydov splitting with temperature occur in Pentacene crystal phases.[61] Thus, temperature-dependent position measurements of the two Davydov components in PFP are monitored in a range from 10 to 300 K. The results are

---

[6] Zinc-oxide

plotted in Fig. 4.14 (a) where the peak position of the lowest component is taken into account. A general red shift of the bandgap with decreasing temperature is observed attributed to reduced inter-molecular spacing, i.e., denser molecular packing ergo higher coupling. The measured shift of ≈30 meV exceeds reported values for Pentacene by a factor of 3.[61] Tentatively, this indicates a higher thermal expansion coefficient in PFP.[7] However, the Davydov splitting remains the same within the experimental error. Hence, a drastic change of the angle between the two basis molecules is ruled out. Furthermore, the resonances exhibit an expected increased homogeneous broadening at elevated temperatures evoked by an increased phonon population.

---

[7] Note however, that the temperature dependent bandgap shift is not linear with the inter molecular spacing, so a direct correlation between expansion coefficient und bandgap shift is not possible.

5 Exciton Dynamics in Perfluoropentacene

In the previous chapter the linear response of PFP was analyzed, showing distinct excitations along the three crystal axes. Based on a phenomenological interpretation, there are strong indications of a 1D partially delocalized exciton within the $\vec{b}$-axis. Preliminary ab-initio calculations come to similar conclusions. A way to gather more information about the nature of the optical excitation and its dynamics are the application of non-linear spectroscopic methods. Here, the method of choice is time-resolved pump white-light probe spectroscopy, since it is a powerful tool to study the incoherent carrier dynamics. In this chapter a rigorous analysis of the carrier dynamics during the first nanosecond after excitation in PFP is given, including all three crystal axes. The results are discussed in the context of singlet exciton fission via excimer formation; both processes have been observed (singlet fission) or proposed (excimer formation) in the closely related PEN crystal. Consequently, the chapter starts with an overview of the observed and proposed dynamics in PFP related crystals. Some of the concepts are then applied to the results and reviewed accordingly.

5.1 Decay Mechanisms in Organic Semiconductors after Optical Excitation

This section covers briefly some of the most frequently occurring decay mechanisms observed in crystalline organic semiconductors. The major part of this section is dedicated to singlet fission, which has gained some reviving attention lately, due to its potential to overcome the Shockley-Queisser limit in organic solar cells.[63] The subsections dealing with the several decay mechanisms are ordered in their chronological occurrence after optical excitation, as far as possible. Since no time-resolved spectroscopic analysis on PFP exists so far, decay mechanisms of related crystals, e.g. Anthracene, PEN and Perylene, are reviewed. An overview of the primary decay mechanisms in these three model systems is given in Figs. 5.1,5.12,5.7. These figures are not exhaustive and should only guide through proposed and accepted relaxation processes after optical excitation. Moreover, they only refer to the documented decay mechanisms of the crystalline phase, the solution and the gas-phase of these materials show completely different decay times and mechanisms and are not treated in this work.

5.1.1 Excimer Formation

The word „excimer“ is derived from „excited dimer“, meaning a shared excitation between two monomers. The simplest known case is the Helium excimer.[64] In the ground state of the hypothetical He_2 molecule, the anti-bonding character[1] of the $1s\sigma^{*2}$ molecular orbital outmatches the binding character of the $1s\sigma^2$ orbital. Consequently, the energy potential between both atoms is repulsive in the ground state, i.e. the binding is energetically unfavorable. However, in the case of an excited He atom the population of the orbitals in the He_2 molecule is as follows: $1s\sigma^2 1s\sigma^{*1} 2s\sigma^1$. The anti-binding character is decreased, while simultaneously increasing the binding character by populating $2s\sigma$. As a result, the excited He_2 molecule is energetically favorable compared to two separate He atoms, with one being in the ground state and the other one in the first

---

[1] Anti-bonding orbitals are marked with a star.

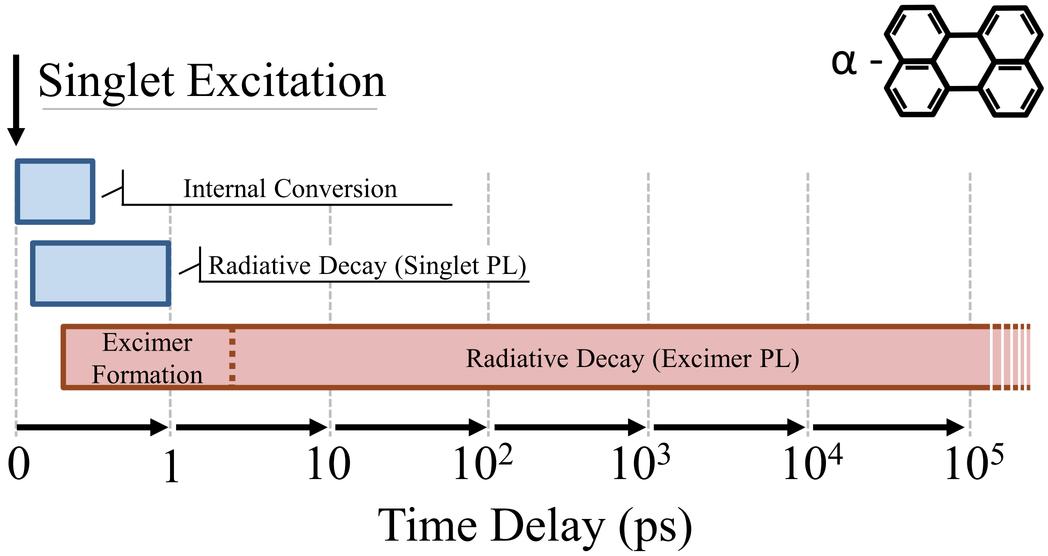

Abbildung 5.1: Decay mechanisms of the α-Perylene crystal, a prominent example of excimer formation.

excited state.

The relaxation back to the ground state happens radiatively. Since the ground-state potential is purely repulsive, the emitted radiation is usually broadband featureless luminescence, peaked at the excited potential's minimum. This can be easily seen in the energy level diagram in Fig. 5.2 (a), where $R_{A,B}$ (Å) is the general reaction coordinate, in this case the average distance between the two He nuclei. The actual binding energy levels are far more complicated, where mixing of orbitals due to spin-orbit coupling, vibrational and rotational states have to be considered. The He_2 excimer states are, as all rare gas excimer states, of the Rydberg type. This means, that predominantly the bonding character of the ion pair (He_2^+) is responsible for the excimer formation. The Rydberg electron[2] wavefunction is diffuse and has only little bonding or anti-bonding contributions. Nonetheless, the bonding states are influenced to some extent. Especially at long internuclear separations, where the Rydberg electron starts to screen the ion significantly, deviations between the ion pair and Rydberg states are observed.[65] In Fig. 5.2 (b) the lowest Rydberg levels of the Ne_2 excimer are shown with their corre-

---

[2] The electron, which is excited to higher states

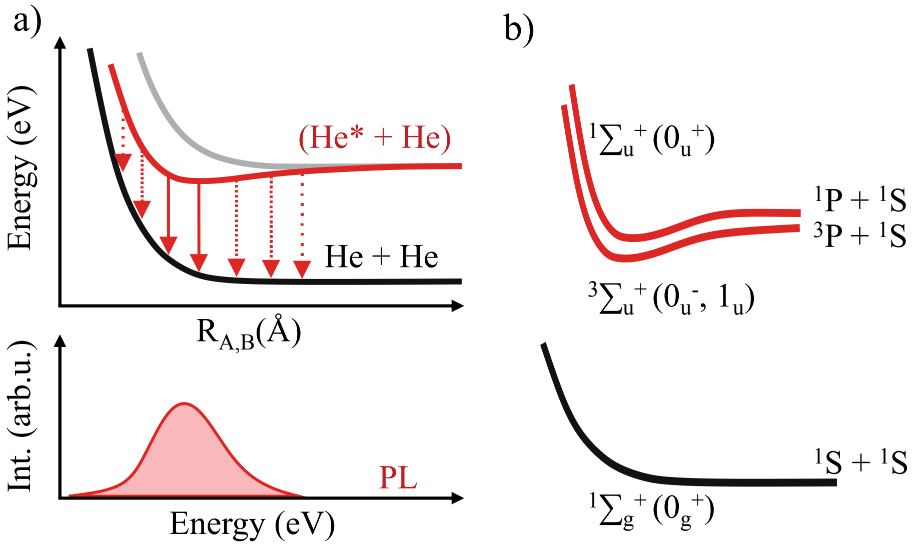

Abbildung 5.2: (a) Simplified He excimer energy level diagram, with the resulting featureless radiative decay. (b) Repulsive ground state and lowest excited Rydberg states of the Ne_2 excimer with the corresponding molecular orbitals (orbitals with spin-orbit coupling in brackets) and resulting states after dissociation. Vibrational and rotational states are ignored. Adapted from Ref. [66].

sponding orbital notation according to Hückel's case *a* and *b*, i.e., no spin-orbit coupling, and in brackets to Hückel's case *c*, i.e., with spin-orbit coupling. Vibrational and rotational states are omitted. It has been shown that spin-orbit coupling mixes Singlet and Triplet states in two of the three lowest lying Rydberg states (in 1_u and 0_u^+), which results in initially forbidden dipole allowed transitions from free atomic ground to bound excimer states. However, the transition probabilities are crucially dependent on the internuclear separation, with vanishing transition matrix elements at the lowest excimer binding lengths. This is the reason for the relatively long relaxation times of the several excimer states (≈90ns) even being considered metastable in the 1_u state.[67] In general, one distinguishes between three extreme cases of bonding excimer states: the previously described Rydberg, covalent and charge transfer states. As the molecular excimer states probably primarily contain Rydberg and charge transfer states or a mixture of both, the treatment of the covalent excimer type is omitted. The reader

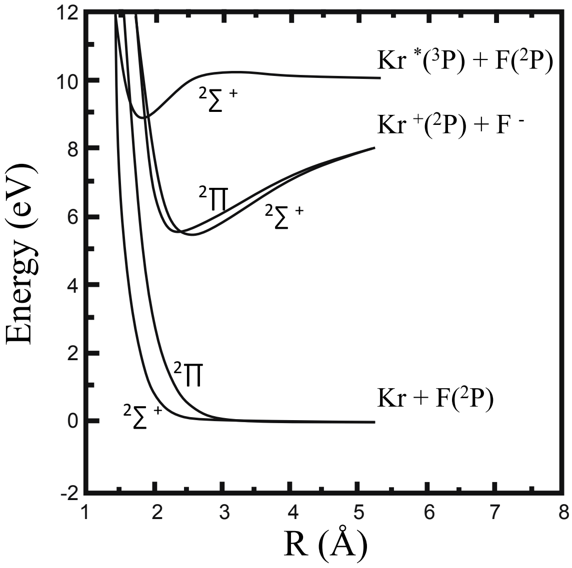

Abbildung 5.3: Energy level diagram of the lowest KrF dimer states without spin-orbit coupling. Adapted from Ref. [68].

interested in covalent excimer states is referred to Ref.([65]).

Prominent examples of charge transfer excimers (also called ion pair excimers), are rare gas-halides, such as KrF or XeF. Ignoring charge transfer mixing or van der Waals interaction, one finds a purely repulsive ground state, due to the exchange repulsion of the F valence electrons with the closed shell of the rare gas. However, if charge transfer mixing is included, the repulsion turning point is shifted towards lower internuclear separations to such an extent, that van der Waals interaction are no longer negligible. Eventually, both contributions lead to a bonding ground state ($^2\Sigma^+$) in XeF with a dissociation energy of 140meV. This configuration is considered to be the most stable charge transfer rare gas halide diatomic complex. In KrF, for instance, the charge transfer contributions cannot overcome the exchange repulsion energy leading to a purely repulsive ground state.[68, 65]

In principal, the lowest excimer states are ion pair states, although one should always keep in mind that potential Rydberg states exist. A simple rule whether the lowest excimer states are of ionic or Rydberg type is to compare the ionization potentials of the participating elements. Regarding HeI, the lowest excited states are Rydberg states, since the ionization potential of I is significantly lower than the one of He. In XeF the situation is vice versa, consequently the lowest states are ion pair states. Nevertheless, this evaluation does not give any information, whether the lowest excited states are bonding or not. In Fig. 5.3 the lowest excimer states (without spin-orbit coupling) of KrF are given as an example. The energy difference of Rydberg and ion pair states in the binding region is more than 3 eV, so that mixing of these states is weak.

One of the early observations of aromatic excimer formation was the concentration dependent change of the Pyrene fluorescence in solution. With increasing concentration the initially violet fluorescence decreased and a featureless blue fluorescence emerged.[69] Later, excimer formation was proposed in several other planar aromatic molecules, e.g. Anthracene and Naphtalene, trying to explain the observation of delayed fluorescence in the gas phase and in solution.[70, 71] Moreover, in Ref.[71] the first consideration was uttered of a possible correlation between a singlet excited dimer and two molecular triplet states, where the latter is populated diabatically by a collision of two molecules in the ground and excited singlet states. This process is nowadays known as singlet fission.

Theoretical Treatment

The theoretical treatment of molecular excimers is still today a subject of scientific research. One key ingredient in the aromatic stabilization is the closed-shell ground state configuration.[64] Therefore, the starting point of the excimer formation is comparable to the rare gas dimers. In aromatic molecules the highest valence electrons occupy delocalized π-orbitals extending over the entire molecule. Accordingly, the anti-bonding π^*-orbitals are the lowest excited states. As a result, one has to deal with two large correlated electron systems interacting with each other.

In the following a brief introduction to an exemplary up-to-date theoretical treatment of aromatic excimers is given. This can be read in more detail in Ref.[72], where it is taken from.

Early ab-initio calculations dealing with aromatic excimers are based on *configuration* *interaction singles* and required empirical corrections only to get qualitive agreement with experiment. Typically, lack of electron correlation treatment is the cause for insufficient results. Recent advances in theoretical methods, e.g. TD-DFT[3] or MRPTs[4], and computational power tackled this issue and enabled quantitive accurate results of excited states in aromatic systems. The presented method MCQDPT[5] is one of the MRPTs known to be successful calculating excited states. As a starting point, the molecular orbitals are separated into active and inactive orbitals. The inactive molecular orbitals are always occupied for the valence states and always unoccupied for the conduction states. Then the complete active space (CAS) is generated by distributing the active electrons in all possible ways among the active molecular orbitals, while the others are kept fixed. The many-body wavefunction is then optimized by employing the complete active space self-consistent field (CASSCF) procedure. After optimization, the wavefunction serves as a reference in order to evaluate the dynamic electron correlation energies by subsequent MCQDPT calculations.

In case of benzene, all bonding and anti-bonding π-orbitals can be treated as active, while in other aromatic molecules already a truncation of the active space is necessary for reasons of insufficient computational capabilities. Thus, only the HOMO and LUMO of the monomer are taken into account, as the related transition is an eligible approximation for the single-electron excitation. The interaction of these orbitals form the four active orbitals of the dimer:

$$(\mathrm{L}+1)_D = \frac{1}{\sqrt{2(1-S_{AB}^{\mathrm{L}})}}\left[(\mathrm{L_A})-(\mathrm{L_B})\right], \tag{5.1}$$

$$\mathrm{L}_D = \frac{1}{\sqrt{2(1+S_{AB}^{\mathrm{L}})}}\left[(\mathrm{L_A})+(\mathrm{L_B})\right], \tag{5.2}$$

$$\mathrm{H}_D = \frac{1}{\sqrt{2(1-S_{AB}^{\mathrm{H}})}}\left[(\mathrm{H_A})-(\mathrm{H_B})\right], \tag{5.3}$$

$$(\mathrm{H}-1)_D = \frac{1}{\sqrt{2(1+S_{AB}^{\mathrm{H}})}}\left[(\mathrm{H_A})+(\mathrm{H_B})\right]. \tag{5.4}$$

---

[3] **T**ime **D**ependent **D**ensity **F**unctional **T**heory

[4] **M**ultireference **P**erturbation **T**heory

[5] **M**ulti**C**onfiguration **Q**uasi-**D**egenerate **P**erturbation **T**heory

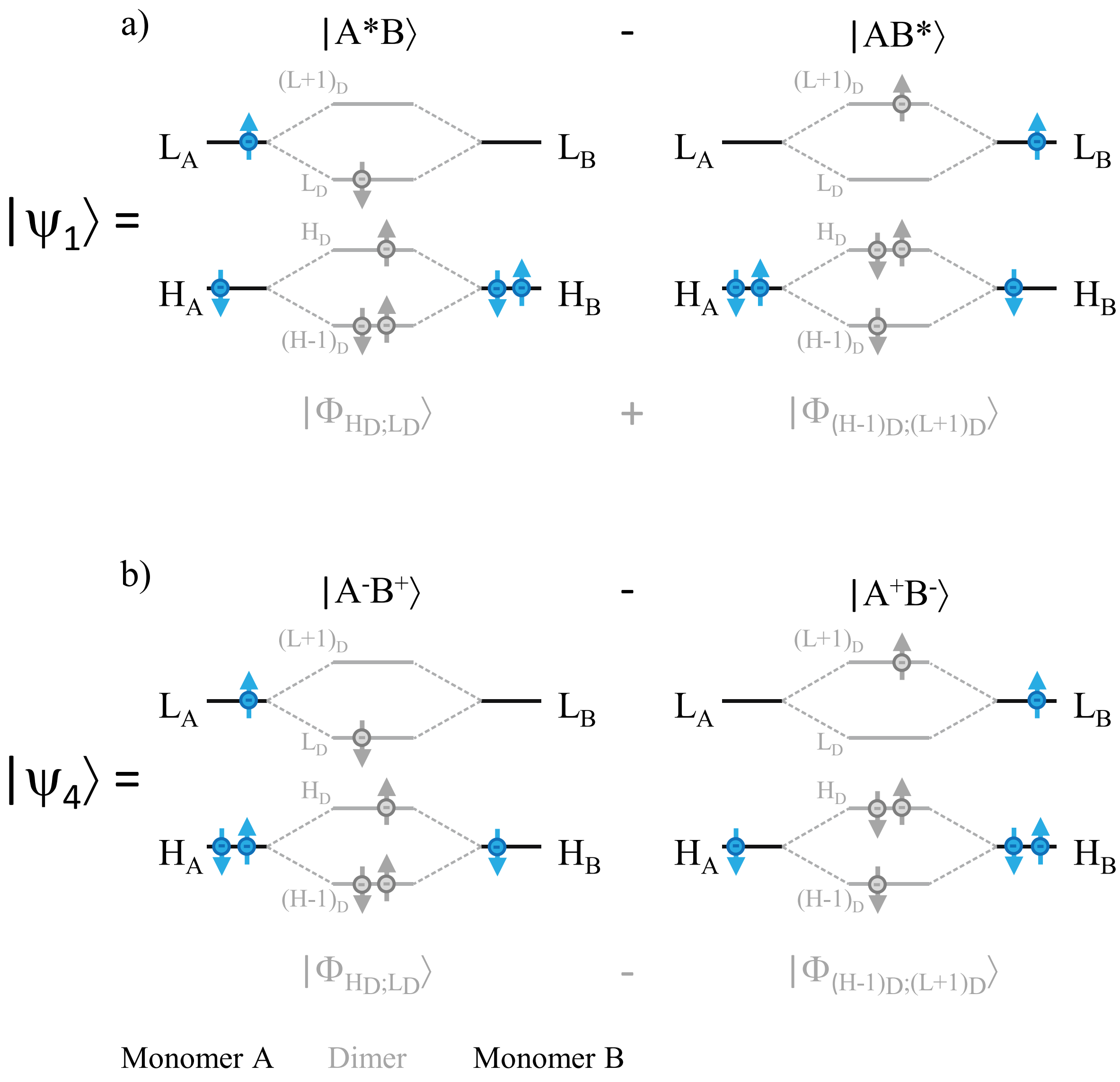

Abbildung 5.4: Two of the four excimer states constructed from the excited monomer states. The dimer states are shown greyed. It should be kept in mind that the sole dimer and monomer states are not equivalent, only the shown linear combinations are. (a) Excimer state related to Frenkel exciton excitation. (b) Excimer state related to charge transfer contributions. Note that in the dimer presentation a separation of these contributions is not possible.

Where $\mathrm{H}_{\mathrm{A,B}}$ and $\mathrm{L}_{\mathrm{A,B}}$ are HOMO and LUMO of molecule A and B and $S_{AB}^{\mathrm{L,H}}$ their overlap integrals. Now utilizing Slater-determinant notations, the single-electron excited states can be written as follows:

$$\left|\Phi_{H_D;L_D}\right\rangle = \frac{1}{\sqrt{2}}\left|(\mathrm{core})(H-1)_D^{\uparrow}(H-1)_D^{\downarrow}\left\{H_D^{\uparrow}L_D^{\downarrow}+L_D^{\uparrow}H_D^{\downarrow}\right\}\right\rangle \tag{5.5}$$

$$\left|\Phi_{H_D;(L+1)_D}\right\rangle = \frac{1}{\sqrt{2}}\left|(\mathrm{core})(H-1)_D^{\uparrow}(H-1)_D^{\downarrow}\left\{H_D^{\uparrow}(L+1)_D^{\downarrow}+(L+1)_D^{\uparrow}H_D^{\downarrow}\right\}\right\rangle \tag{5.6}$$

$$\left|\Phi_{(H-1)_D;L_D}\right\rangle = \frac{1}{\sqrt{2}}\left|(\mathrm{core})H_D^{\uparrow}H_D^{\downarrow}\left\{(H-1)_D^{\uparrow}L_D^{\downarrow}+L_D^{\uparrow}(H-1)_D^{\downarrow}\right\}\right\rangle \tag{5.7}$$

$$\left|\Phi_{(H-1)_D;(L+1)_D}\right\rangle = \frac{1}{\sqrt{2}}\left|(\mathrm{core})H_D^{\uparrow}H_D^{\downarrow}\left\{(H-1)_D^{\uparrow}(L+1)_D^{\downarrow}+(L+1)_D^{\uparrow}(H-1)_D^{\downarrow}\right\}\right\rangle \tag{5.8}$$

The (core) functions are the closed shell orbitals. Due to the linearity of Eqs. 5.1-5.4, the monomer orbitals can be reversely expressed as linear combinations of the dimer orbitals, e.g.:

$$H_A = \frac{1}{\sqrt{2}}\left\{\sqrt{1+S_{AB}^{H}}\,(\mathrm{H}-1)_D+\sqrt{1-S_{AB}^{H}}\mathrm{H}_D\right\}. \tag{5.9}$$

Therefore, single-electron excitations can also be expressed in terms of the monomer orbitals, e.g.:

$$\left|A^{*}B\right\rangle = \frac{1}{\sqrt{2}}\left|(\mathrm{core})H_B^{\uparrow}H_B^{\downarrow}\left\{H_A^{\uparrow}L_A^{\downarrow}+L_A^{\uparrow}H_A^{\downarrow}\right\}\right\rangle, \tag{5.10}$$

$$\left|A^{-}B^{+}\right\rangle = \frac{1}{\sqrt{2}}\left|(\mathrm{core})H_A^{\uparrow}H_A^{\downarrow}\left\{H_B^{\uparrow}L_A^{\downarrow}+L_A^{\uparrow}H_B^{\downarrow}\right\}\right\rangle. \tag{5.11}$$

These are again the known description of the Frenkel- and charge transfer excitons in a dimer from the previous chapter. Since, in a dimer they are indistinguishable excitations, the spatial- and spin-symmetry adapted excited states are constructed from the determinants in Eqs. 5.5-5.5 as follows:

$$|\Psi_1\rangle = \frac{1}{\sqrt{2}}\left(|\Phi_{H_D;L_D}\rangle + \left|\Phi_{(H-1)_D;(L+1)_D}\right\rangle\right) = \frac{1}{\sqrt{2}}\left(|A^*B\rangle - |AB^*\rangle\right), \tag{5.12}$$

$$|\Psi_2\rangle = \frac{1}{\sqrt{2}}\left(\left|\Phi_{H_D;(L+1)_D}\right\rangle + \left|\Phi_{(H-1)_D;(L)_D}\right\rangle\right) = \frac{1}{\sqrt{2}}\left(|A^*B\rangle + |AB^*\rangle\right), \tag{5.13}$$

$$|\Psi_3\rangle = \frac{1}{\sqrt{2}}\left(\left|\Phi_{H_D;(L+1)_D}\right\rangle - \left|\Phi_{(H-1)_D;(L)_D}\right\rangle\right) = \frac{1}{\sqrt{2}}\left(\left|A^-B^+\right\rangle + \left|A^+B^-\right\rangle\right), \tag{5.14}$$

$$|\Psi_4\rangle = \frac{1}{\sqrt{2}}\left(|\Phi_{H_D;L_D}\rangle - \left|\Phi_{(H-1)_D;(L+1)_D}\right\rangle\right) = \frac{1}{\sqrt{2}}\left(\left|A^-B^+\right\rangle - \left|A^+B^-\right\rangle\right). \tag{5.15}$$

Hence, within this approximation, four excimer eigenstates exist, with Frenkel (Eqs. 5.12, 5.13) and charge transfer contributions (Eqs. 5.14,5.15). In Fig. 5.4 two of the four excimer states are shown with the corresponding electronic populations. In comparison to the dipole coupled dimer (Ch. 4), here, an additional stabilization is evoked by charge transfer. This happens in two ways; firstly, the intermolecular Coulomb interaction induces an attraction between the electron on molecule A and the hole on molecule B, i.e. a weakly bound charge transfer exciton emerges, secondly, coupling of charge transfer and Frenkel exciton contributions occur, reducing the overall potential.[15] The degeneracies of Eqs. 5.12,5.13 and Eqs. 5.14,5.15 are lifted by dipole and charge transfer interaction, respectively. A similar resonance stabilization is found for the ground-state of benzene, where not only all possible double bonds need to be considered, but also the Dewar- and ionic isomers.[64]

The four states are essential to describe excimer bonding in organic dimers, yet, treating the other monomer orbitals merely as a constant background obviously leads to lower calculation accuracy. The monomer ground states are determined by common DFT calculations, eventually building the dimer states. In the following, the dimer ground and excited states are optimized by CASSCF and simultaneously perturbed using MCQDPT. During these procedures the spatial conformation of monomers and dimer are not changed, leaving them as phenomenological presets. With this method, the calculated energy of excimer photoluminescence for Perylene deviated by 13% from experiments.[72]

As expected, analysis of the bonding excimer state reveals significant admixture of charge transfer contributions. In Fig. 5.5 the weights of the charge transfer and Frenkel

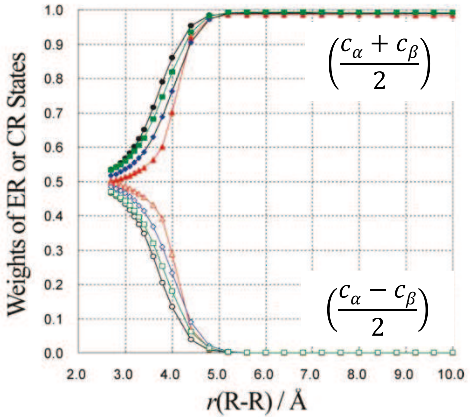

Abbildung 5.5: Weights of the Frenkel- and charge transfer exciton wavefunctions as a function of intermolecular separation. Adapted from Ref.[72].

exciton contributions are shown as a function of intermolecular separation applying the following approximation (from Eqs. 5.12,5.15) for the bonding dimer wavefunction:

$$\begin{aligned} c_\alpha \left|\Phi_{H_D;L_D}\right\rangle + c_\beta \left|\Phi_{(H-1)_D;(L+1)_D}\right\rangle = &\left(\frac{c_\alpha + c_\beta}{2}\right)(|A^*B\rangle - |AB^*\rangle) \\ &+ \left(\frac{c_\alpha - c_\beta}{2}\right)(\left|A^-B^+\right\rangle - \left|A^+B^-\right\rangle). \end{aligned} \tag{5.16}$$

In the binding region, where the nature of the excimer is predominantly governed by the lowest dimer state $|\Phi_{H_D;L_D}\rangle$, strong mixing of the excitonic wavefunctions occur with nearly equal weights. This emphasizes the importance of the charge transfer contributions to the excimer formation.

Excimer formation in α-perylene crystals

Moving from the isolated dimer picture to the crystal, α-Perylene is a prominent system to study excimer dynamics. The α-Perylene crystal exhibits a herringbone structure, where the primitive cell is composed of four molecules arranged in two pairs. The „paired“ molecules face each other with their planar sides, close to an eclipsing conformation. It is within these pairs, where the excimer formation takes place.
The population of the excimer state after excitation happens over a direct and an indirect pathway. The direct population occurs during the first one hundred femtoseconds, shortly after internal conversion steps, while the indirect population follows

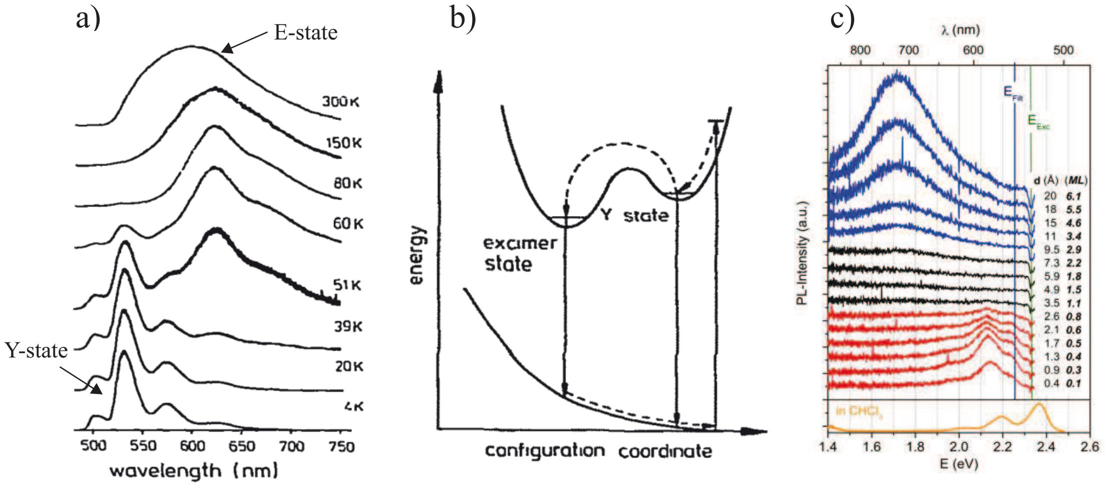

Abbildung 5.6: (a) Temperature dependent photoluminescence of α-perylene. Observation of the transition from E- to Y-state. Adapted from Ref. [73]. (b) Proposed α-perylene excimer relaxation scheme. (c) Change of photoluminescence with PTCDA coverage on mica substrate. Transition from a monomeric, vibronic progression dominated photoluminescence into a bulk, excimer photoluminescence. Adapted from Ref. [74].

with a time constant of 2 ps.[75] The decay of the excimer is primarily radiative with a decay constant of around 100 ns.[76, 73] Temperature dependent photoluminescence studies have shown an odd behavior: with decreasing temperature the featureless excimer fluorescence vanishes and a structured blue-shifted fluorescence emerges, which is sometimes called the Y-state. At liquid Helium temperatures it is assumed, that after excitation and internal conversion the dimer relaxes into the intermediate Y-state, not capable of overcoming the energy barrier to the fully relaxed E-state (see Fig. 5.6 (b)). Although being assigned to some sort of excimeric state[77], the origin of the Y-state has never been satisfactorily clarified and even a monomeric origin is not completely ruled out.[73] Another material system, where the excimer formation has been extensively studied, is PTCDA[6], a Perylene derivative. Here, a detailed analysis, where step-by-step the PTCDA coverage on a mica subtsrate is increased, impressively showed the transition from the monomer to the excimer photoluminescence (Fig. 5.6 (c)).[74]

---

[6] Perylene-3,4,9,10-tetracarboxylic dianhydride

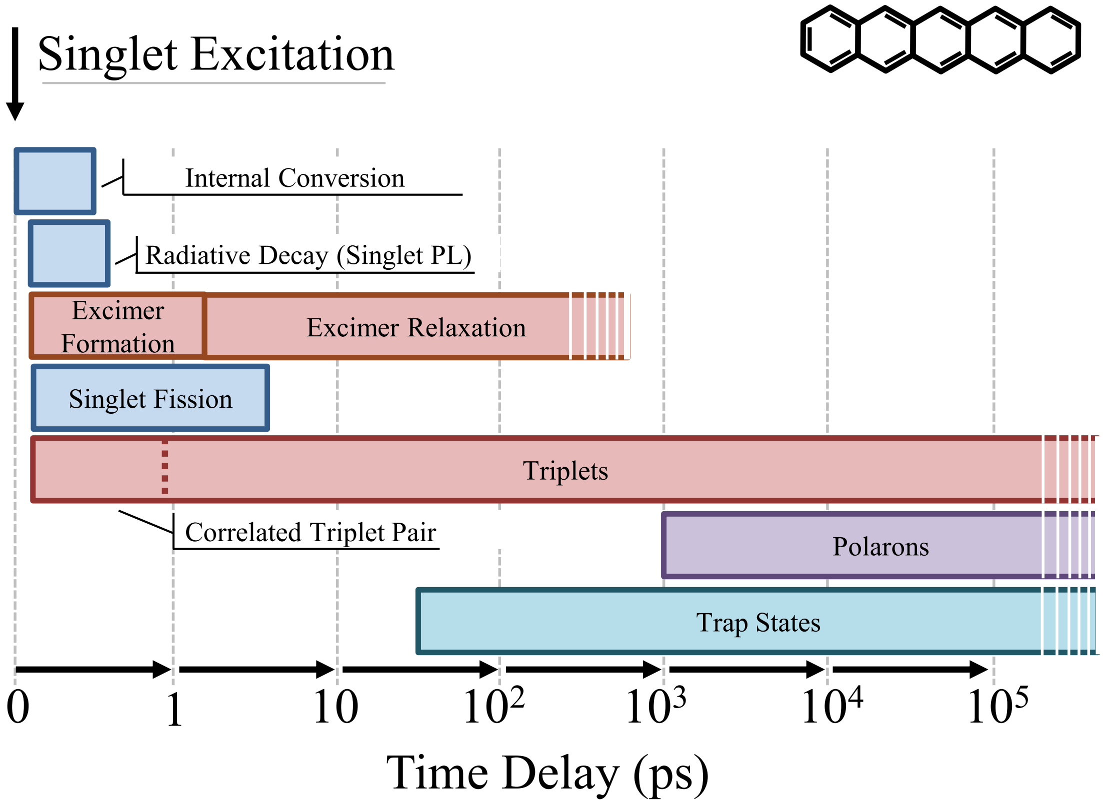

Abbildung 5.7: Decay mechanisms of PEN crystals. Singlet fission converts the majority of neutral carriers from the singlet to the triplet system. Free carrier creation (Polaron creation) occurs at an electron-acceptor interface, e.g., C_{60}.

5.1.2 Singlet Exciton Fission

Singlet fission is considered as a competing relaxation channel to excimer formation and consequently occurs right after optical excitation. It involves the conversion of one singlet exciton into two triplet excitons (Fig. 5.8). Due to the apparent carrier multiplication, singlet fission is regarded as a process with the potential to increase light conversion efficiencies of solar cells significantly.

In general, an electronic excitation induced by an absorbed photon in a molecule results in an excited singlet state. However, this is not necessarily the lowest electronic excitation. In polyacenes the excited triplet states are considerably lower in energy (see

Ch. 2, Sec. 2.2.2, p.12), e.g., in PEN the first excited triplet state T_1 is estimated to be at 0.85 ± 0.03 eV in comparison to S_1 at 1.8 ± 0.1 eV.[78, 60, 79, 61] Although, as stated before, the energetic position of T_1 in a solid is still under debate (Ch. 2, Sec. 2.2.2, p.12), it is accepted that in polyacenes the T_1 state lies below the S_1.

Due to the singlet ground state in combination with dipole selection rules, typically the optical transitions in polyacenes are singlet excitations. So after optical excitation the exciton is in the singlet state, where subsequently it experiences various relaxation and possibly scattering processes in order to return to its ground state. In Sec. 2.2.2 it has been stated that the inter-system crossing from pure singlet to pure triplet systems is forbidden and for organic systems composed of elements with low atomic numbers in a first approximation this holds true. Still, normally the inter-system crossing rate is finite but small compared to other relaxation processes, e.g., solid Naphtalene: inter-system-crossing rate $1.6 \cdot 10^6\,\mathrm{s}^{-1}$; luminescence-decay rate $1.2 \cdot 10^7\,\mathrm{s}^{-1}$.[80, 81] Anyhow, as a consequence, in Naphtalene crystals the quantum efficiency at the $S_1 \rightarrow S_0$ transition is just 0.1 ± 0.02, in contrast to Anthracene crystals, where quantum efficiencies of even 0.80 ± 0.05 have been observed.[82, 83]

On the other hand, in Tetracene crystals only weak photoluminescence was detected with an estimated quantum efficiency of merely 0.05 ± 0.005.[11] Despite the fact, that the determined quantum efficiencies should be treated with caution and their comparability is not fully given (In the introduction of Ref. [83] it says: „Literaturwerte (für die Quantenausbeute von Naphtalin) sind wenig einheitlich: Die Messwerte bei Raumtemperatur (293 K) liegen zwischen 0.7 und 0.18,...“[7].), the order of magnitude lower photoluminescence is an indicator for efficient inter-system crossing. Strikingly, the evaluated quantum efficiency of Tetracene in solution is 0.21 at the singlet transition, suggesting a relaxation process in the crystal involving more than one molecule.[84][8] Temperature dependent photoluminescence measurements on Tetracene crystals later revealed an increase of the emission with decreasing temperature by a factor of 100.[86] Shortly afterwards, this increase was interpreted as a quench of the singlet fission pro-

---

[7] engl. (loose translation): The quantum efficiency of Naphtalene results in literature show large discrepancies: the measured values at room temperature vary between 0.18 and 0.7 at room temperature.

[8] This value has been taken from Ref. [85]. Ref. [84] was not accessible.

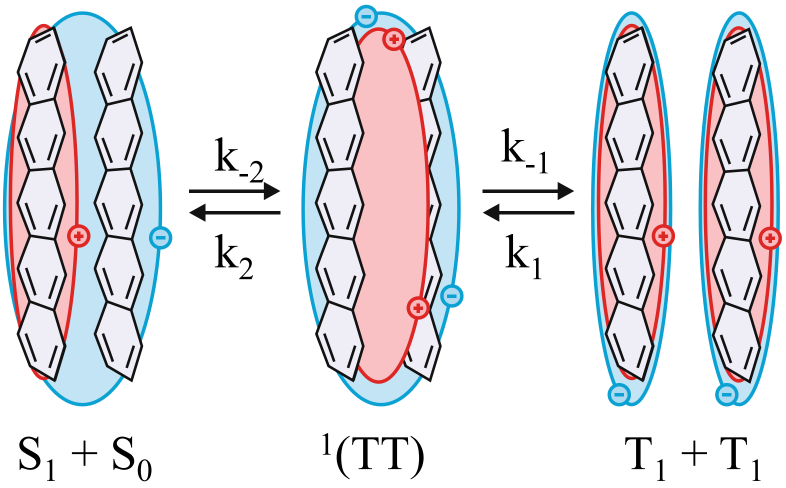

Abbildung 5.8: Schematic representation of the singlet exciton fission process. The singlet exciton exhibits partial charge transfer contributions. Adapted from Ref. [87].

cess, which is suggested to be the major decay mechanism of the singlet population at room temperature.[10] This hypothesis was verified by measuring the photoluminescence in an externally applied magnetic field.[85] In that experiment, it was shown, that the emission efficiency increased with increasing magnetic field strength and changed with changing field orientation in respect to the crystal planes.

The basic idea of the underlying mechanisms responsible for singlet fission hasn't changed much, since it's postulation in the 60ies. Singlet fission is regarded as the reverse process of triplet annihilation, which in turn is responsible for delayed fluorescence. It involves at least two monomers; the excited singlet exciton relaxes to the lower lying triplet state, while simultaneously exciting a second triplet exciton in the adjacent molecule (see Fig. 5.8). Apparently, the singlet energy needs to be at least twice the triplet energy so that singlet fission happens exothermic:

$$0 \leq \mathrm{E}(\mathrm{S}_1) - 2 \times \mathrm{E}(\mathrm{T}_1). \tag{5.17}$$

This requirement is not fulfilled in Naphtalene (≈ -1.3 eV) and Anthracene (≈ -0.55 eV) and not even in Tetracene (≈ -0.21 eV), where singlet fission was initially proposed.[88]

However, PEN, the next polyacene in the list, fulfills the requirement ($\approx 0.1\,\text{eV}$) and serves supposedly as an ideal model system to study this process. The simplified kinetic scheme of the conversion is traditionally written as follows:[9]

$$S_0 + S_1 \underset{k_2}{\overset{k_{-2}}{\rightleftharpoons}} {}^1(TT) \underset{k_1}{\overset{k_{-1}}{\rightleftharpoons}} T_1 + T_1 \tag{5.18}$$

This scheme includes the conversion of the singlet exciton S_1 to the so called „correlated triplet pair“ ${}^1(TT)$ and the following dissociation into two separate triplet excitons. Therein, the three steps are characterized by the rates $k_{-2;2;1;-1}$, treating back and forth conversions. Furthermore, a branching ratio can be defined:

$$\epsilon = \frac{k_2}{k_{-1}}, \tag{5.19}$$

indicating the conversion efficiency of the singlet fission process.

The spin multiplicity in the correlated triplet pair is denoted as a singlet state, due to the simple picture of two triplet states, whose spin functions couple into a pure singlet. A more appropriate description of this singlet state is the coherent superposition of all possible nine triplet sublevels created by two triplet excitons, which themselves are no longer pure spin eigenstates.[9] Correspondingly, ${}^1(TT)$ is also referred to as a multi-exciton state.[89] The transition step between both singlet states in Eq. 5.18 should not be regarded as an incoherent scattering channel. Since both states can be observed simultaneously in 2PPE experiments right after optical excitation, they are necessarily coupled coherently (see Fig. 5.9).[89] Within this transition state, only the electrostatic Hamiltonian ($\mathscr{H}_{el}$) is allowed to act. In the second step, the spin Hamiltonian ($\mathscr{H}_{spin}$) introduces decoherence and exciton diffusion in order to create two separate triplet pairs.[9] Thus, the interaction Hamiltonian is divided into two parts:

$$\mathscr{H} = \mathscr{H}_{el} + \mathscr{H}_{spin}. \tag{5.20}$$

It is obvious, that a separated treatment of the electrostatic and spin interactions cannot reflect the complete nature of the dynamics, however, to some extent they are able to identify pathways for this process.

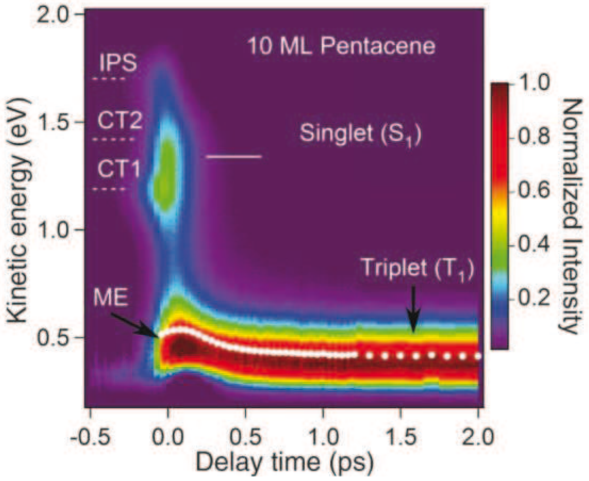

Abbildung 5.9: 2PPE measurement of 10 monolayers PEN. The excitation energy of the pump pulse was tuned to 2.15 eV and the ionization energy of the probe pulse to 4.65 eV. Singlet (S_1) and correlated Triplet (^1TT) signals occur at the same time. Adapted from Ref. [89].

Typically the rate constant k_{-2} is treated in terms of an Arrhenius equation:[9]

$$k_{-2} = A[S_1S_0 \rightarrow {}^1(TT)]e^{-\frac{\Delta E}{k_B T}}, \tag{5.21}$$

with the frequency factor $A[S_1S_0 \rightarrow {}^1(TT)]$ for the conversion of a singlet exciton into a triplet pair, the activation energy ΔE and the Boltzmann constant k_B. The determination of $A[S_1S_0 \rightarrow {}^1(TT)]$ for a simple dimer model will be given below. The activation energy ΔE for exoergic singlet fission is zero, unlike for endoergic singlet fission, where it is at least equal to the energy difference between S_1S_0 and $^1(TT)$. In fact, the magnitude of ΔE is strongly dependent on possible intra- or inter-molecular structural changes, which might be necessary for singlet fission to occur. Therefore, a general assumption for all systems experiencing singlet fission is impossible. As far as Eq. 5.17 is concerned, typically, the energies of states $^1(TT)$ and $T_1 + T_1$ are assumed to be equal; a reasonable assumption for weakly interacting molecules and questionable for strong interactions.[9]

The starting point of a simple theoretical treatment is again a system of two weakly interacting molecules. The electrostatic Hamiltonian ($\mathscr{H}_{el}$) of the total system is then again approximated as the sum of the individual molecular Hamiltonians ($\mathscr{H}_{el;A,B}$) and the interaction Hamiltonian ($\mathscr{H}_{int}$). The participating orbitals in the process are reduced to the HOMO ($H_{A,B}$) and the LUMO ($L_{A,B}$) of the monomers, similar to the treatment of the excimer, yet, without the consideration of the core-levels. Hence, the essential states for the description of singlet fission are given as follows:

$$\left|S_1^A S_0^B\right\rangle = |A^* B\rangle \approx \left|H_B^{\uparrow} H_B^{\downarrow} \left\{H_A^{\uparrow} L_A^{\downarrow} + H_A^{\downarrow} L_A^{\uparrow}\right\}\right\rangle , \tag{5.22}$$

$$\left|{}^1A^A C^B\right\rangle = \left|A^- B^+\right\rangle \approx \left|H_A^{\uparrow} H_A^{\downarrow} \left\{H_B^{\uparrow} L_A^{\downarrow} + H_B^{\downarrow} L_A^{\uparrow}\right\}\right\rangle , \tag{5.23}$$

$$\begin{aligned}\left|{}^1(TT)\right\rangle = |A^* B^*\rangle \approx & \left|\left\{\left(H_A^{\uparrow} L_A^{\uparrow}\right) + \left(H_A^{\downarrow} L_A^{\downarrow}\right) + \left[\left(H_A^{\uparrow} L_A^{\downarrow}\right) + \left(H_A^{\downarrow} L_A^{\uparrow}\right)\right]\right\}\right\rangle \\ & \times \left|\left\{\left(H_B^{\uparrow} L_B^{\uparrow}\right) + \left(H_B^{\downarrow} L_B^{\downarrow}\right) + \left[\left(H_B^{\uparrow} L_B^{\downarrow}\right) + \left(H_B^{\downarrow} L_B^{\uparrow}\right)\right]\right\}\right\rangle .\end{aligned} \tag{5.24}$$

The eigenenergies relative to the ground state, including interaction corrections of $\mathscr{H}_{int}$[9], are denoted as $E(S_1S_0)$, $E(^1(TT))$ and $E(^1CA)$, respectively. The resulting truncated Hamiltonian matrix of the system is:[9]

$$\mathscr{H}_{el} =$$

$$\begin{pmatrix}
\mathbf{E(^1CA)} & \langle ^1CA|\mathscr{H}_{el}|S_1S_0\rangle & \langle ^1CA|\mathscr{H}_{el}|^1(TT)\rangle & \langle ^1CA|\mathscr{H}_{el}|S_0S_1\rangle & \langle ^1CA|\mathscr{H}_{el}|^1AC\rangle & \langle ^1CA|\mathscr{H}_{el}|S_0S_0\rangle \\
\langle S_1S_0|\mathscr{H}_{el}|^1CA\rangle & \mathbf{E(S_1S_0)} & \langle S_1S_0|\mathscr{H}_{el}|^1(TT)\rangle & \langle S_1S_0|\mathscr{H}_{el}|S_0S_1\rangle & \langle S_1S_0|\mathscr{H}_{el}|^1AC\rangle & \langle S_1S_0|\mathscr{H}_{el}|S_0S_0\rangle \\
\langle ^1(TT)|\mathscr{H}_{el}|^1CA\rangle & \langle ^1(TT)|\mathscr{H}_{el}|S_1S_0\rangle & \mathbf{E(^1(TT))} & \langle ^1(TT)|\mathscr{H}_{el}|S_0S_1\rangle & \langle ^1(TT)|\mathscr{H}_{el}|^1AC\rangle & \langle ^1(TT)|\mathscr{H}_{el}|S_0S_0\rangle \\
\langle S_0S_1|\mathscr{H}_{el}|^1CA\rangle & \langle S_0S_1|\mathscr{H}_{el}|S_1S_0\rangle & \langle S_0S_1|\mathscr{H}_{el}|^1(TT)\rangle & \mathbf{E(S_0S_1)} & \langle S_0S_1|\mathscr{H}_{el}|^1AC\rangle & \langle S_0S_1|\mathscr{H}_{el}|S_0S_0\rangle \\
\langle ^1AC|\mathscr{H}_{el}|^1CA\rangle & \langle ^1AC|\mathscr{H}_{el}|S_1S_0\rangle & \langle ^1AC|\mathscr{H}_{el}|^1(TT)\rangle & \langle ^1AC|\mathscr{H}_{el}|S_0S_1\rangle & \mathbf{E(^1AC)} & \langle ^1AC|\mathscr{H}_{el}|S_0S_0\rangle \\
\langle S_0S_0|\mathscr{H}_{el}|^1CA\rangle & \langle S_0S_0|\mathscr{H}_{el}|S_1S_0\rangle & \langle S_0S_0|\mathscr{H}_{el}|^1(TT)\rangle & \langle S_0S_0|\mathscr{H}_{el}|S_0S_1\rangle & \langle S_0S_0|\mathscr{H}_{el}|^1AC\rangle & \mathbf{0}
\end{pmatrix}$$

The individual matrix elements can be found in more detail in Ref. [9]. The off-diagonal elements describe the coupling between the singlet states. In the case of localized states and small interaction, the time development of the system can be described by first-order perturbation theory. Accordingly, the transition rate of the initially populated state $S_1 + S_0$ to the quasi-continuum of vibrational states of $^1(TT)$ can be determined

---

[9] Corrections are given by the diagonal elements of $\mathscr{H}_{int}$

by applying Fermi's golden rule:[9]

$$A\left[S_1S_0 \to {}^1(TT)\right] = \left(\frac{2\pi}{\hbar}\right) \left|\langle {}^1(TT)|\mathscr{H}_{el}\,|S_1S_0\rangle\right|^2 \rho\left\{E({}^1(TT))\right\}, \tag{5.25}$$

where ρ is the Franck-Condon weighted density of states at the energy $E({}^1(TT))$. This would be the route for the direct singlet fission process, with the responsible matrix elements marked in red. It has been shown that these transition rates are very sensitive to the orientation of the two molecules. Actually, perfectly stacked molecules are not necessarily the most efficient configuration for the direct transition, on the contrary, they have vanishing matrix elements. For Isobenzofuran, for instance, a slightly parallel shifted stacking order seems to be the optimal case.[9]

The indirect pathway is marked in blue and cyan; a localized Frenkel exciton couples to the charge transfer state (cyan matrix elements), which consecutively couples to the triplet pair state (blue matrix elements). As a result second order perturbation theory has to be applied in order to deal with this two step singlet fission mechanism:

$$\begin{aligned} A\left[S_1S_0 \to {}^1CA \to {}^1(TT)\right] = \left(\frac{2\pi}{\hbar}\right) |\langle {}^1(TT)|\mathscr{H}_{el}\,|S_1S_0\rangle \\ - \frac{\langle {}^1(TT)|\mathscr{H}_{el}|\,{}^1CA\rangle\langle {}^1CA + {}^1AC)|\mathscr{H}_{el}|\,S_1S_0\rangle}{\Delta E_{CT}}|^2\rho\left\{E({}^1(TT))\right\}, \end{aligned} \tag{5.26}$$

where ΔE_{CT} is the difference between the energy of the CT states and the energy of the S_1S_0 and ${}^1(TT)$ states.[90] For slip-stacked ethylene molecules it has been shown that Eq. 5.26 is dominated by the indirect terms. So, neglecting the direct term and additionally applying the zero differential overlap approximation[10] in combination with an expansion of the molecular to atomic orbitals, within the tight-binding approximation, Eq. 5.26 is simplified and can now be used as a quick tool to estimate the singlet fission rate for various molecules and packing motifs.[90] Figure 5.10 shows the simplified singlet fission rate equation, where the sums are performed over pairs of interacting neighboring atomic orbitals ($\mu\nu$) with their corresponding amplitudes $c_{\mu_{l;h};\nu_{l;h}}$[11] and their resonance integrals $\beta_{\mu\nu}$.

---

[10] Here, completely neglecting two-electron repulsion integrals.

[11] l: LUMO; h: HOMO

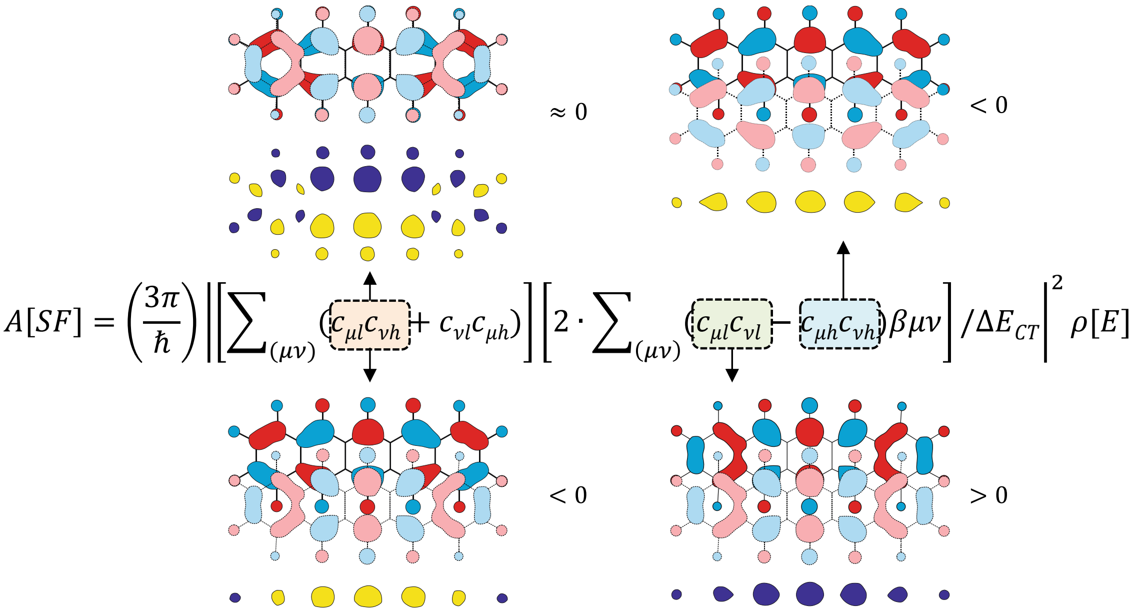

$$A[SF] = \left(\frac{3\pi}{\hbar}\right)\left|\left[\sum_{(\mu\nu)}\left(\boxed{c_{\mu l}c_{\nu h}} + c_{\nu l}c_{\mu h}\right)\right]\left[2\cdot\sum_{(\mu\nu)}\left(\boxed{c_{\mu l}c_{\nu l}} - \boxed{c_{\mu h}c_{\nu h}}\right)\beta\mu\nu\right]/\Delta E_{CT}\right|^{2}\rho[E]$$

Abbildung 5.10: Simplified singlet exciton fission rate calculation for the indirect path. Graphical results of the amplitude products for the HOMO and LUMO (taken from Ref. [42]) of PFP are shown. Purple spaces indicate positive results, while yellow spaces indicate negative results.

Additionally, in Fig. 5.10 a quick analysis is performed for a pair of PFP molecules. However, instead of atomic orbitals DFT calculated molecular orbitals from Ref. [42] are used, slightly increasing accuracy. Two situations are considered: eclipse stacking, where the molecular orbitals of the π-system overlap perfectly and still maintain an inversion symmetry, and slipped stacking, where the molecules experience a slip along their short axis and the inversion symmetry of the pair is broken. The graphical results of the convolution of the wavefunctions' amplitudes are given as purple (positive sign) and yellow (negative signs) spaces below the orbitals of the DFT calculation. Each space represents the performed product marked in the singlet fission rate equation. Considering the eclipse stacking, we see that the analysis results in equal amounts of positive and negative amplitudes which cancel after summation. Consequently, the left-hand side of the product is zero, turning the whole expression to zero and leading to a vanishing singlet fission rate.

In the slip-stacked arrangement the first term is dominated by negative amplitudes, so that summation yields an overall negative result, in contrast to the eclipse-stacking. In the second term in Fig. 5.10, the first product in the summation yields an overall positive amplitude, while the second turns out to be negative. However, since the second product is subtracted from the first, it further increases the rate, making the slip stacking an ideal packing motif for singlet fission.

Now, if the singlet excitation, i.e. $\left|S_1^A S_0^B\right\rangle$; $\left|{}^1A^A C^B\right\rangle$ and their counterparts are delocalized over both molecules, e.g. in PEN or PFP, then the superposition of these states have to be considered:

$$\left|S_1^A S_0^B\right\rangle \pm \left|S_0^A S_1^B\right\rangle \tag{5.27}$$

$$\left|{}^1A^A C^B\right\rangle \pm \left|{}^1C^A A^B\right\rangle \tag{5.28}$$

Furthermore, these states mix significantly, if they are close in energy, resulting in non-vanishing cyan matrix elements.[9] As a consequence, the strict distinction between a direct and an indirect path in singlet fission can no longer be made.

Having established the way, how a singlet excitation can couple to the correlated triplet pair, the essential second step in Eq. 5.18, for a complete singlet fission process, is the decoupling of the triplet pair into two uncorrelated triplet excitons and eventually, their diffusion onto different crystal sites. In order to speak of two independent triplet excitons, the correlated triplet pair needs to lose its phase relation, i.e., they need to dephase. As said before, the ${}^1(TT)$ state is composed of nine sublevels, which are all eigenfunctions of the total system Hamiltonian $\mathscr{H}_{el} + \mathscr{H}_{spin}$ (illustrated in Fig. 5.11). In more detail, these sublevels are usually mixtures of singlet ${}^1(TT)$, triplet ${}^3(TT)$ and quintet ${}^5(TT)$ eigenstates, e.g., for the kth function:

$$\Psi_k = \underbrace{\phi_S C_S^k \left|S\right\rangle}_{{}^1(TT)} + \underbrace{\phi_T \sum_{l=2}^{4} C_T^{k,l} \left|T^l\right\rangle}_{{}^3(TT)} + \underbrace{\phi_Q \sum_{l=5}^{9} C_Q^{k,l} \left|Q^l\right\rangle}_{{}^5(TT)}, \tag{5.29}$$

where $\phi_{S;T;Q}$ are the three spatial wavefunctions and $\left|S; T^L; Q^L\right\rangle$ are the spin wavefunctions. The amount of mixture present, depends on the off-diagonal elements of the spin Hamiltonian $\mathscr{H}_{spin}$ matrix in combination with the energy splitting of the three spin

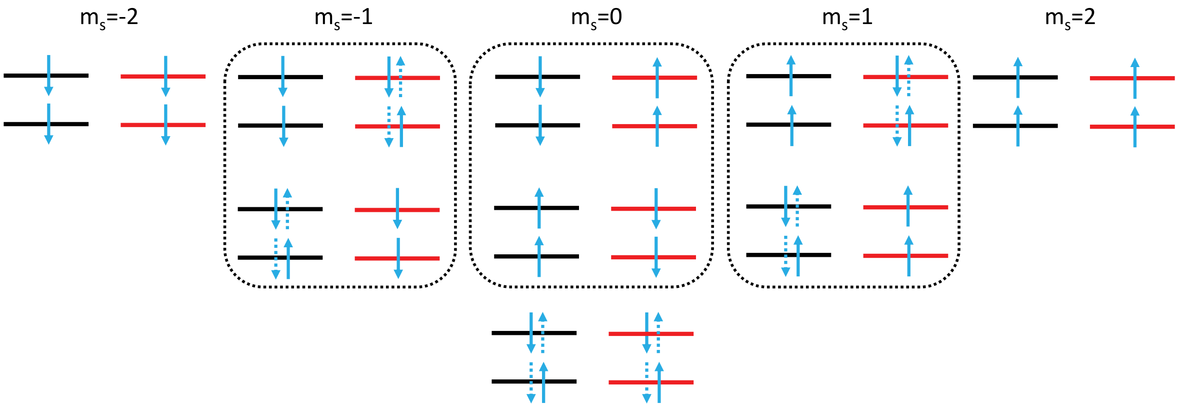

Abbildung 5.11: Simple representation of the nine sublevels resulting from the superposition of two triplet excitons in the correlated triplet pair. The excitons reside on translational non-equivalent lattice sites. In the case of symmetric lattice sites, the states marked in dotted boxes are indistinguishable, eventually resulting in six sublevels.

states $E(^1(TT);^3(TT);^5(TT))$. The higher the amount of mixture, the higher the probability of the correlated excitons to lose their phase relation and, consequently, to act as independent triplet excitons. The energy splitting of the spin states is predominantly determined by $\mathscr{H}_{el}$, since the spin-spin dipole interaction between electrons on adjacent molecules is generally considered small. However, the exact energy alignment cannot be estimated merely by looking at the crystalline structure, but has to be calculated explicitly. As again, potential admixture of charge transfer contributions can severely alter the eigenenergies of these states. Anyhow, the subsystem of the nine correlated triplet pair states in Eq. 5.29 is not degenerate.

Moreover, it is assumed, that the amount of $^1(TT)$ back-conversion into singlet excitons is governed by the number of $^1(TT)$ sublevels, carrying significant singlet wavefunction admixture. Accordingly, the back-conversion and, subsequently, the radiative decay increases with increasing amount of Ψ_k, where C_S^k is different from zero.[91] In the case of homofission[12] combined with symmetry equivalent chromophores, only three correlated triplet pair states carry singlet spin functions.[91] Consequently, only these three states take part at the singlet fission and fusion process. This selection rule is

---

[12] The participating chromophores in the fission process are of equal kind.

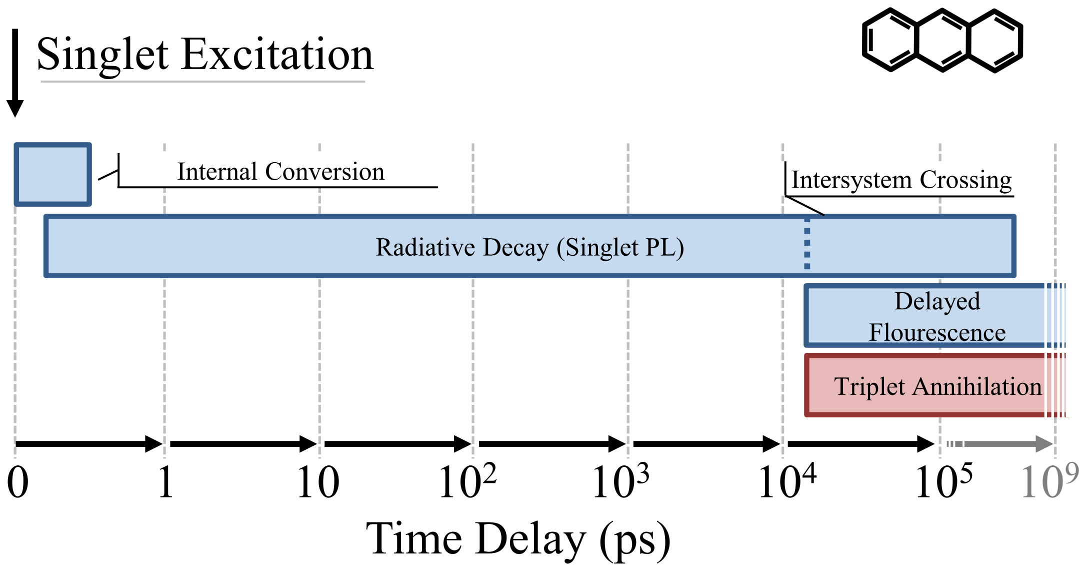

Abbildung 5.12: Decay mechanisms of the Anthracene crystal. Triplet annihilation leads to delayed fluoroscence.

lifted, as soon as either an external magnetic field is applied, or the correlated triplet pair is delocalized to some extent over chromophores with unequal symmetry.

5.1.3 Triplet Annihilation

In the 60ies, magnetic field dependent measurements of the luminescence of Anthracene and Tetracene eventually lead to the formulation of the singlet fission and triplet fusion processes. Triplet annihilation or fusion is the reverse process of singlet fission. Two triplet excitons hop to adjacent chromophores and scatter into a correlated triplet pair state. The conversion into a singlet exciton is then governed by the amount of sublevels with singlet spin function contributions. Respectively, the annihilation is observed as delayed photoluminescence out of the singlet state. This is observed, for instance, in Anthracene single crystals after directly exciting carriers into the triplet state (Fig. 5.13 (a)).[92]
In the case of an external magnetic field, when the Zeeman splitting exceeds the zero field splitting, the spin states are quantized along the magnetic field.[91] In the simplest

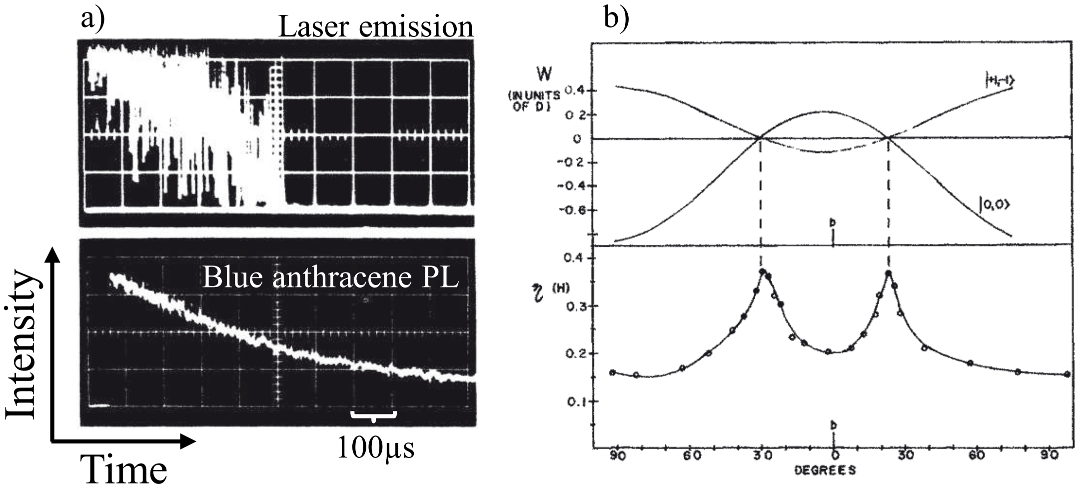

Abbildung 5.13: (a) Delayed singlet fluorescence (3.42 eV) from an Anthracene single crystal after laser excitation into the triplet state (1.79 eV). Adapted from Ref. [92]. (b) Top: Energy calculation of correlated triplet pair states with partial singlet spin function. Bottom: Singlet fluorescence efficiency $\eta(H)$ as a function of orientation of the magnetic field vector. Adapted from Ref. [85].

case, the correlated triplet again has three states with singlet contributions. However, two of them are degenerate and since some weak spin-spin coupling needs to be present for the annihilation process, their symmetric and antisymmetric combinations are the eigenstates of the system. One of the two new eigenstates is spatially purely antisymmetric, hence, a pure triplet state. This reduces the amount of eigenstates with singlet character. Consequently, the effective triplet annihilation rate is reduced with increasing magnetic field strength.[93] It is observed as reduced delayed fluorescence in Anthracene or as reduced singlet fission in Tetracene, shown in Fig. 5.13 (b).[85] Changing the magnetic field vector changes the eigenenergies of the two partially singlet states. At the point, where they are degenerate the fission/fusion rate is at its minimum which is observed as peaks in the singlet fluorescence efficiency as a function of the magnetic field vector (Fig. 5.13 (b)). In general, the triplet annihilation does not necessarily end up in singlet excitons, but also in hot triplet excitons or quintet excitons, although the latter is typically considered energetically unfavorable and, therefore, negligible. The rate of the triplet channel, i.e., the channel where the correlated triplet pair fuses into a hot triplet exciton, is independent of the magnetic field, as, in a first approximation, these purely antisymmetric wavefunctions do not mix with the singlet or quintet wavefunctions.[94] On the other hand, this leads to a purely triplet fusion channel, which also acts as a non-radiative relaxation channel. In principle, the conversion of a hot triplet exciton into a singlet exciton is possible, however, in many polyacenes this rate is six orders of magnitude lower than the internal conversion within the triplet system.[95] Consequently, the energy of one triplet exciton is dissipated as heat to the lattice.

5.1.4 Polarons

Until now, only neutral excitations were treated. However, in order to get a photocurrent, charge separation of electron and hole, i.e., exciton ionization has to take place. Since the results presented in this thesis are all based on neutral excitations, just a rough description is given for the sake of completeness.

In organic heterojunctions, e.g., PEN/C_{60}, charge separation occurs at the donor-acceptor interfaces. Due to the large exciton binding energies in organic crystals, the acceptor levels typically have to overcome several hundreds of meV. After separation, the carriers act as single quasi-particles in the crystal lattice. As they are no longer neutral, they induce attractive (repulsive) forces towards surrounding molecules which lead to a local distortion of the crystal lattice. The distortion can be considered as a phonon cloud composed of a superposition of longitudinal optical phonons surrounding the charge carrier.[17] This entity is called a polaron with its own excitation spectrum. The formation time of polarons is directly coupled to the diffusion of the excited excitons which first have to reach an appropriate interface. In PEN/C_{60} this happened after a few $\approx 2.5\,\mathrm{ns}$.[96]

Charge separation not only occurs on interfaces, but can also occur at lattice defects or at surface states.

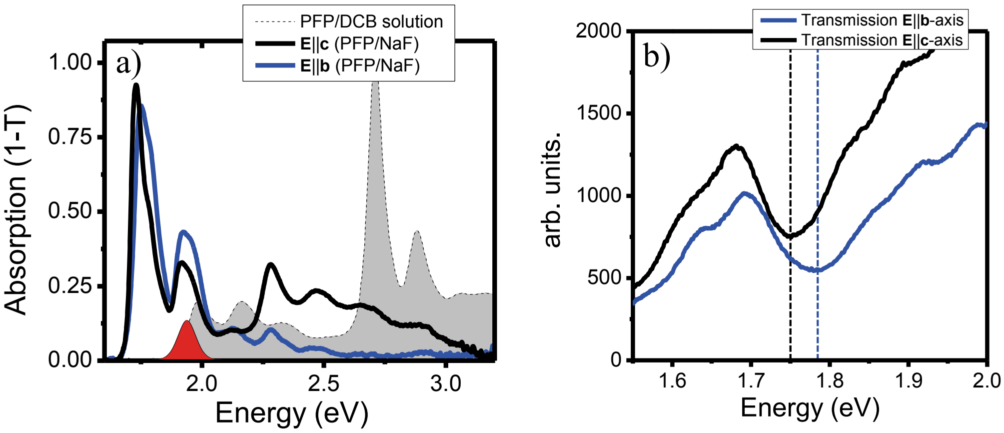

Abbildung 5.14: (a) Excitation energy of the pump pulse with the linear absorption of the sample. The excitation corresponds to the HOMO-LUMO transition of PFP in Dichlorbenzene solution. (b) Alignment of the probe polarization to a crystalline axes controlled by the transmission of the sample. The lowest resonance shifts in energy when changing from the $\vec{c}$- to the $\vec{b}$-axis.

5.2 Polarization-Resolved Nonlinear Absorption of Perfluoropentacene

In this section the ultrafast carrier dynamics of PFP after optical excitation are analyzed with polarization resolved pump-probe spectroscopy. The experiments are performed on the same single crystalline samples as in Ch. 4 allowing for the correlation of carrier dynamics and crystalline directions. It shows that the dynamics are highly anisotropic, thus, strongly correlated to the packing nature of the molecules along the different crystalline axes. In the slipped stack direction of the crystal, i.e., the $\vec{b}$-axis, the excited excitons are significantly delocalized corroborating the strong coupling between molecules along this direction, as suggested in the previous Ch. 4. Furthermore, excimer as well as triplet pair formation along the b-axis are identified and their decay mechanisms are described using a rate-equation model. The samples are provided by T. Breuer and G. Witte from the Philipps-University Marburg.

5.2.1 Experimental Details

The analyzed sample #0058 is a PFP thin film epitaxially grown on NaF(100) with a nominal film thickness of 150 nm. Here, a standing conformation of the molecules is found, where the $\vec{b}$- and $\vec{c}$-axis of the crystal are optically addressable in transmission geometry. The sample #0051 is a PFP thin film epitaxially grown on KCl(100) with the same nominal film thickness of 150 nm. However, the molecules are found in lying conformation, thus, the crystalline $\vec{a}$- and $\vec{b}$-axis are optically addressable in transmission geometry.

The non-linear absorption experiments are performed with the pump-probe setup described in Ch. 3. The excitation energy of the pump pulse is set to 1.95 eV (see Fig. 5.14 (a)), if not stated otherwise. It corresponds to the HOMO-LUMO transition of PFP soluted in Dichlorbenzene.[43]

The pump and probe polarizations are adjusted with half-wave plates before the sample. Before the experiment, the probe pulse polarization is aligned to a crystalline axis with the help of the sample's transmission spectrum. Here, the previously discussed Davydov-splitting, i.e., the energy shift of the lowest resonance clearly identifies the crystalline axis (see Fig. 5.14 (b)). Accordingly, the maximum blue shift in the transmission spectrum identifies the $\vec{b}$-axis' of the crystal. Moreover, the transmission spectrum is used to find single crystalline domains by comparing amount of shift, which is maximized in a single crystalline domain, as well as linewidth of the fundamental transition for several sample positions.

The orientation of the probe pulse polarization allows for the correlation of structural properties and electronic excitation. Its polarization is thus set parallel either to the $\vec{b}$- or the $\vec{c}$-axis for the samples grown on NaF and along the $\vec{a}$- or the $\vec{b}$-axis for the samples grown on KCl.

5.2.2 Non-linear absorption of PFP: the c- and b-axis

We start with the sample PFP/Naf(100) where the $\vec{c}$- and $\vec{b}$-axis are optically addressable by transmission spectroscopy in normal incidence. The differential absorpti-

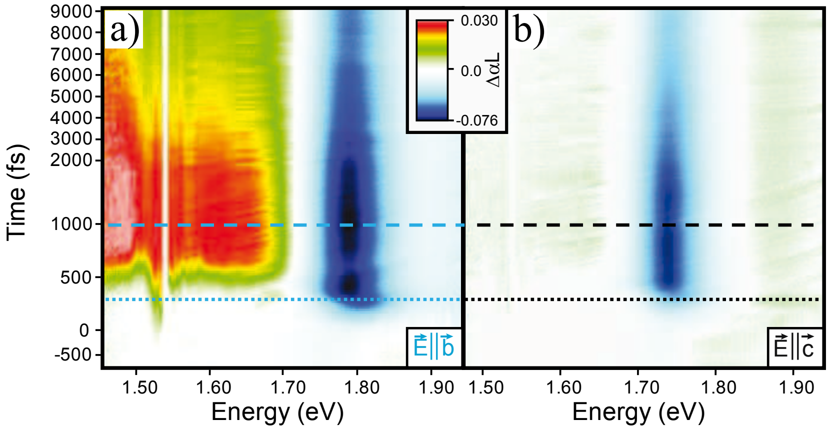

Abbildung 5.15: (a) 2D false-color plot of the differential absorption (ΔαL) along the $\vec{b}$-axis. (b) 2D false-color plot of the ΔαL along the $\vec{c}$-axis.

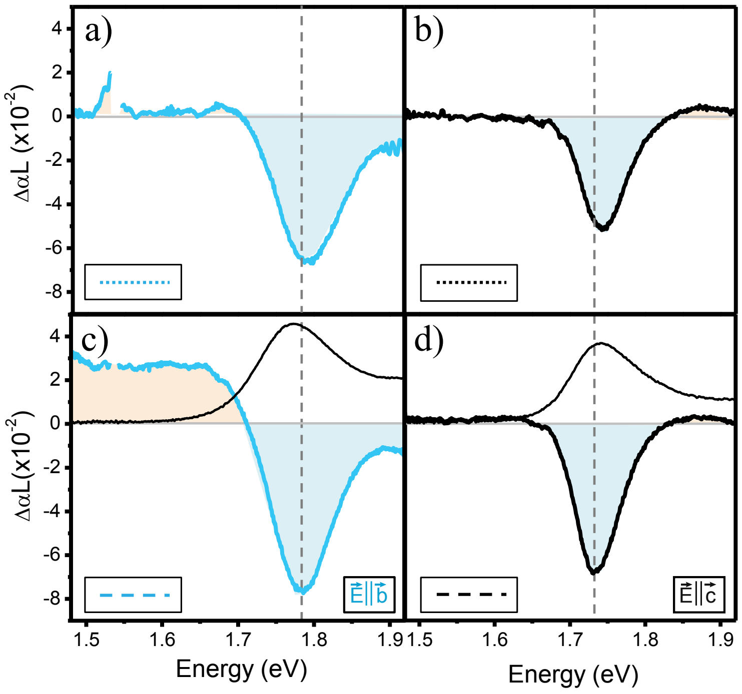

Abbildung 5.16: (a) ΔαL spectrum of the $\vec{b}$-axis after 300 fs. (b) ΔαL spectrum of the $\vec{c}$-axis after 300 fs. (c) ΔαL spectrum of the $\vec{b}$-axis after 1 ps. Solid black line: linear absorption of the $\vec{b}$-axis for reference. (d) ΔαL spectrum of the $\vec{c}$-axis after 1 ps. Solid black line: linear absorption of the $\vec{c}$-axis for reference.

on ($\Delta\alpha$L) is shown as a function of energy and time-delay in a 2D false-color plot in Figs. 5.15 (a,b) along both crystal axes. Clearly, we observe significant differences in the non-linear response. The most pronounced anisotropy is the strong broadband induced absorption parallel to the $\vec{b}$-axis below the fundamental transition. This feature is absent along the $\vec{c}$-axis; cf. Figs. 5.16 (c,d), where the $\Delta\alpha$L-spectra 1ps after excitation along the $\vec{b}$- and $\vec{c}$-axis are given.

The induced absorption is a consequence of emerging new absorption channels, due to excited carriers. Evidently, the dipole moment of the new absorption channels is oriented along the $\vec{b}$-axis. Furthermore, the induced absorption is a clear crystalline signature, since the two molecules in the unit cell exhibit a nearly rectangular conformation, and accordingly, should show practically a degenerate response, if they acted as isolated monomers. As this is not the case, the excitations have to be virtually exclusively delocalized along the $\vec{b}$-axis.

As mentioned before, along the $\vec{b}$-axis the molecules are stacked parallel face-to-face in slightly slipped fashion. This slipped stacking already lead to the observed H-aggregate in linear absorption in Ch. 4. Thus, the molecular coupling is not only responsible for constructive interference of the transition dipoles, but also for the delocalization of the excited singlet excitons.

In Figs. 5.16 (a,b) the $\Delta\alpha$L-spectra are shown for a time-delay of 300 fs. At this time delay the bleaching, i.e., negative $\Delta\alpha$L-signal, is already present, whereas the broadband induced absorption is not. In general, bleaching of the fundamental transition indicates, that some of the original, optically allowed transitions are blocked. This means, that either the state is already occupied by a fermion, i.e., Pauli-blocking, or that the probed system no longer resides in the ground state. Accordingly, after 300 fs excited carriers are present in the system. A closer look at the spectrum Fig. 5.16 (a) reveals, that the bleaching is accompanied by a narrow induced absorption resonance at 1.53 eV (FWHM≈12 meV). Hence, before the broadband induced absorption a discrete induced absorption is present. Similar to the broadband induced absorption, this feature is only observed along the $\vec{b}$-axis (cf. Figs. 5.16 (a,b)). Furthermore, we observe an energetic shift of the bleaching with delay time by comparing the spectra at τ_{Delay}=300 fs (Figs. 5.16 (a,b)) with the spectra at τ_{Delay}=1 ps (Figs. 5.16 (c,d)).

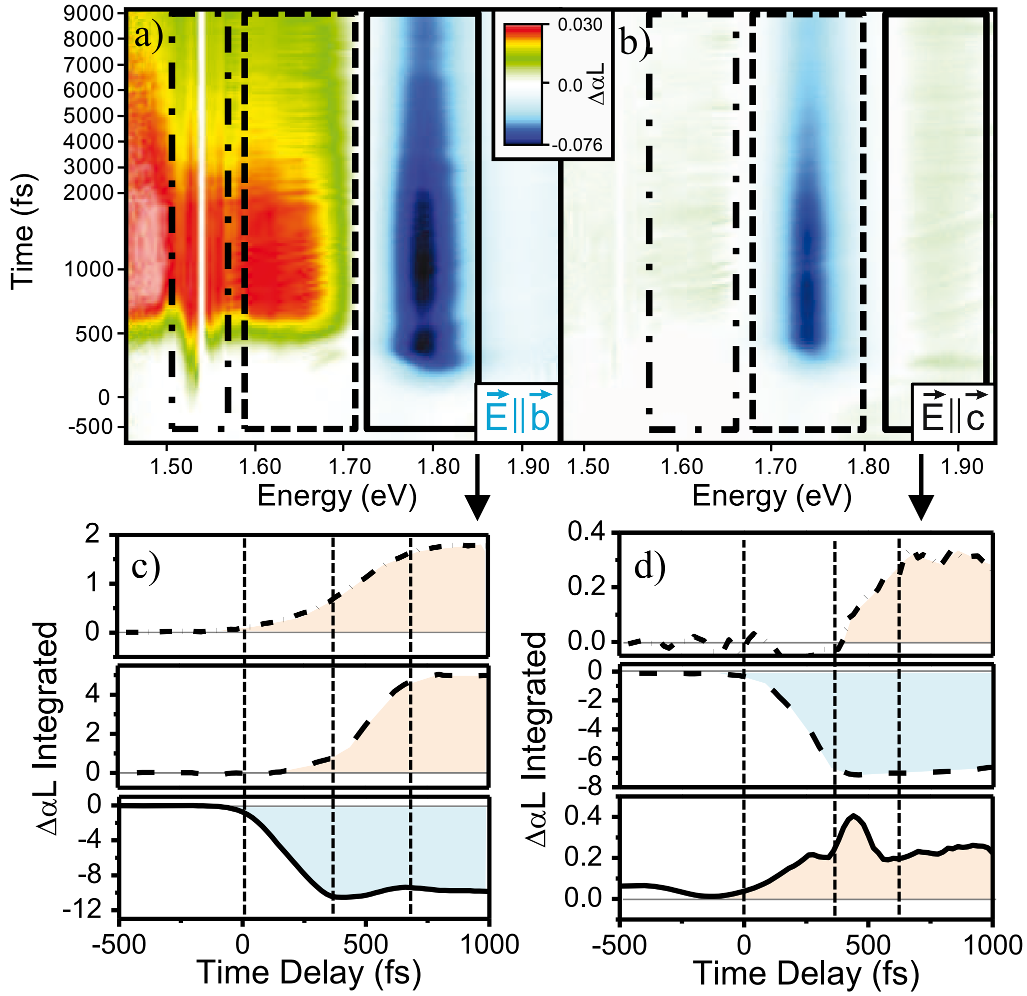

Abbildung 5.17: (a) 2D false-color plot of the ΔαL along the $\vec{b}$-axis. Transients are extracted from the marked regions, which are spectrally integrated. (b) 2D false-color plot of the ΔαL along the $\vec{c}$-axis. Transients are extracted from the marked regions, which are spectrally integrated. (c) Transients from the marked regions in (a). (d) Transients from the marked regions in (b).

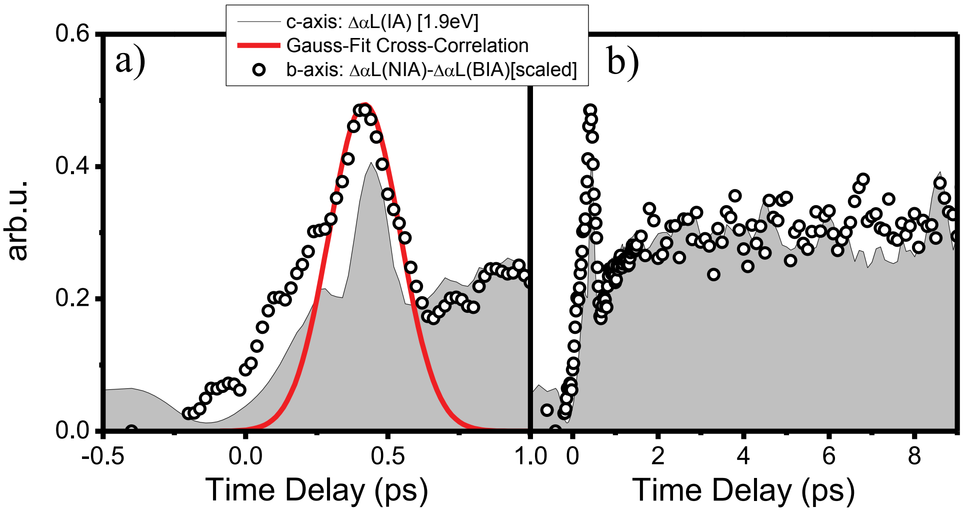

Abbildung 5.18: (a) Short term comparison of the induced absorption transient along the $\vec{c}$-axis at 1.9 eV with the evaluated transient of the narrowband induced absorption along the $\vec{b}$-axis at 1.54 eV. (b) same as (a) with long term evolution.

Transients from the prominent features are plotted in Figs. 5.17 (c,d), in order to determine their rise times. The transients are extracted by spectrally integrating the regions, which are marked by the boxes in Figs. 5.17 (a,b).

First, we focus on the $\vec{b}$-axis' transients shown in Fig. 5.17 (c). As already expected from the $\Delta\alpha$L-spectra, the onset of the broadband induced absorption is delayed by approximately 120 fs in respect to the bleaching and the discrete induced absorption. Interestingly, the broadband induced absorption starts, when the bleaching peaks. Subsequently, the bleaching experiences a dip after 650 fs, just 150 fs before the broadband induced absorption reaches its maximum. However, the bleaching nearly fully recovers afterwards. The discrete induced absorption at 1.53 eV starts with the bleaching, but it shows a longer rise time than both, the bleaching and the broadband induced absorption. This is a result of the overlaid broadband induced absorption signal, which extends the rise time artificially. In order to extract the real dynamics of the discrete induced absorption, the scaled broadband induced absorption transient is subtracted. The result is plotted as open circles in Fig. 5.18.

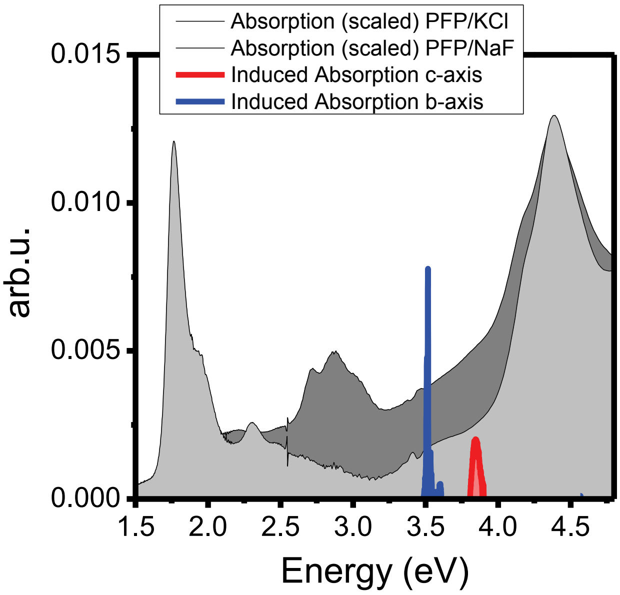

Abbildung 5.19: Comparison of PFP absorption spectra with the two-photon induced-absorption along the $\vec{b}$- and $\vec{c}$-axis.

The transients of the $\vec{c}$-axis are given in Fig. 5.17 (d). The bleaching shows the same rise time as the bleaching along the $\vec{b}$-axis. This is not surprising, since both have the same origin. Moreover, an induced absorption is observed around 1.6 eV. As its dynamics are similar to the broadband induced absorption along the $\vec{b}$-axis, it is assigned to residual $\vec{b}$-axis signal. At 1.9 eV an induced absorption is observed, which is absent along the $\vec{b}$-axis. Its transient has two time regimes: a short signal at a time delay of 450 fs with a FWHM comparable to the excitation pulse and a long term signal decaying on a picosecond time scale.

The short term $\vec{c}$-axis signal at 1.9 eV is compared to the extracted $\vec{b}$-axis discrete induced absorption signal at 1.53 eV along with the cross-correlation of the pump and probe pulse in Fig. 5.18. Apparently, all three signatures show the same temporal behavior. Since the cross correlation of pump and probe is extracted from two photon absorption in GaP, we come to the conclusion that both short induced absorption signatures originate from two photon absorption processes within PFP. Two photon absorptions allow for even parity transitions. Hence, the induced absorption shifted by the pump

Tabelle 5.1: Results of the double exponential fits of the transients in Fig. 5.21.

	A_1	τ_1	A_2	τ_2
$\vec{b}$-axis bleaching (1.7 eV-1.86 eV)	5±0.1	15 ps±1 ps	3.5±0.08	1 ns±0.5 ns
$\vec{b}$-axis induced absorption (1.45 eV-1.7 eV)	7.2±0.3	16.8 ps±1.2 ps	1.95±0.3	0.5 ns±0.37 ns
$\vec{c}$-axis bleaching (1.66 eV-1.83 eV)	5.6±0.1	14.5 ps±1 ps	2.3±0.1	0.6 ns±0.35 ns

energy does not correspond to any transition in the linear absorption of PFP, shown in Fig. 5.19. The excitation around 3.85 eV could be the dipole forbidden transition $S_0 \rightarrow S_6$, which was calculated by single molecular TD-DFT to be at 4 eV.[48] However, the transition at 3.5 eV does not fit to any of the listed transitions in Ref. [48]. The only close transition with 3.68 eV lies within the long axis of the molecule and, therefore, can be ruled out. Anyhow, both signatures show a polarization dependence, which is a hint for a crystalline response.

We now focus on the long term dynamics of the observed signals. An overview of the $\Delta\alpha$L-signal along both axes is given in Fig. 5.20. First, the essential three $\Delta\alpha$L-signals are analyzed, namely the bleaching and broadband induced absorption along the $\vec{b}$-axis (long dashed and and short dashed box) and the bleaching along the $\vec{c}$-axis (short dashed box). The corresponding spectrally integrated transients are shown in Fig. 5.21. On first sight, all three signals virtually show the same decay dynamics on the longer time-scale. Additionally, they do not follow a mono-exponential but at least a double-exponential form. Therefore, more than simply one relaxation path exists: either the population within that state exhibits at least two scattering channels to lower states or the state is fed by at least one higher state. Accordingly, fitting the transients double-exponentially gives a good agreement with the experiment. The results of the fits are given in Table 5.1. As presumed before, the decay constants are the same within the experimental error, merely the amplitudes differ. Since bleaching is the result of excited carriers, we conclude that after τ_1 ≈15 ps the majority of the carriers are relaxed

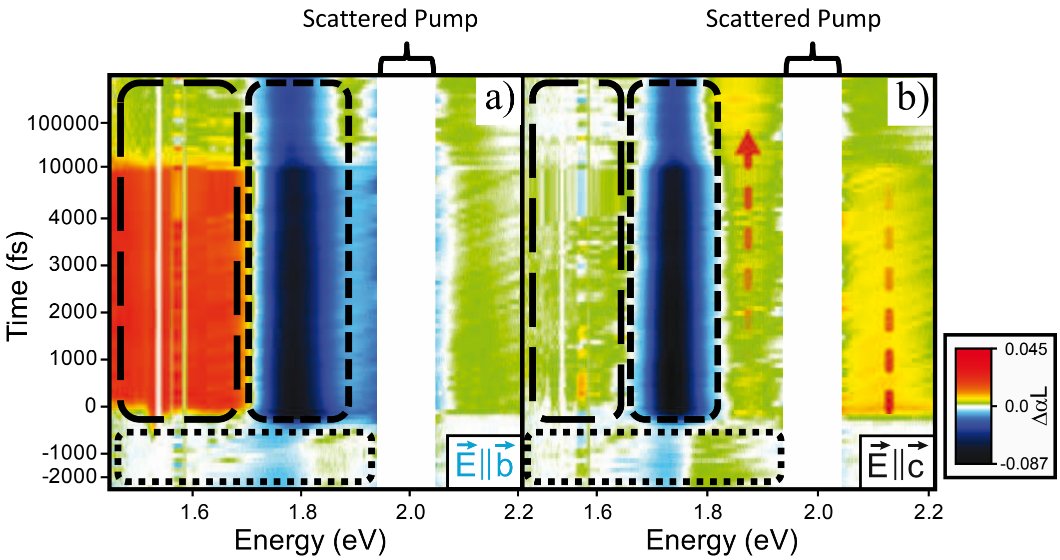

Abbildung 5.20: (a) 2D false-color plot of the ΔαL spectra along the $\vec{b}$-axis. (b) 2D false-color plot of the ΔαL along the $\vec{c}$-axis. The scattered pump light is left out for aesthetic reasons.

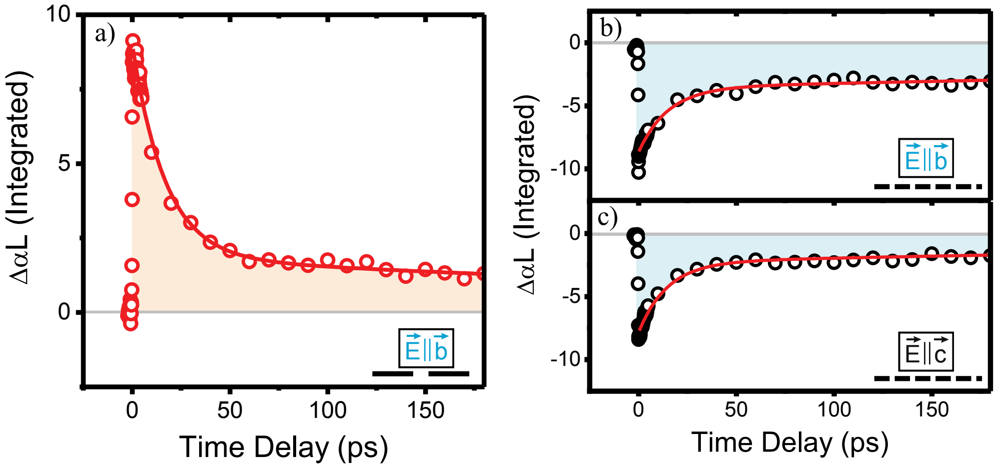

Abbildung 5.21: (a) Transient of the $\vec{b}$-axis' broadband induced absorption (spectrally integrated long-dashed box in Fig. 5.20 (a)). (b) Transient of the $\vec{b}$-axis' bleaching (spectrally integrated short-dashed box in Fig. 5.20 (a)). (c) Transient of the $\vec{c}$-axis bleaching (spectrally integrated short-dashed box in Fig. 5.20 (b)). All transients are shown with corresponding double-exponential fit.

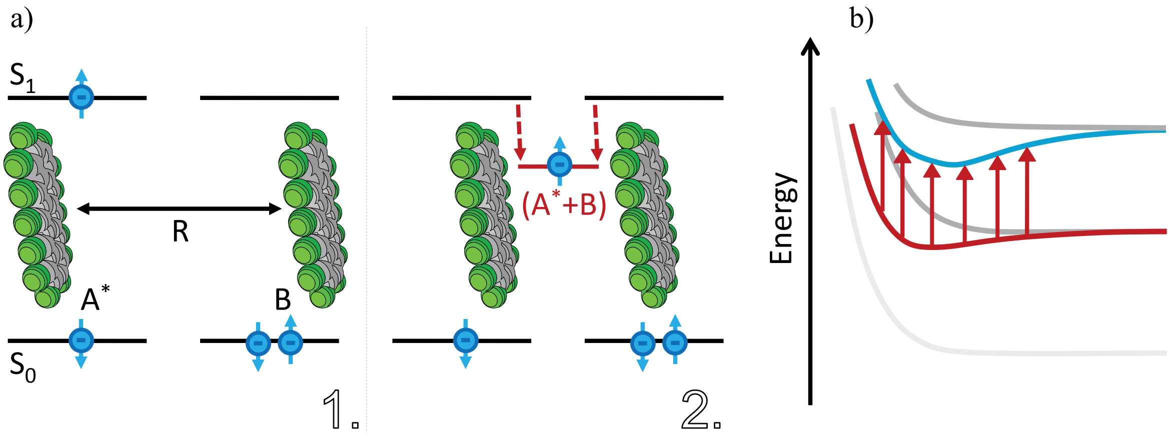

Abbildung 5.22: (a) Dimer picture of the excimer formation. (b) Schematic energy-level diagram of the excimer binding potential and induced absorption into higher states.

back to the ground-state. The long term decay constants (τ_2) are severely error affected, due to the small signal change within the measured time window[13]. Thus, they are nothing more than an estimate. However, approximately one third of the population resides within an excited state indicated by the sustained bleaching and induced absorption.

A first Interpretation: Excimer Formation

In general, induced absorption is a consequence of new absorption channels arising due to excited carriers. Here, the transition dipole moment of the new absorption channels is oriented along the $\vec{b}$-axis. Thus, the excitations have to be delocalized along the $\vec{b}$-axis as expected from the observed resonance coupling in the linear absorption in Ch. 4. This anisotropy in carrier dynamics between $\vec{b}$- and $\vec{c}$-axis has been predicted theoretically by Delgado et. al, where the transfer integrals of HOMO's (t_H) and LUMO's (t_L) along the three crystal axes were calculated.[42] The results are shown in Table 5.2. Strikingly,

---

[13] In general, a good guess of a signal's decay time can be given when its change is measured over two orders of magnitude.

Tabelle 5.2: DFT-PW91 calculated transfer-integrals along the three different crystalline axes of PFP single crystals. From Ref. [42].

Crystalline axis	t_H [meV]	t_L [meV]
$\vec{b}$-axis	-132	73
$\vec{c}$-axis	0	0
$\vec{a}$-axis	3	-7

there are virtually vanishing transfer integrals along the $\vec{c}$-axis and the $\vec{a}$-axis. The dominant coupling present in PFP is along the slip-stacked direction of the $\vec{b}$-axis. In addition, the corresponding transfer integrals of -132 meV and 73 meV are relatively large compared to PEN, where the largest values are found along the diagonal of the *ab*-plane with 85 meV. A comparison of the transfer integrals of PEN and PFP is given in Fig. 5.23. It illustrates the fundamental difference between both systems; PEN is predicted to experience significant 2D coupling within the *ab*-plane, while PFP supposedly shows a 1D behavior. The experimental results confirm the distinct 1D dispersion along the $\vec{b}$-axis, which in turn implies strong charge-transfer character of the excited excitons. Exciton Bohr radius calculation with calculated effective masses from Ref. [42] contradict these findings:

$$\alpha_B^{ex} = \alpha_B^H \cdot \epsilon_{PFP} \cdot \frac{m_0}{\mu} = 0.53\mathring{A} \cdot 2.7 \cdot \frac{m_0}{0.77 m_0} = 1.86\mathring{A}. \tag{5.30}$$

Here the estimated 1.86 Å delocalization is less than half the amount of the $\vec{b}$ lattice vector with 4.45 Å, which indicates, that the effective mass approximation is not valid in organic crystals.

As mentioned in the beginning of Sec. 5.1, partially delocalized excitons are precursors for excimer formation. In general, excimer formation is a diabatic process[14], where the

---

[14] Born-Oppenheimer approximation is not valid.

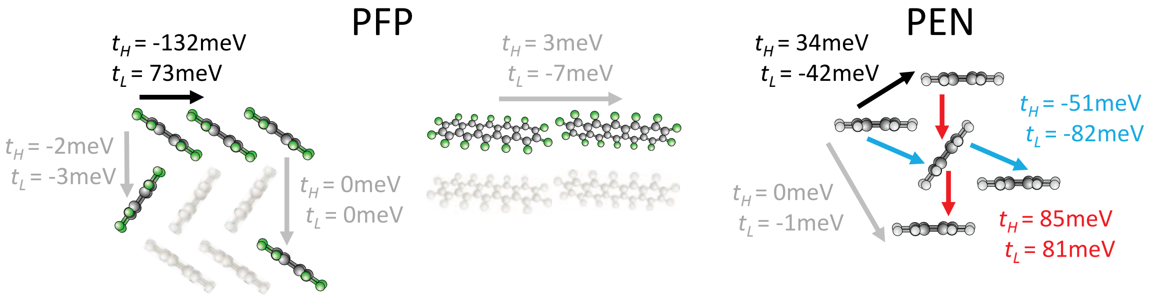

Abbildung 5.23: Comparison of transfer-integrals of PFP and PEN. Significant coupling in PFP is only found along the $\vec{b}$-axis, whereas in PEN there is considerable 2D-coupling within the ab-plane.

atomic disposition in the participating monomers is changed and the system's energy is reduced, schematically depicted in Fig. 5.22. Accordingly, the formation evolves through a conical intersection of two crossing potential energy surfaces as shown in Fig. 5.24 (a). In the simplified pictures of Fig. 5.22 and Fig. 5.24 the excimer formation is parameterized only by the generalized coordinate R of two monomers, illustrated as the intermolecular distance. The intermolecular distance just serves as an example for R and should not be considered as the general case; all kinds of intra- and intermolecular conformational changes can be a part of the formation process. The conical intersection of repulsive and bonding state is the point where both potentials cross, in Fig. 5.24 approximated as the 1D cut through their potential energy surfaces parallel to R. Moreover, it is assumed, that the shown path portrays the global minimum of all possible paths along the potential surfaces.

Now, the system's dynamics can be described in terms of wave-packet-dynamics [97]; The system is excited from the weakly bonding ground-state into a repulsive state and evolves as a wave-packet along the repulsive energy potential surface (first step in Fig. 5.24 (a)). While the excited system propagates along the potential surface the probe invokes stimulated emission leading to radiative relaxation of the system from excited to ground-state. The stimulated emission is observed as bleaching, which shifts in energy with time-delay (see Fig. 5.24 (b)). When the system has reached the conical intersection, it crosses into the binding excimer potential and new absorption channels emerge observed as induced absorption. So, the induced absorption along the $\vec{b}$-axis are

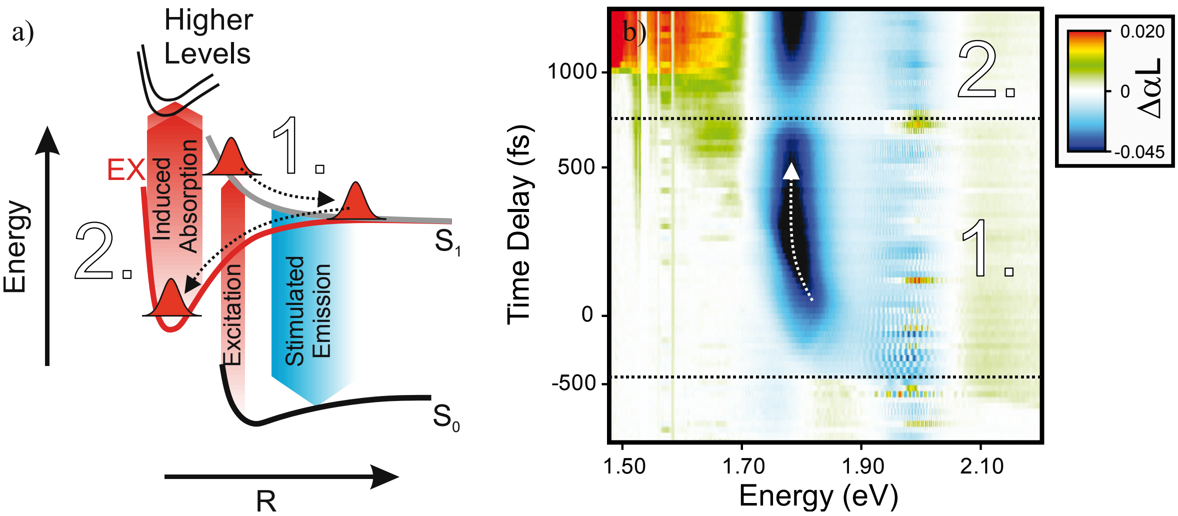

Abbildung 5.24: (a) Proposed wave-packet dynamics of excimer formation in PFP through a conical intersection. (b) High temporal resolution of the differential absorption along the $\vec{b}$-axis. The signal is not dechirped.

interpreted as transitions between different excimer states, as sketched in Fig. 5.22 (c). When the wave-packet has crossed into the excimer potential, the stimulated emission is reduced, due to vanishing effective overlap between excimer and ground-state wave functions. However, the bleaching recovers, as the excimer inhibits the fundamental transition. The combination of both effects results in the observed dip in the bleaching transient(Fig. 5.24 (b)). Therefore, the dynamics through the conical intersection can be directly monitored in pump-probe spectroscopy.

According to the measurements, the conical intersection is reached after approximately 700 fs. This is around one order of magnitude slower than the wave-packet dynamics through the conical intersection of the Rhodopsin molecule after resonant excitation.[98] Tentatively, this discrepancy is explained by the different energies of the mediating quasi-particles: In Rhodopsin, it is an intra-molecular change of conformation mediated by vibrons, typically in the range of a few hundred meV ($200\,\text{meV} \rightarrow T \approx 20\,\text{fs}$); in PFP crystals, it is in first approximation an inter-molecular change of conformation, mediated by phonons in the range of a few meV ($10\,\text{meV} \rightarrow T \approx 400\,\text{fs}$).

Nonetheless, one should keep in mind that the PFP considerations are done by ignoring the crystalline surrounding, where the distances between the molecules along the

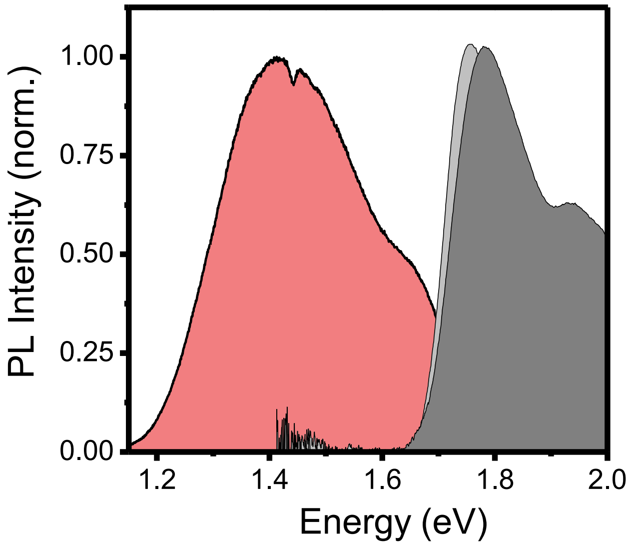

Abbildung 5.25: CW photoluminescence measurement of PFP with the same excitation conditions as in the pump-probe experiments. The gray shaded areas show the linear absorption along the $\vec{b}$- and $\vec{c}$-axes as a reference.

$\vec{b}$-axis are equidistant, i.e., excitations exhibit periodic boundary conditions. Thus, the excitations between two nearest neighbors are indistinguishable, exceeding a dimeric treatment of the problem. Consequently, the knowledge of the full energy potential of the crystal is necessary to gain a more quantitative understanding.

Excimer formation occurs, when it lowers the excited system's energy and its formation-path along the potential surface is energetically favorable. One possible way for the system to relax back to the ground state is by spontaneous emission. As mentioned in Sec. 5.1, the energy reduction results in featureless photoluminescence shifted to lower energies compared to the fundamental transition in linear absorption. Although, the ground- and excimer-states have a reduced wave-function overlap it is finite, so that radiative recombination is expected. In Fig. 5.25 photoluminescence spectroscopy of the PFP crystal is presented, where the excitation conditions are set equal to the pump-probe measurements. We observe a broadband, featureless[15] signature below the

---

[15] The small dip is a pixel artefact in the detection scheme.

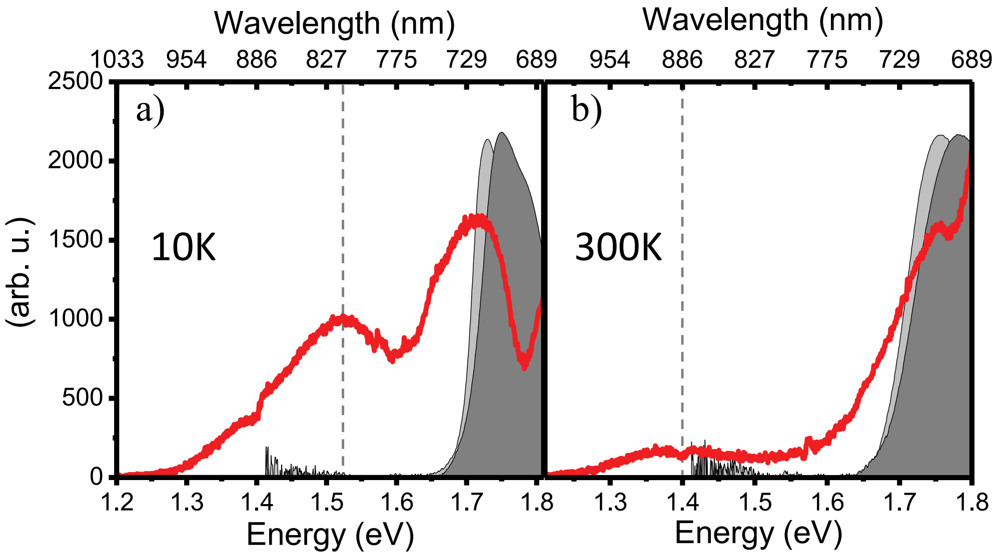

Abbildung 5.26: Temperature dependent CW photoluminescence spectroscopy of the PFP crystal. The excitation energy was set to 2.33 eV. (a) at 10K . (b) at 300K.

fundamental transition with its peak intensity at 1.4 eV. The measured photoluminescence corroborates the excimer formation hypothesis, since a Stokes shift of 300 meV is incompatible with a vibronic progression. Additionally, the 300 meV give an estimate of the binding energy, which is gained by excimer formation compared to the exciton. Temperature dependent CW photoluminescence measurements, with the excitation energy set to 2.33 eV, reveal an unexpected shift of the peak position to higher energies, see Fig. 5.26. The energy difference between the lowest photoluminescence peak position and the fundamental transition is reduced to 195 meV, resembling the energy of the dominant vibron, identified in the previous chapter in the absorption spectrum. So, similar to α-Perylene, in PFP the low-energy excimer like photoluminescence at room temperature seems to change to a monomeric photoluminescence at 10 K. However, the low energy tail does not vanish at 10 K, on the contrary, it is slightly increased (cf. Fig. 5.26 (a,b)). Therefore, the vibronic progression emerges without replacing, but dominating the excimeric photoluminescence .

According to Fermi's Golden Rule, the rate of radiative recombination, in first approximation, is proportional to the square of the dipole matrix element of initial and final state. Since the overlap of excimer and ground state wavefunction is small, the expected photoluminescence decay rate should be slow. For instance, this relation can be observed in TRPL measurements of the quantum confined Stark effect in ZnO, where the fundamental photoluminescence decay rate decreases with reduced electron-hole wavefunction overlap.[99] Automatically, for excimer relaxation in PFP this means, that other non-radiative decay mechanisms become important. As mentioned in the previous section, the decay dynamics of the induced absorption, which is now associated with the excimer, shows an at least double exponential decay. Consequently, radiative recombination is not the only dominant decay mechanism.

5.2.3 Non-linear absorption of Perfluoropentacene: the a-axis

The $\Delta\alpha$L-dynamics in PFP show two distinct time-regimes, a fast decay with a decay constant of 15 ps and a slow decay with a decay constant of 1 ns. The fast relaxation channel is the radiative recombination of the excimer, identified in the previous section. The second decay is significantly slower pointing to an excited triplet state, which is dipole forbidden and consequently cannot recombine radiatively in an ideal organic crystal[16]. In order to verify, whether the system relaxes into a triplet state, pump-probe spectroscopy along the $\vec{a}$-axis of the PFP crystal is performed. The reason to look for a triplet response in the $\vec{a}$-axis lies within the crystalline packing motif of PFP. The long axis of the PFP molecules are oriented virtually parallel to the $\vec{a}$-axis. Apparently, the same dipole-moment orientation is predicted for the lowest, dipole allowed triplet intra-system transitions by single molecular TD-DFT calculations, namely $T_1 \rightarrow T_2$ (1.11 eV; $f_{osc} = 0.004$) and $T_1 \rightarrow T_4$ (2.16 eV; $f_{osc} = 0.581$) with their corresponding transition energies and oscillator strengths given in brackets.[48] If an inter-system crossing occurs, these triplet transitions should be observed as induced absorption in pump-probe spectroscopy.

In Ch. 4 it is shown, that the dipole moment of the singlet exciton is oriented along the short axis of the molecule, hence, transferred to the crystalline phase it corresponds

---

[16] Here, a crystal without incorporated heavy atoms in any sense, so that spin-orbit coupling is negligible.

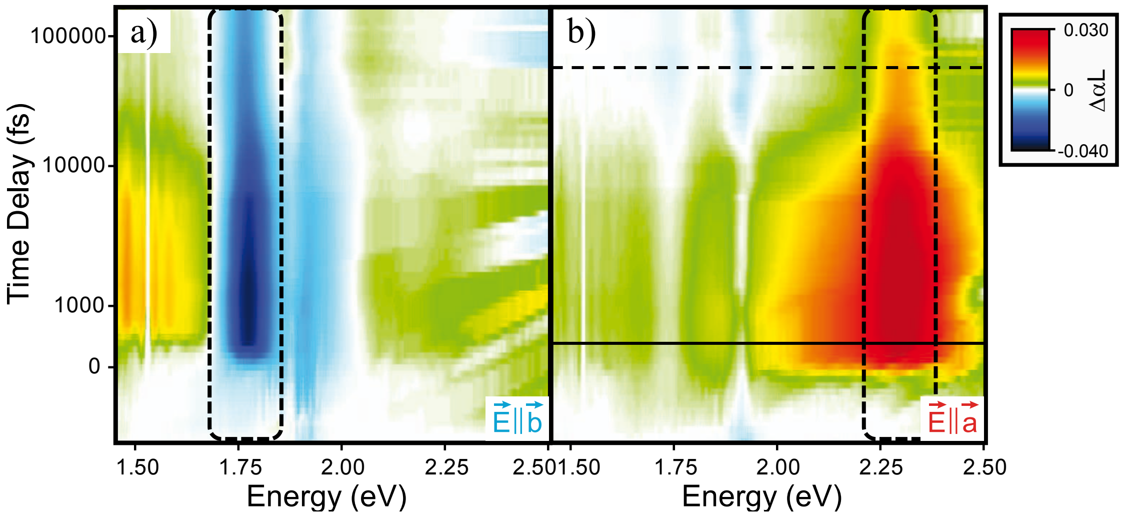

Abbildung 5.27: ΔαL-measurements of PFP crystal (a) along the $\vec{b}$-axis (b) along the $\vec{a}$-axis, shown as 2D false-color plots. Dashed boxes mark the integrated spectral region for the extracted transients in Fig. 5.28 (c). Horizontal lines mark the time delay positions of the shown ΔαL-spectra shown in Fig. 5.28 (a,b).

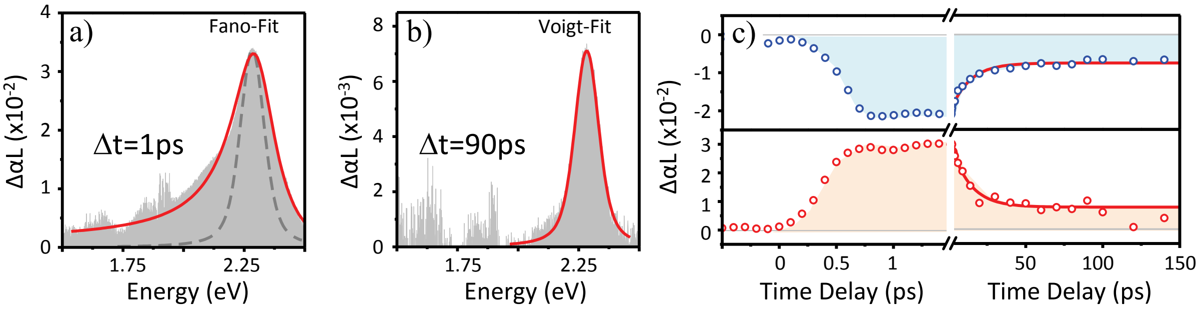

Abbildung 5.28: (a) Grey shaded area: ΔαL-spectrum along the $\vec{a}$-axis at a time delay of 1 ps showing an asymmetric induced absorption at 2.28 eV. Red line: Fano-fit of the asymmetric peak. (b) Grey shaded area: ΔαL-spectrum along the $\vec{a}$-axis at a time delay of 90 ps. Red line: Voigt-fit of the symmetric peak. Same Voigt-fit with adapted amplitude is shown in (a) as a dashed line. (c) Top: Transient of the exciton bleaching along the $\vec{b}$-axis. Bottom: Transient of induced absorption along the $\vec{a}$-axis.

to the $\vec{b}$- and $\vec{c}$-axis. As a result, there is vanishing absorption along the $\vec{a}$-axis in the relevant spectral region from 1.5 eV to 2.5 eV, except for a residual response of the singlet exciton, due to a tilt angle of 11° of the molecules' long axes in respect to the crystalline axis. Therefore, singlet exciton bleaching, broadening or shift signatures cannot superimpose the non-linear response, reducing related misinterpretations to a minimum. On the other hand, the pump pulse polarization inevitably needs to be set along the $\vec{b}$-axis, otherwise the carrier injection would be rather challenging. So the excitation conditions are the same as in Sec. 5.2.2 with a pump pulse energy of 1.95 eV. Again, the probe polarization is set according to the desired crystal axis, i.e. along the $\vec{b}$- and $\vec{a}$-axes, which are optically addressable with normal incidence in PFP crystals grown on KCl(100) substrate.

The $\Delta\alpha$Lresults for both crystal axes are shown as 2D false-color plots in Fig. 5.27. As expected, the $\Delta\alpha$L-measurements of the $\vec{b}$-axis in PFP/KCl(100) shows the same dynamics as the $\Delta\alpha$L-measurements of the $\vec{b}$-axis in PFP/NaF(100), emphasizing its intrinsic crystalline origin. Strikingly, along the $\vec{a}$-axis, immediately after excitation an asymmetric induced absorption is observed at an energy of 2.28 eV. The peak energy deviates from the calculated single molecular $T_1 \rightarrow T_4$ transition by 120 meV. In respect of the general challenges in DFT calculations to gain quantitative valid results for transition energies in combination with neglecting crystalline boundary conditions, the observed induced absorption is in very good agreement with theory.

In Fig. 5.28 (a,b) $\Delta\alpha$L-spectra along the $\vec{a}$-axis are shown for time delays of $\Delta t = 1\,ps$ and $\Delta t = 90\,ps$ marked as solid and dashed lines in Fig. 5.27 (b). Evidently, at early time delays the induced absorption has an asymmetric line-shape, which successively evolves into a symmetric one. The symmetric peak ($\Delta t = 90\,ps$) is fitted with a Voigt-function, capturing the associated lifetime, including the inhomogeneity in the sample. The asymmetric peak ($\Delta t = 1\,ps$) is fitted with a Fano-function, which is typically observed when the transition amplitude associated with a resonance experiences constructive and destructive interference with a continuum of background transitions[100]:

$$f(E) = \frac{(q+\epsilon)^2}{1+\epsilon^2}\ ;\ \epsilon = \frac{E - E_\phi - F}{\frac{1}{2}\Gamma}, \tag{5.31}$$

with the Fano parameter q, giving the ratio of the transition probabilities to the discrete and the continuum states, the resonance energy E_ϕ, the homogeneous broadening Γ and the resonance shift F, resulting from configuration interaction. The Voigt-fit with adapted amplitude fails to capture the line shape of the asymmetric peak (gray, dashed line in Fig. 5.28).

The dynamics of the induced absorption is analyzed in Fig. 5.28 (c), where transients of the spectrally integrated regions shown as dashed boxes in Fig. 5.27 are given. The rise dynamics of the exciton resonance's bleaching along the $\vec{b}$-axis and of the induced-absorption along the $\vec{a}$-axis are identical and occur simultaneously within the time resolution. Additionally, the decay dynamics of the $\vec{a}$-axis follows at least a double-exponential form, similar to the $\vec{b}$-axis. In particular, double-exponential fits yield the following decay constants: $\tau_1 = 12 \pm 3\,\mathrm{ps}$ and $\tau_2 = 0.5 \pm 0.3\,\mathrm{ns}$. Consequently, bleaching and induced absorption showing the same dynamicsresult from the same excited species within PFP.

Interpretation: Correlated Triplet-Pair Formation

As previously speculated in Sec. 5.2.2 and confirmed in this section, the excited carriers predominantly reside within the triplet system after 15 ps. However, the identified triplet intra-system transition $\mathrm{T}_1 \rightarrow \mathrm{T}_4$ at 2.28 eV rises on the same timescale as the bleaching of the singlet exciton resonance and, hence, is observed immediately after excitation. This fast or rather instantaneous inter-system crossing is explained by singlet exciton fission, which is consistent with the expected large fission rate along the $\vec{b}$-axis, due ot the slip-stacked packing motif. In the introduction to singlet exciton fission the process is artificially separated into two steps, while it is mentioned, that in presence of CT-excitons it is reduced to simply one, mediated by direct coupling between CT-exciton and $^1(TT)$. The instantaneous rise of the triplet transition in combination with the observed CT-exciton contributions, identified as broadband induced absorption along the $\vec{b}$-axis, lead us to the conclusion, that singlet exciton fission in PFP is directly mediated. Therefore, the asymmetric induced absorption along the $\vec{a}$-axis is attributed to $^1(TT)$; the afore mentioned nine non-degenerate sub-levels of this cor-

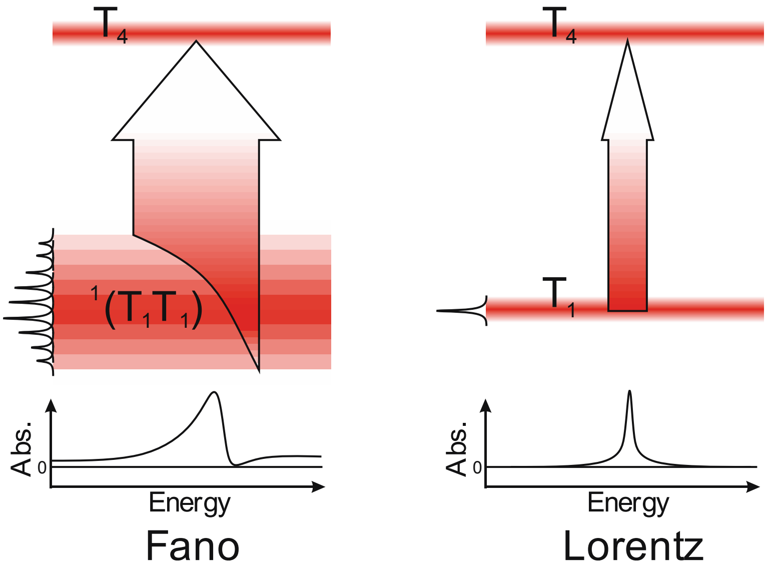

Abbildung 5.29: Schematic diagram of the line-shape evolution of the induced absorption along the $\vec{a}$-axis. Interference of the nine $^1(TT)$ sublevels' transition amplitudes results in the observed Fano-resonance. When the coherence is lifted a symmetric resonance remains.

related triplet pair state act as a quasi-continuum, where the transition amplitudes of the intra-triplet resonance $T_1 \rightarrow T_4$ interfere. The result is the observed Fano-like resonance. As soon as the coherent state is lifted and the triplet excitons act independently, the $T_1 \rightarrow T_4$ resonance exhibits a Lorentzian line-shape or in the case of inhomogeneous broadening a Voigt line-shape. The origin of the resonance's appearance is illustrated in Fig. 5.29. The coherence of $^1(TT)$ decays predominantly by radiative recombination, whereas approximately one third diffuses into triplet excitons evaluated by the bleaching ratios at short and long delay times.

The triplet excitons are generally regarded as strictly Frenkel-type excitons, completely localized to one lattice site, i.e., the molecule. Hence, a crystalline, anisotropic response in PFP is not expected, due to the rectangular packing motif. However, evaluating the induced absorption below the bleaching for the $\vec{b}$- and $\vec{c}$-axis yields a significant anisotropy over the entire temporal range. This is shown in Fig. 5.30, where the same spectral region along both axis is integrated, in order to extract the transients. Again, the transition dipole moment of the broadband induced absorption is oriented along

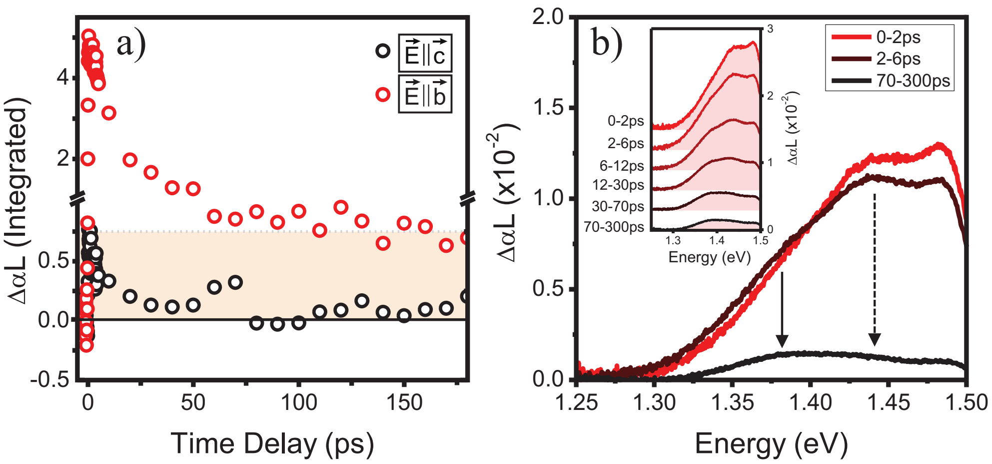

Abbildung 5.30: (a) Transients of the induced absorption in the spectral region of 1.5 eV to 1.7 eV: red dots $\vec{b}$-axis, black dots $\vec{c}$-axis. An anisotropic triplet response is observed. (b) Spectral evolution of the induced absorption along the $\vec{b}$-axis with time delay. The induced absorption changes when the spin-system changes.

the $\vec{b}$-axis of PFP. Accordingly, the triplet exciton is not confined to one molecule, but is to some extent delocalized similar to the singlet exciton.

Since the excited excitons transfer from a delocalized, singlet-like state into a delocalized, triplet-like state a qualitative, spectral change within the induced absorption should be observed. The spectral evolution of the broadband induced absorption is given in Fig. 5.30 (a). Clearly, the initial line-shape changes; the resonance at 1.44 eV disappears, while the low-energy resonance at 1.38 eV prevails and eventually dominates the spectrum. As the broadband induced absorption is polarization dependent, transitions of captured excited carriers at defect states are ruled out. Therefore, the broadband-induced absorption-spectrum monitors the transition from the singlet-like $^1(TT)$ excimer state to the individual triplet excitons. Furthermore, the triplet exciton probably resides in a similar excimer state as the singlet exciton, due to the similarity of their induced absorption spectra. Such a triplet excimer is discussed, for instance, in the case of naphthalene dimers.[101]

Turning to Fig.5.20 again, the dotted boxes mark regions with a signal before the time-zero of the experiment. This residual signal indicates that not all excited carriers

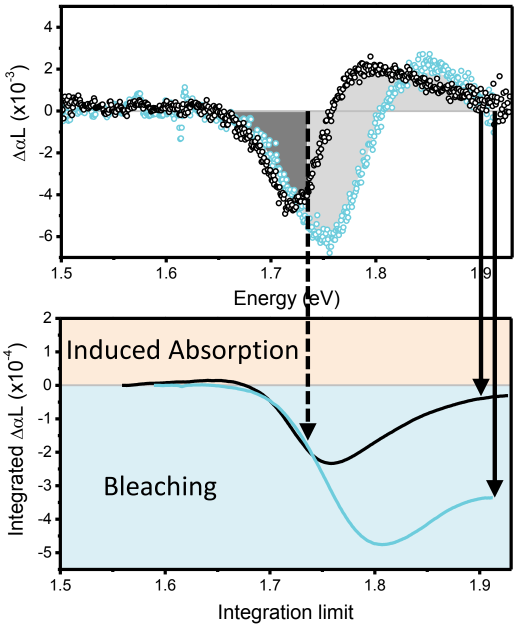

Abbildung 5.31: Top: Spectra of the temporally averaged region marked as dotted boxes in Fig.5.20 (blue dots along the $\vec{b}$-axis; black dots along the $\vec{c}$-axis). Bottom: Integral of the $\Delta\alpha$L-signals.

are back in the ground-state, when the next laser pulse arrives. Due to the 100 kHz repetition rate of the experiment, the time delay of the signal is 10 μs. Since 10 μs is large compared to 2 ps, one can simply temporally average the spectral region marked by the dotted boxes, in order to gain a $\Delta\alpha$L-signal with a very good signal-to-noise ratio for a delay time of 10 μs. The result is shown in Fig. 5.31, still exhibiting a clear anisotropy between the $\vec{b}$- and the $\vec{c}$-axis. Reminiscent of Ch. 3, an idea of the signal's nature is gained by spectrally integrating it. Apparently, setting the integration limit to different energies alters the interpretation severely, e.g. integration of the $\vec{c}$-axis signal until 1.75 eV results in a bleaching signal, while integration until 1.9 eV results in a strong shift signature with a negligible amount of bleaching. Although, the signal along the $\vec{c}$-axis is asymmetric[17] around zero-crossing, it is interpreted as a shift signal with a small residual amount of bleaching. The $\vec{b}$-axis on the other hand, shows a dominant

---

[17] Presumably due to interference with higher energy resonances.[13]

bleaching signal even when setting the integration limit to 1.9 eV. Consequently, triplet excitons block direct transitions within the $\vec{b}$-axis of the PFP crystal even after 10 μs, while the transitions along the $\vec{c}$-axis predominantly are shifted in energy.

5.2.4 Excimer? Correlated Triplet-Pair? or Both?

Now that two species are identified, namely the excimer and the correlated triplet pair $^1(TT)$, the question remains what picture holds. The interplay of both species is of particular interest, as the role of excimers in singlet exciton fission is presently debated controversially. Sometimes, they are considered parasitical [9], while others identify their formation as the mediating mechanism [102, 103, 104].

In the previous section, it is shown that the inter-triplet transition $\mathrm{T}_1 \rightarrow \mathrm{T}_4$ at 2.28 eV along the $\vec{a}$-axis is asymmetrically broadened, due to the sublevels of $^1(TT)$. The rise dynamics of singlet exciton bleaching and induced absorption of $^1(TT)$ are identical within the experimental error. Furthermore, an anisotropic induced absorption along the $\vec{b}$-axis is observed even after the inter system crossing via singlet fission. The spectral signature changes during the transition from $^1(TT)$ to individual triplet excitons, which is a clear evidence that the excited carriers are transferred into a new state. The anisotropic response of the triplet system within the *bc*-plane indicates that the triplet excitons are to some extent delocalized.

Concerning the excimer, in Sec. 5.2.2 Fig. 5.17 shows, that the onset of the associated broadband induced absorption along the $\vec{b}$-axis is delayed compared to the singlet exciton bleaching. In combination with the observed, excimer luminescence at identical excitation conditions and the formation dynamics presumably resulting from the conical intersection, the formation of an excimer type species is plausible. Consequently, both views hold and the comprehensive scenario appears as follows: the initial bleaching results from stimulated emission and blocked absorption experienced by the probe pulse after the crystal is excited. The coupled state of $^1(TT)$ and singlet exciton crosses into the excimer potential diabatically and the broadband induced absorption along the $\vec{b}$-axis emerges. At this point, the stimulated emission is reduced due to the vanishing effective overlap between the excited excimer and ground state wave functions. Howe-

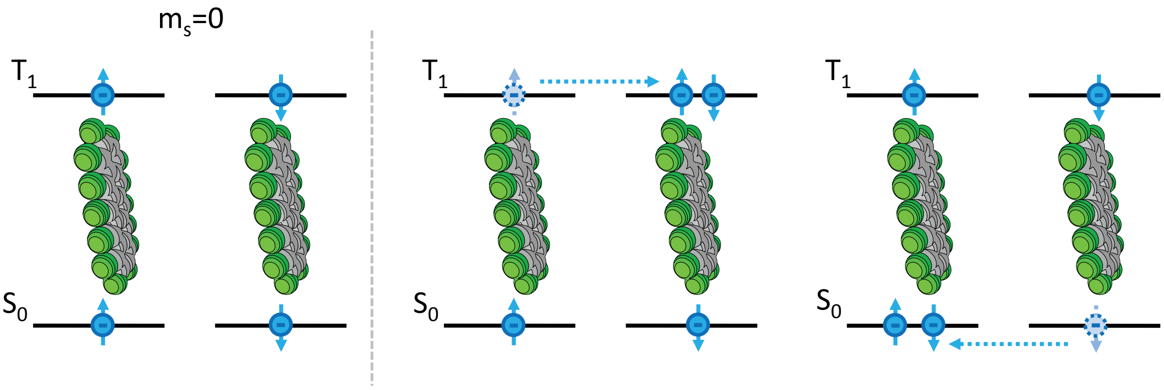

Abbildung 5.32: One possible charge transfer scheme in the $^1(TT)$ state.

ver, the bleaching recovers as the excimer inhibits the fundamental absorption, where it blocks at least two transition channels instead of one. The decay with a constant of around τ_1=12±3 ps is assigned to the radiative relaxation of the excimer, observed as luminescence below the fundamental transition and the dephasing of the $^1(TT)$. The second, slower decay is attributed to relaxation of triplet excitons into the ground-state, which lasts for over 10 μs. Thus, neither is the excimer formation in competition with $^1(TT)$ formation nor is the excimer a precursor for the $^1(TT)$ formation.

The fundamental question of singlet fission is, if the energy balance $E(S_1) \geq 2 \times E(T_1)$ is fulfilled, i.e., if the fission process is exothermic. As a result, the relaxation into an excimeric state with a consecutive singlet fission is rather unintuitive; in general, after excimer formation, the system's energy would be lowered to such an extent, that the energy balance is no longer fulfilled and singlet fission is endothermic. In PEN crystals such calculations have been performed and it was concluded that excimer formation is energetically unfavorable compared to $^1(TT)$ [105]. Now, in PFP, the energy gap between excimer and ground-state is approximately 1.4 eV, determined in Sec. 5.2.2 by the peak energy of the observed photoluminescence. Hence, exothermic singlet fission is expected, as long as the lowest triplet energy is equal or below 0.7 eV ($E(T_1) \leq 0.7\,eV$). Single molecular DFT calculations predict, that the lowest triplet state is at 0.62 eV, thus, well within the limit [47]. In turn this explains, why both relaxation channels are not in competition and observed in the experiment.

Regarding the excimer formation of the coupled state, consisting of singlet exciton and

$^1(TT)$ exciton pair, charge-transfer states may be responsible for the stabilization. In Fig. 5.32 one thinkable charge transfer composition, build from one of the nine presented substates is presented. Since the transfer integrals of both, HOMO and LUMO, are comparably large, possible charge transfer states are further increased, enhancing stabilization.

A simple model

In order to better quantify the decay and formation times of the excimer and the $^1(TT)$, the above findings are implemented into a simple rate-equation. The considered energy levels and relaxation mechanisms are depicted in Fig. 5.33, where singlet exciton (X_{S1}) and $^1(TT)$ are modeled as an indistinguishable coupled state, which act as one. The solid blue arrows mark radiative relaxation channels, whereas the solid red arrows indicate new absorption channels, due to excited carriers observed as induced absorption. The dashed arrows represent non-radiative relaxation, albeit the triplet exciton (X_{T1}) may relax radiatively, however on a nanosecond time-scale. Furthermore, next to the levels, the evaluated and estimated energies are given. The underlying rate-equation model is the following:

$$\begin{aligned}\frac{dN_{S_0}}{dt} &= + N_{S_1} \cdot \tau(S_1 \rightarrow S_0) + N_{X_{S1}} \cdot \tau(X_{S1} \rightarrow S_0) \\ &\quad + N_{EX} \cdot \tau(EX \rightarrow S_0) + N_{X_{T1}} \cdot \tau(X_{T1} \rightarrow S_0) - N_{S_0} G, \end{aligned} \tag{5.32}$$

$$\begin{aligned}\frac{dN_{S_1}}{dt} &= + N_{S_0} G \\ &\quad - N_{S_1} \cdot \tau(S_1 \rightarrow S_0) - N_{S_1} \cdot \tau(S_1 \rightarrow X_{S1}), \end{aligned} \tag{5.33}$$

$$\begin{aligned}\frac{dN_{X_{S1}}}{dt} &= + N_{S_1} \cdot \tau(S_1 \rightarrow X_{S1}) \\ &\quad - N_{X_{S1}} \cdot \tau(X_{S1} \rightarrow S_0) - N_{X_{S1}} \cdot \tau(X_{S1} \rightarrow EX), \end{aligned} \tag{5.34}$$

$$\begin{aligned}\frac{dN_{EX}}{dt} &= + 2 \cdot N_{X_{S1}} \cdot \tau(X_{S1} \rightarrow EX) \\ &\quad - N_{EX} \cdot \tau(EX \rightarrow S_0) - N_{EX} \cdot \tau(EX \rightarrow X_{T1}), \end{aligned} \tag{5.35}$$

$$\frac{dN_{X_{T1}}}{dt} = + N_{EX} \cdot \tau(EX \rightarrow X_{T_1}) - N_{X_{T1}} \cdot \tau(X_{T1} \rightarrow S_0), \tag{5.36}$$

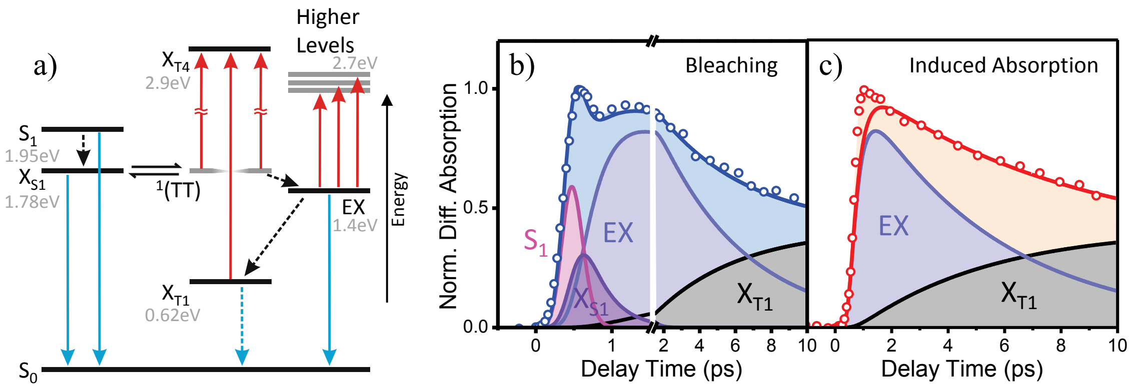

Abbildung 5.33: (a) Energy level scheme and underlying relaxation mechanisms implemented in the rate-equation model. The solid blue arrows represent radiative recombination, the dashed arrows non-radiative relaxation. Red arrows indicate induced absorption. (b) Bleaching transient from Fig. 5.17 (blue circles), rate-equation fit (solid blue line) and the individual contributions (shaded areas). (c) Same as (b) for the induced absorption of Fig. 5.17.

with the states' populations $N_{S_0;\ldots;X_{T1}}$, the excimer state EX and the relaxation rates τ with their respective relaxation paths given in brackets. The experiment is initiated by the population of S_1 with the rate G, where G corresponds to the temporal evolution of the pump pulse and is modeled according to the cross-correlation of pump- and probe pulse (cf. Ch. 3) as a Gaussian with a Γ_{FWHM} of 300 fs:

$$G(t) = \frac{A_0}{\sqrt{2\pi}\sigma} \exp\left(-\frac{(t-t_0)^2}{2\sigma^2}\right) \text{ with } \sigma = \frac{\Gamma_{FWHM}}{2\sqrt{2ln2}}. \tag{5.37}$$

Once S_1 is populated, the system relaxes back to the ground-state via the several pathways, populating all modeled states along the way. The coupled state of singlet exciton and $^1(TT)$ is simply denoted as X_{S1} and is populated by internal conversion from S_1. Consecutively, the coupled state relaxes into the excimer state EX, where the multiplication process is implemented, since then at least two lattice sites are occupied. The EX state decays radiatively to the ground state or diffuses into individual triplet excitons, which eventually return to the ground state or decay otherwise.

Having established the model to simulate the population dynamics, we are now able to fit the bleaching of the fundamental transition. Here, it is assumed that all populated states contribute equally to the bleaching, following the simple explanation of excited electrons no longer being available for the fundamental transition. The model is applied to the bleaching and induced absorption transients along the $\vec{b}$-axis shown in Fig. 5.17, where all the significant signatures are present.

The results for both transients are presented in Fig. 5.33 (b,c), where the experimental results are given as open circles, the rate-equation fit as solid lines and the individual contributions as the shaded areas. Excellent agreement is found for both signatures with applying the same set of parameters. Remarkably, even the dip at 700 fs in the bleaching is reproduced. Its origin is the combined effect of stimulated emission from the initial excited state S_1 and the delayed carrier multiplication process, where the coupled state X_{S1} relaxes into the excimer state EX. In the case of the induced absorption, only the EX and the triplet excitons contribute, in agreement with their delocalized nature. The extracted decay rates are given in Table 5.3.

Tabelle 5.3: Decay constant results of the rate-equation model shown in Fig. 5.33.

Relaxation channel	τ [fs^{-1}]	τ^{-1} [fs]	Relaxation channel	τ [fs^{-1}]	τ^{-1} [fs]
$\tau(S_1 \rightarrow S_0)$	1×10^{-2}	100	$\tau(EX \rightarrow S_0)$	1.1×10^{-4}	9000
$\tau(S_1 \rightarrow X_{S1})$	2.8×10^{-3}	350	$\tau(EX \rightarrow X_{T1})$	8.3×10^{-5}	12000
$\tau(X_{S1} \rightarrow S_0)$	6.1×10^{-4}	1650	$\tau(X_{T1} \rightarrow S_0)$	2.5×10^{-6}	400000
$\tau(X_{S1} \rightarrow EX)$	2.5×10^{-3}	400			

5.2.5 Higher Energy Resonances

The formation of ${}^{1}(TT)$ with the consecutive relaxation into an excimer state is identified in the previous sections. Due to the presence of excited carriers the fundamental transition energies are altered; the system resides in an excited state with changed interaction potentials and consequently exhibits a changed absorption behavior. In inorganic semiconductors for instance, excited carriers screen the Coulomb attraction of electron and holes, resulting in lower exciton binding energies and a shifted exciton resonance to higher energies. On the other hand, the excited carriers also induce a bandgap renormalization, which shifts the bandgap to lower energies; in the special case of GaAs these two effects annihilate each other.[13] In addition to Coulomb induced effects, also spin orientation introduces changes in the fundamental absorption, e.g., the spin bandgap renormalization observed in Ge/SiGe quantum wells.[106]

In organic semiconductors, the exciton binding energies are significantly higher and plasma at these excitation energies is not found, consequently screening effects are improbable. However, two effects should significantly alter the fundamental response: Firstly, the delocalized nature of the excited excitons on a lattice site changes the Coulomb potential of molecules in the vicinity, comparable to bandgap renormalization in inorganic semiconductors, secondly, and this is the dominant contribution, the excimer formation breaks the initial symmetry of the crystal, due to the diabatic relaxation. The latter leads to changed selection rules resulting in new, dipole allowed transitions and forbidden or at least reduced fundamental transitions. These changes of the fundamental reponse are monitored by pump-probe measurements. As shown in Ch. 3, these signatures are not easy to distinguish from other non-linear responses. Nonetheless, when looking at transition energies above the pump energy, at least bleaching signatures from occupied states can be ruled out.

The results of the pump-probe experiments for high transition energies are given in Figs. 5.34 and 5.35. The spectra in Fig. 5.35 are temporally integrated over the marked regions in Fig. 5.34. The linear absorptions of both axes are included for reference as gray shaded areas: $\vec{b}$-axis dark gray and $\vec{c}$-axis light gray.

As expected strong anisotropies are observed. Intriguingly, on first sight, the $\vec{b}$-axis response shows the mirror image of the $\vec{c}$-axis response for energies above 2.2 eV. First,

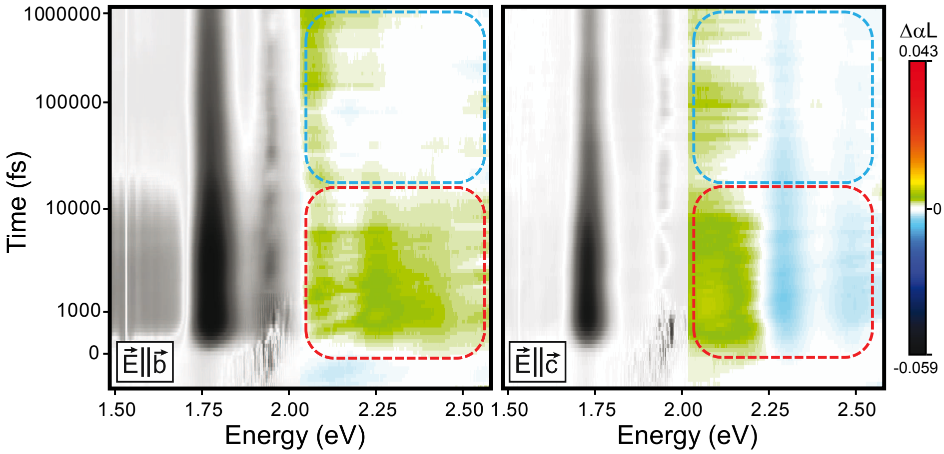

Abbildung 5.34: ΔαL 2D false-color plots of PFP/NaF(100) along the $\vec{b}$- and $\vec{c}$-axis. The high energy (2-2.5 eV) non-linear response also shows anisotropies. The lower energy signals are shown greyed for clarity.

we focus on the $\vec{c}$-axis in Fig. 5.35 (b). The bleaching signatures starting at 2.29 eV resemble the high energy band identified as the monomeric response with a vibronic progression in Ch. 4 (light gray linear absorption). Since no shifts in energy are observed and the energy difference between the two bleaching peaks is unchanged, these signatures can be definitely associated with the high energy band. Consequently, it is a pure bleaching signature of the monomeric response, due to occupied states after excitation, although it is rather unintuitive, that a vibronic progression, or more specifically, a vibron as a boson shows Pauli-blocking. However, the progression is coupled to an electronic excitation, which is fermionic, explaining the observed bleaching.

The induced absorption at around 2.08 eV is either related to the excimer or to a shift in energy of the HOMO-LUMO transition to higher energies. A shift of the HOMO-LUMO transition is less probable, as the induced absorption is energetically broader and exhibits a higher oscillator strength than the bleaching reduces. Therefore, the transition is associated to the excimer. This is corroborated by its dynamics: At longer delay times the signature changes its spectral shape and virtually vanishes, when changing the spin system. The remaining induced absorption results from the asymmetric shift signature of the fundamental singlet exciton transition. The change in spectral signature, as well as the transition from the singlet system into the triplet system is also

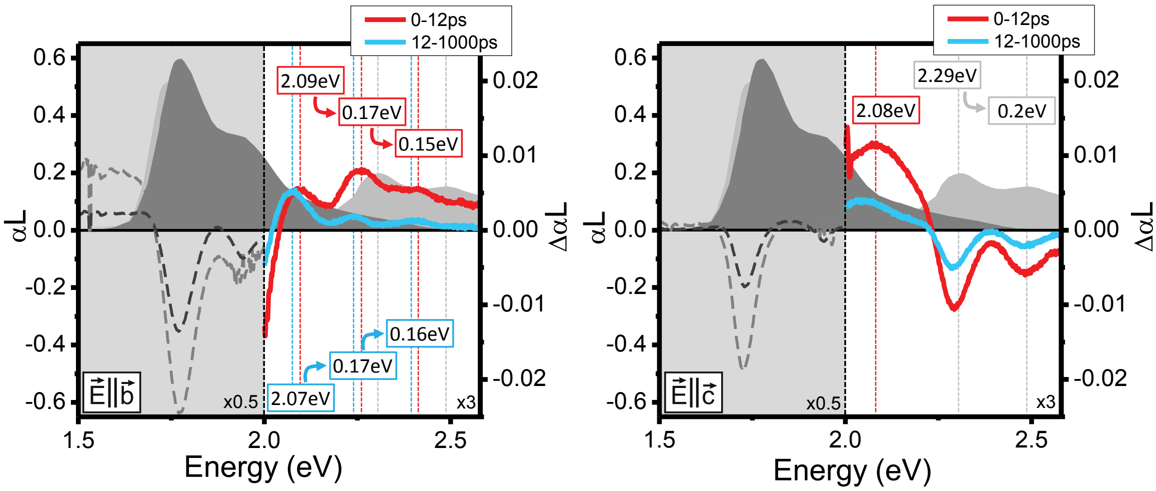

Abbildung 5.35: $\Delta\alpha$L spectra of PFP/NaF(100) along the $\vec{b}$- and $\vec{c}$-axis. The spectra are temporally integrated over the region marked by dashed boxes in Fig. 5.34. The linear absorptions along both axes are given as grey shaded areas for reference.

marked in Fig. 5.20 (b) by the two dashed arrows. Although, the excimer is delocalized along the $\vec{b}$-axis, the electromagnetic field can couple to it perpendicularly. A similar situation is found in inorganic quantum wires, where excitonic resonances are observed with the electromagnetic field set parallel to the direction of the confining potential, yet higher in ernegy.[107]

The $\vec{b}$-axis shows a distinctively different response. Instead of a bleaching, several induced absorption features appear. Additionally, the features evolve spectrally with time and slightly shift to lower energies. As far as the line-shape is concerned, the peaks resemble a vibronic progression, similar to the energy band starting at 2.29 eV in the linear absorption along the $\vec{c}$-axis (cf. red solid line and light gray shaded area in Fig. 5.35 (a)). Since the vibronic progression along the $\vec{c}$-axis is attributed to the monomeric response, the emerging progression along the $\vec{b}$-axis is a strong indication, that the crystalline response is lifted by the excited carriers and monomeric dipole transitions are allowed. Consequently, as expected, the excimer formation alters the selection rules and molecules not involved in the formation process act more indivi-

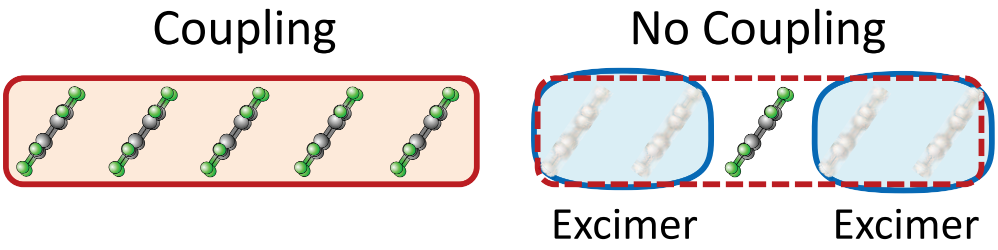

Abbildung 5.36: Simplistic explanation of the emerging monomeric response observed along the $\vec{b}$-axis after optical excitation.

dually. Hence, they can couple efficiently to inner vibrons after optical excitation, in line with Ref. [58]. Strikingly, the absolute position and the energy spacing of the peaks do not match with the monomeric response of the $\vec{c}$-axis. Yet, this is explained by the different background potential evoked by surrounding excimers, or excited carriers in general, in comparison to the ground state potential along the $\vec{c}$-axis. A change in the background potential is then again observed, when the $^1(TT)$ excimer diffuses into individual triplet excitons after approximately 12 ps (blue solid line in Fig. 5.35 (a)); the vibronic progression shifts to lower energies and the oscillator strength of the individual contributions is adapted. A simple scheme explaining the emerging monomeric vibronic progression is shown in Fig. 5.36.

5.2.6 Low Temperature Analysis

In Ch. 4, it is seen that the fundamental transitions are severely broadened at room temperature and cooling the lattice to liquid helium temperatures lead to the observation of the high energy Davydov component along the $\vec{b}$-axis. Accordingly, pump-probe measurements at 10 K are performed along the $\vec{b}$- and $\vec{c}$-axes, with a focus on the excimer formation and its decay. The experiments are performed with a 1 kHz amplifier system, using a liquid nitrogen cooled InGaAs photodiode array as a detector. The InGaAs detector has an effective photon-energy response, ranging from 0.8 eV to 2 eV, well within the desired window.

The results are shown as a 2D false-color plot in Fig. 5.37 for both axes. We observe a

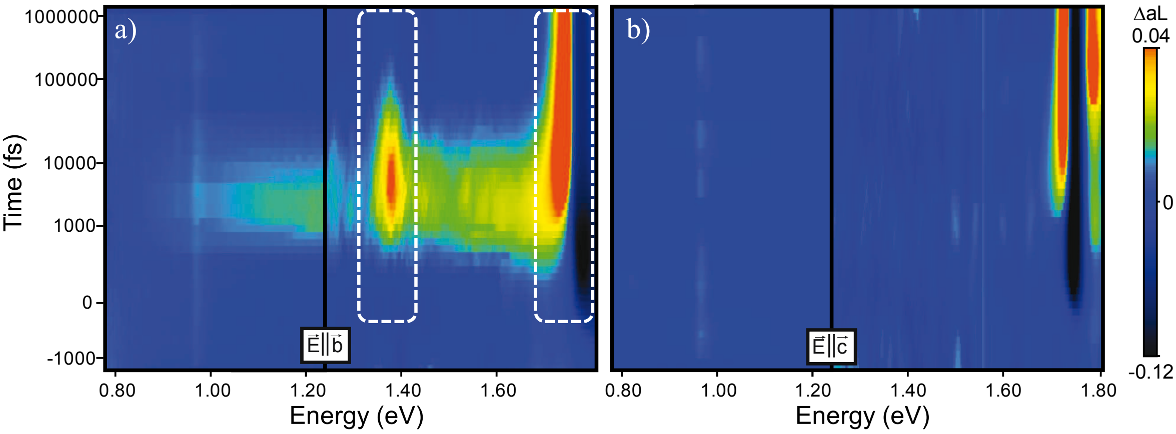

Abbildung 5.37: $\Delta\alpha$L 2D false-color plots of PFP/NaF(100) crystals at 10 K: (a) along the $\vec{b}$-axis; (b) along the $\vec{c}$-axis.

broadband induced absorption along the $\vec{b}$-axis with a distinct resonance at 1.38 eV. As expected, this signature is not found along the $\vec{c}$-axis, in agreement with room temperature measurements. The broadband signal extends over the entire low-energy spectral range, emphasizing the delocalized nature of the excimer and its continuum-like intersystem transitions (cf. schematic illustration in Fig. 5.22 (b)). Remarkably, already the 2D plots reveal different dynamics between the distinct resonance and the broadband signature; the distinct resonance lasts at least an order of magnitude longer. In order to further analyze and quantify this, spectra and transients of the $\vec{b}$-axis are extracted and given in Fig. 5.38 and Fig. 5.39.

Figure 5.38 shows the comparison of the broadband induced absorption spectrum at 10 K and its counterpart at room temperature, both along the $\vec{b}$-axis. Note, that the room temperature induced absorption is the one associated to inter-triplet transitions at a delay time of 70 ps. Although, the peak at room temperature is heavily broadened[18], the peak transition energies are comparable. Because of similar long decay times and spectral line-shapes at 10 K and room temperature, the resonance at 1.38 eV is attributed to the same inter-triplet transition. Tentatively, it is assigned to the dipole forbidden $T_1 \rightarrow T_3$ transition, predicted to be at 1.69 eV by single molecular TD-DFT calculations.[48] In a system with inversion symmetry, e.g., single PFP molecules, pa-

---

[18] This is attributed to enhanced phonon scattering.

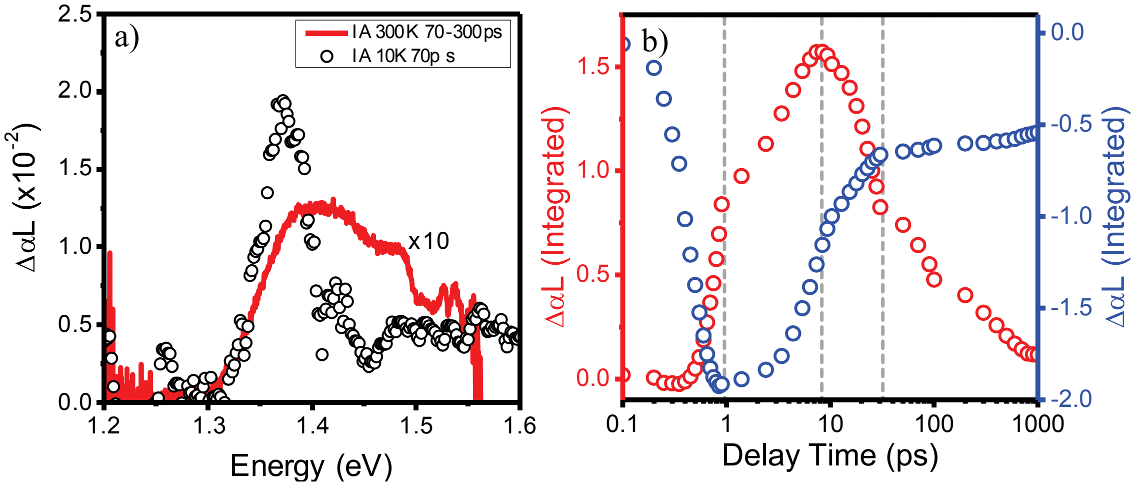

Abbildung 5.38: (a) Comparison of the induced absorption along the $\vec{b}$-axis for 10 K and 300 K. (b) Transients of the bleaching (blue open circles) and the induced absorption (red open circles) spectrally integrated over regions marked as boxes in Fig. 5.37.

rity is a good quantum number and this strict dipole selection rule holds. However, the PFP crystal does not have an inversion symmetry, consequently, in the case of a dipole transition, where now the symmetry of the crystal counts, parity selection rules are weakened.[17] Especially in the case of transitions along the $\vec{b}$-axis, where significant delocalization is present, such a scenario is plausible, resulting in the observed resonance.

In Fig. 5.38 the dynamics of the triplet resonance is compared with the fundamental transition bleaching, both transients are plotted on a logarithmic time delay scale and are extracted from the marked regions in Fig. 5.37 (b). Roughly speaking, three distinct time regimes are observed. During excitation the bleaching transient preludes the induced triplet absorption, then the triplet absorption sets in, when half of the fundamental bleaching is reached. At the peak maximum of the bleaching (≈1 ps) both signal dynamics change; the growth rate of the induced triplet absorption decreases and the bleaching starts to decay. When the induced triplet absorption reaches its maximum, the fundamental bleaching signal is reduced to half its initial value. Subsequently, both

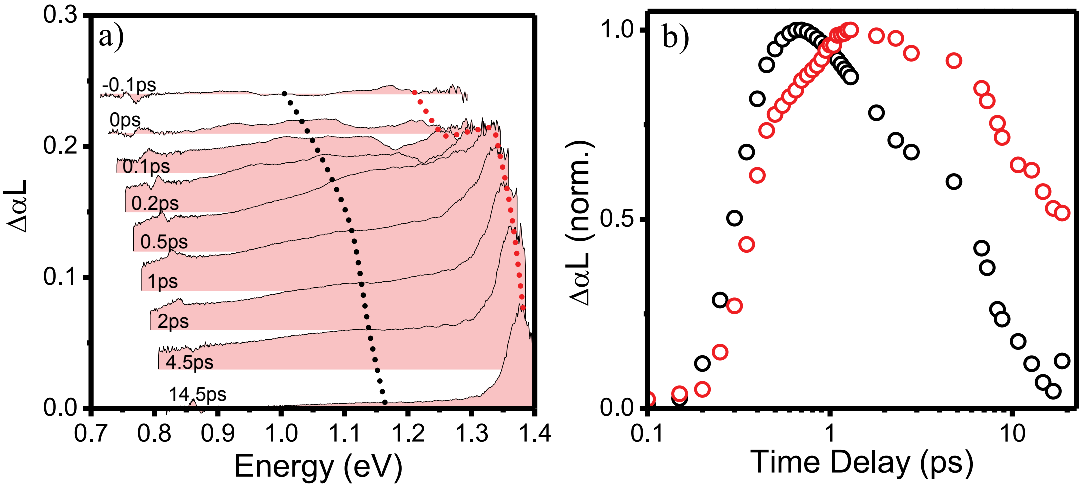

Abbildung 5.39: (a) Temporal evolution of the induced absorption's spectral signature, along the $\vec{b}$-axis. (b) Transient of the peak feature compared to the one of the broadband signature marked in (a).

signals decay on nanosecond time scale. These observations are in good agreement with the interpretation of a diffusing correlated triplet pair with two relaxation channels, i.e., radiative recombination out of the excimer state and the diffusion into individual triplet excitons. The bleaching decays as the radiative recombination proceeds, whereas the triplet induced transition increases, due to an increasing amount of individual triplet excitons. The difference between excimer associated and triplet associated induced absorption is further clarified in Fig. 5.39. Clearly, the evolution of a singlet like excimer into a triplet like excimer is seen. The onset of both signals happen simultaneously within the time-resolution of the experiment, but the subsequent dynamics are different. Initially, the broadband induced absorption is dominant, while the distinct triplet resonance is only weakly detected (after ≈500 fs). The picture changes, as soon as the excimer signature declines, while the distinct triplet resonance prevails (after ≈14.5 ps) eventually observed as an isolated transition.

At the end, the transients of induced absorption below the fundamental transition are compared for the $\vec{b}$- and $\vec{c}$-axes. The results are shown in Fig. 5.40. The $\vec{b}$-axis exhibits

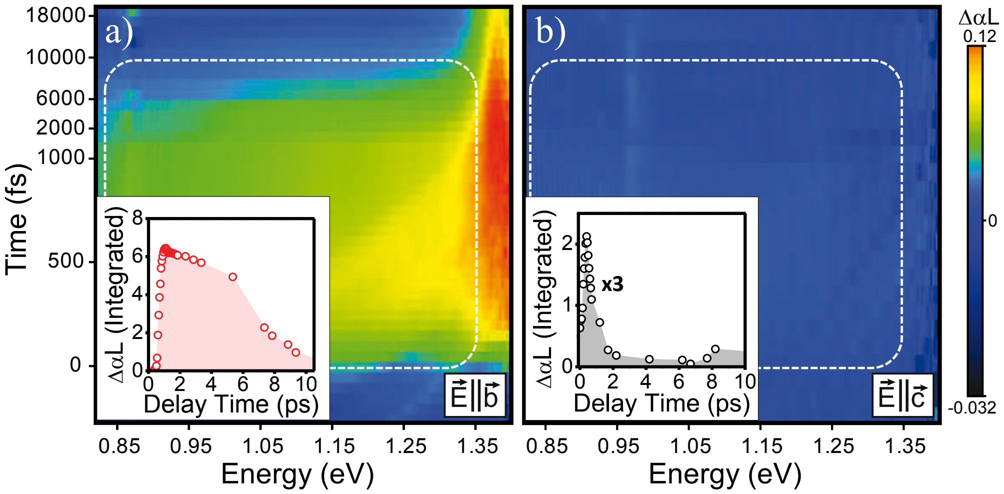

Abbildung 5.40: (a) Induced absorption along the $\vec{b}$-axis. Inset: Extracted transient, spectrally integrated over the white dashed region.(b) Negligible induced absorption observed along the $\vec{c}$-axis. Inset: Extracted transient, spectrally integrated over the white dashed region.

the in detail discussed broadband induced absorption. Along the $\vec{c}$-axis, a residual induced absorption signal is detected, yet significantly weaker and with a sub-picosecond decay time. Due to the weak oscillator strength in combination with its temporal fingerprint, this signature is attributed to a two-photon absorption.

In general, the excitation dynamics at liquid helium temperatures are similar to the one at room temperature. The initial bleaching of the fundamental transition is followed by the broadband induced absorption resulting from the formed excimer and solely observed along the $\vec{b}$-axis. Within the broadband induced absorption a distinct resonance emerges. It shows at least an order of magnitude slower decay dynamics than the broadband excimer signature and is in good agreement with the evolving correlated triplet pair.

In summary, in this chapter a detailed analysis of the excitation dynamics in PFP crystals is given. For the first time it was possible to monitor the process of singlet exciton fission within an organic semiconductor crystal axes resolved. It shows that PFP is an ideal model system, where the fission process is highly anisotropic and happens mono-directional along the $\vec{b}$-axis. Respectively, two important theoretical predictions are verified: the one-dimensional delocalized excitations along the $\vec{b}$-axis [42] and the singlet exciton fission enhancement for slipped stacked molecules [90]. The excited singlet exciton directly couples to the correlated triplet pair $^1(TT)$, which is observed along the $\vec{a}$-axis as the inter-triplet transition $T_1 \rightarrow T_4$ at 2.28 eV. The superposition state of the two triplet excitons dephases on a picosecond time scale, manifested in the evolution of the $T_1 \rightarrow T_4$ line-shape; the initial asymmetric Fano-resonance changes into a Voigt-like resonance. After the superposition is lifted the triplet excitons act individually and return to the ground state on a nano-to-μs time-scale.

Additionally, the coupled excitation of singlet exciton and correlated triplet pair crosses into an excimer state identified by the broadband induced absorption below the fundamental transition, exclusively observed along the $\vec{b}$-axis. Hence, the corresponding dipole moment is oriented accordingly, which implies the one dimensionality of the delocalized excitation. The excimer hypothesis is corroborated by broadband, featureless luminescence 300 meV below the fundamental transition. Consequently, radiative recombination is the second dominant dephasing channel of the correlated triplet pair. Furthermore, due to the changed symmetry along the $\vec{b}$-axis, resulting from the local lattice relaxation, new monomeric absorption features emerge at energies above the associated HOMO-LUMO transition. Along the $\vec{c}$-axis, only a bleaching of the monomeric resonances is seen.

The individual triplet excitons are, in contrast to prevailing opinions, not strictly Frenkel-type. The tentatively assigned $T_1 \rightarrow T_3$ transition is again exclusively observed along the $\vec{b}$-axis. It emphasizes the, in van der Waals bond crystals, comparably strong inter-molecular coupling and the direct consequence of significant delocalization of the excitations. As a result, the collective crystal eigenstates have to be considered, which exhibit mixed states enhancing singlet to triplet transitions by singlet fission and excimer formation.

6 Dephasing of Wannier Exciton Polarization in Germanium

In the last chapter we turn to the inorganic material system of Germanium quantum wells. Their spectrum is dominated by Wannier excitonic resonances which show rich coherent dynamics in non-linear pump-probe measurements. The dephasing times of the induced excitonic polarization play a crucial role in such experiments, thus, their knowledge is inevitable. Here, a methodology is presented capable to determine the excitonic dephasing times by exploiting their coherent non-linear response in pump-probe spectroscopy. As a proof of principle, it is applied to the three excitonic resonances lowest in energy in a Ge/SiGe quantum well sample and compared to their FWHMs in the linear absorption. Furthermore, their temperature dependence is analyzed. At the end, four nominally equal samples are characterized and evaluated in respect to their optical qualities with the developed method.

6.1 Introduction

6.1.1 Sample

Unlike Silicon, the bandgap of Ge is typically labeled quasi-direct as it displays a local conduction band minimum at the Γ-point ≈150 meV above the indirect band gap (see

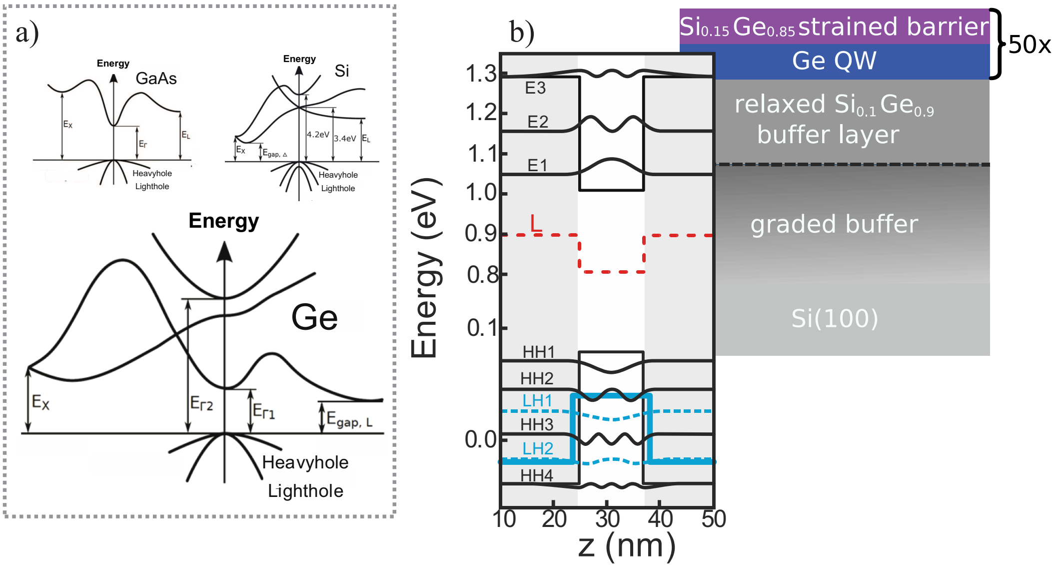

Abbildung 6.1: (a) Bandstructures of the prototypical semiconductors Si and GaAs in comparison to the bandstructure of Ge. (b) Calculation of the lowest electronic subbands with schematic structure of the quantum well samples.

Fig. 6.1 (a)). As a consequence, Ge exhibits optical properties similar to GaAs, a direct-gap semiconductor. Accordingly, typical direct gap characteristics on Ge/Si material systems have been found, including transient gain, direct-gap electroluminescence, optically and electrically pumped lasing, the quantum-confined Stark effect, and a strong dynamical Stark shift.[108, 109, 110, 111, 38, 112]

Some of these experiments are performed on Ge/SiGe quantum wells, heterostructures which confine the electrons to two dimensions. The resulting quantized sublevels in the z-direction are shown in Fig. 6.1 (b) with the corresponding schematic structure of the samples, which will be analyzed in this chapter. All samples named from A to D contain 50 compressively strained 10 nm thick Ge QWs between 20 nm thick $Si_{0.15}/Ge_{0.85}$ barriers grown on a graded buffer on Si as a virtual substrate. All samples are nominally identical but display different optical qualities thoroughly evaluated later.

The band structure shows some noteworthy peculiarities; the global minimum in the conduction band is the fourfold degenerate L-valley which is sketched as the red dotted line in Fig. 6.1 (b). Additionally, the confining potential between light-and heavyhole is

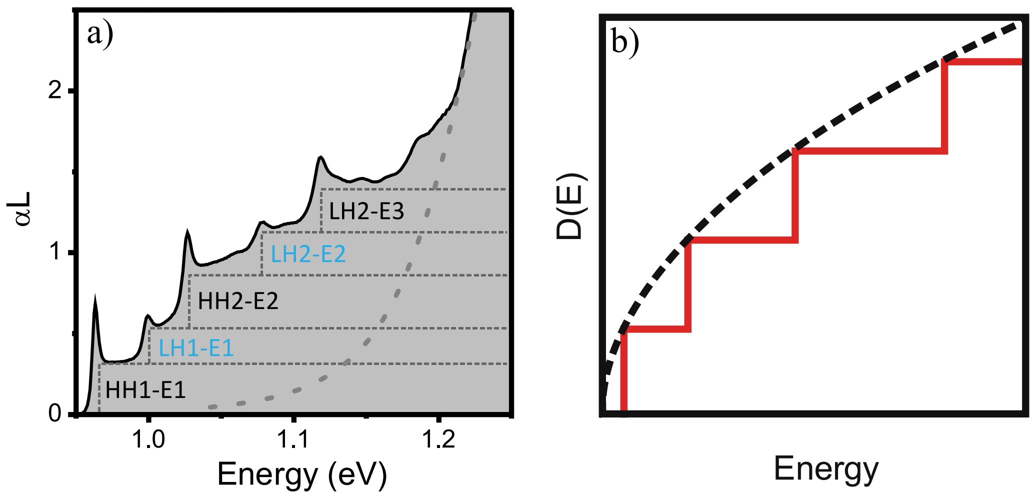

Abbildung 6.2: (a) Linear absorption of the analyzed Ge/SiGe quantum well sample A with the marked sublevels. (b) Density of states of the free electron gas in two dimensions. The dotted line marks the density of states for three dimensions.

not identical; the lighthole potential is not as deep and marked as a blue line.
Due to the confinement, the density of states is reduced and shows a step-like function owing to the quantization. Hence, the absorption of such a system in principle follows its combined density of states and resembles the step-like function, see Fig. 6.2. However, in addition, the sublevels exhibit pronounced excitonic resonances slightly below their continua. They result from the induced excitonic polarization, i.e., Coulomb enhanced pair states of electron and hole.

6.1.2 Excitonic Polarization

During excitation the excitonic polarization is coherent to the exciting electromagnetic field until it is either Coulomb or phonon scattered to form excited, incoherent carriers or re-emitted as radiation. Both processes contribute to the dephasing of the induced excitonic polarization and are encoded in the homogeneous broadening of the resonance.

In general, all coherent effects in optically excited materials depend crucially on the dephasing of the addressed states. The dynamical Stark shift in Ge serves as an example: it is two times larger than in GaAs which is attributed to an increased temporal overlap of pump pulse and the dephasing probe polarization.[36, 38] Hence, the knowledge of dephasing times in material systems, which are typically referred to as T_2-times, is essential in order to interpret and model coherent effects correctly. In particular, it is often used as a phenomenological damping parameter $\gamma = 1/T_2$ in theoretical descriptions which summarizes all underlying processes invoking decoherence after optical excitation.[13]

Assuming a dephasing excitonic polarization as a damped dipole oscillation we expect a Lorentzian lineshape in the spectrum where the T_2-time can be extracted from the Γ_{FWHM} as follows:[17]

$$\gamma = \frac{1}{T_2} = \frac{\Gamma_{FWHM}}{2\hbar}. \tag{6.1}$$

However, this estimate is strongly error-affected when the excitonic resonance exhibits inhomogeneous broadening; then the lineshape becomes a convolution of a Lorentz and a Gauss due to slight fluctuations of the quantum well width. Furthermore, when significant overlap with the continuum exists, particularly in case of the higher subband resonances (cf. Fig. 6.2 (a): transitions from LH1-E1 onwards), it yields grossly wrong results.

Typically, the method to determine macroscopic dephasing times is degenerate four wave mixing (FWM) spectroscopy which has been performed extensively on various systems including bulk Ge.[113, 114, 115, 116, 117, 118, 119] Here, the duration of the FWM-signal is directly governed by the dephasing of the induced polarization. Yet, when excitonic resonances exhibit significant overlap with continuum states, the FWM-signals show rather complicated structures and the extraction of the macroscopic dephasing times of single excitonic resonances becomes tricky.[120]

Ultrafast pump-whitelight-probe spectroscopy offers the possibility to extract the macroscopic dephasing time of the excitonic resonances within one spectrum with relative

ease by exploiting a well-known coherent phenomena known as coherent oscillations.[121] Pump-probe experiments are commonly performed to analyze the dynamics of the incoherent carriers after optical excitation.[120] Nevertheless, one should always consider that the probe signal in pump-probe experiments contains a superposition of coherent and incoherent responses. Especially in the time reversed situation, coherent effects dominate the $\Delta\alpha$L spectrum; the probe pulse first excites a weak polarization in the sample which is then scattered by the much stronger time-delayed pump.
Coherent oscillations are observed, when the initial „slow“ free induction decay (FID) of the probe polarization governed by the reversible and the irreversible phase relaxation comes to an abrupt end, e.g., by the pump-pulse excited high density of carriers (see Fig. 6.3 (b)).[13] This quasi-instantaneous decay in the time domain causes an oscillatory feature in the frequency domain. The microscopic theoretical framework capable to calculate coherent and incoherent excitation dynamics correctly are the semiconductor Bloch equations.[122] Concerning coherent oscillations, their central peak amplitude's dependence on the time delay between pump and probe can be approximated by an exponential decay, if the pump pulse is set to energies high into the continuum and the pump fluencies are large enough to bleach the excitonic resonances:[123]

$$\frac{\Delta T}{T} \propto \exp\left(\frac{\tau_d}{T_2}\right); \text{ for } \tau_d < 0, \tag{6.2}$$

with the differential transmission $\Delta T/T$ and the delay time τ_d. Hence, the dephasing time can be directly extracted from the coherent oscillations' transients.

6.2 Coherent Oscillation Spectroscopy

The measurements are performed in the ultrafast pump-whitelight-probe set-up described in Ch. 3. The excitation energy is tuned well above the bandgap for all experiments with photon fluencies of 1×10^{16} Photons/cm^2 per pulse (100 fs). These high fluencies assure that the required pump conditions are fulfilled in order to apply the approximation of Eq. 6.2. The linear absorption spectra are measured with both the pump-probe

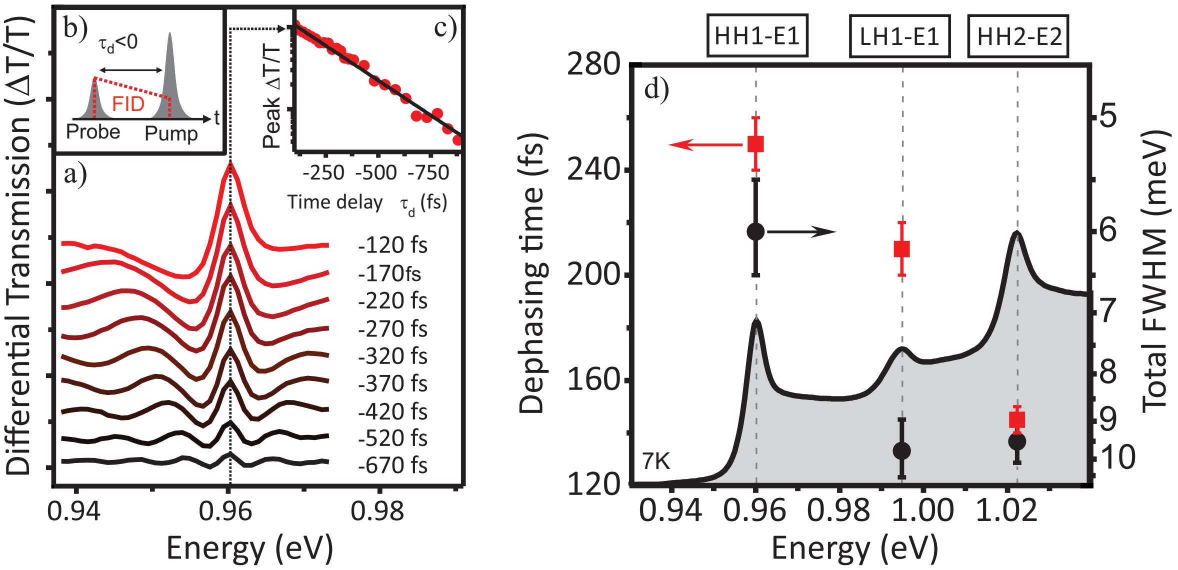

Abbildung 6.3: (a) Measured coherent oscillations from the excitonic resonance HH1-E1 for different time delays between pump and probe τ_d. (b) Schematic illustration of the abrupt end of the free induction decay (FID). (c) Exponential decay of the coherent oscillation's peak amplitude towards negative time delays. (d) Detailed dephasing analysis of the three lowest excitonic resonances in the Ge/SiGe quantum well sample A. Adapted from Ref. [124].

setup and a Fourier-transform spectrometer, where it is taken care of that the lineshape of one sample agrees well in both experiments.

A typical evaluation of the coherent oscillations with the extraction of the dephasing time is presented in Fig. 6.3 (a,c). The differential transmission spectra are plotted versus energy around the HH1-E1 excitonic resonance for various time delays. Clearly, the coherent oscillations are observed with their increasing peak amplitude and their diverging oscillation period with decreasing negative time delays. The extracted intensity of the central peak is given in Fig. 6.3 (c). Applying Eq. 6.2, the single-exponential fit yields a measured dephasing time of 250 fs for the lowest excitonic resonance (HH1-E1). Previous pump-probe measurements on Ge/SiGe quantum wells revealed an intervalley scattering time $\tau_{\Gamma-\mathrm{L}}$ of around 300 fs which can be assumed as the upper limit to form incoherent, excited carriers.[125] Since the extracted dephasing time is comparable to

$\tau_{\Gamma-\mathrm{L}}$, we conclude that the dephasing of the coherent polarization in Ge quantum wells is governed by phonon scattering into the L valleys. Similar assumptions have been made by Rappen et. al. for bulk Ge which is here confirmed for quantum wells.[118] Therefore, the dephasing mechanism is in contrast to direct-gap semiconductors such as GaAs, where Coulomb scattering and intra-valley phonon scattering are the main driving force typically exhibiting dephasing times of several ps in high-quality samples.[17]

The determined dephasing times for the lowest three excitonic resonances for sample A at a lattice temperature of 7 K are plotted in Fig. 6.3(d). The linear absorption of the sample is included as a reference. The analysis yields 250 fs for the HH1-E1 transition, 210 fs for the LH1-E1 transition, and 130 fs for the HH2-E2 transition. In order to interpret these results the peculiarities of the band structure of this sample has to be considered which was previously evaluated by $\mathbf{k}\cdot\mathbf{p}$-calculations and is shown in Fig. 6.1.[126] As mentioned before, the LH1-subband is less confined and has consequently a higher wave function overlap with the barriers. Therefore, an induced LH1-E1 excitonic polarization has an increased probability of scattering with structural defects in the barriers which consequently reduces the dephasing time. The dephasing time of the HH2-E2 excitonic polarization is nearly by a factor two smaller. Two efficient scattering mechanisms are responsible for the fast dephasing: firstly, in Ge quantum wells an inter-subband relaxation process of electrons from E2 to E1 exists during the first 100 fs[127] and, secondly, the hole scattering efficiencies between HH_k-HH_l is two orders of magnitude larger than the LH_k-HH_l efficiencies.[128]

The differences in the dephasing times also manifest themselves in the linear absorption spectra: in Fig. 6.3(d) the determined total FWHMs of the excitonic resonances from the linear absorption are given as black dots. They are determined by the half width at half maximum of the low-energy flank in the linear absorption carefully avoiding any continuum contributions. The total FWHMs of the two HH resonances, HH1-E1 and HH2-E2, are in good agreement with the extracted dephasing times. However, the LH1-E1 resonance's total FWHM is nearly twice as large as the broadening expected from the coherent oscillations' dephasing time. Again it is explained by the the weaker confinement of the LH-sublevel: it leads to a lower oscillator strength which in combi-

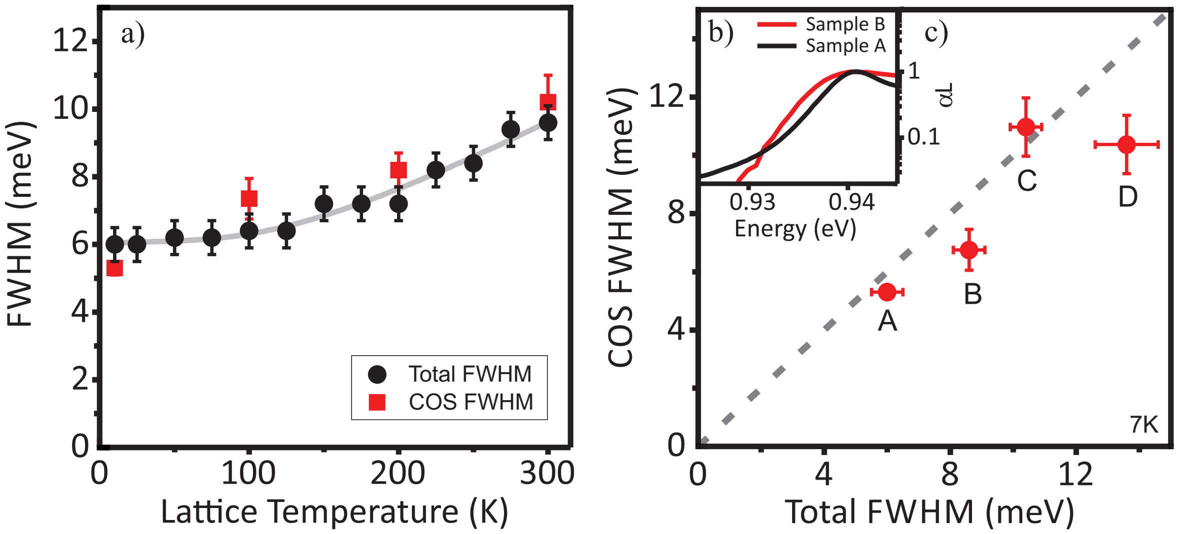

Abbildung 6.4: (a) Temperature dependence of the lowest excitonic resonance's broadening extracted by the coherent oscillation analysis and from the linear absorption. (b) Linear absorption comparison of two nominally equal samples which exhibit two different lineshapes. (c) Dephasing time analysis for four nominally equal samples all exhibiting different optical quality.

nation with the superimposed continuum makes the determination of the resonance's total FWHM from the linear absorption highly inaccurate. Hence, for LH1-E1 the simple estimation of Eq. 6.1 obviously fails to determine the dephasing time correctly. In Fig. 6.4 (a) the temperature dependence of the total FWHM of the HH1-E1 excitonic resonance of sample A from the linear absorption is compared to the extracted broadening from the coherent oscillations. For all measured temperatures, the determined values by the two methods agree well within the experimental error. Thus, the sample's lowest-lying transition is dominated by homogeneous broadening over the entire temperature range. The decrease of dephasing time, i.e., the broadening of the resonance with increasing temperature, is caused by the increase of phonon population providing an enhanced number of possible scattering processes at higher temperatures.[129] At room temperature, a dephasing time of 130 fs is extracted for the HH1-E1 excitonic resonance.

In the last part of this chapter the coherent oscillation analysis is applied to three additional samples (B, C and D) with different linewidths in their linear absorption spectra. The results are shown in Fig. 6.4 (c) where the total FWHM of the HH1-E1 excitonic resonance of the linear absorption is plotted against the extracted broadening from the dephasing times at the lattice temperature of 7 K. All three samples show shorter dephasing times than sample A which correlates with the corresponding broader total FWHMs. These findings are tentatively explained by an increase of interface roughness and structural defects which not only increase the inhomogeneity of the sample (reversible phase relaxation) but also provide new scattering channels for an induced polarization (irreversible phase relaxation), both decreasing the macroscopic dephasing time.[120, 17, 130] In the inset the linear absorption of sample A and sample B is plotted on a logarithmic scale clearly portraying the different lineshapes (Fig. 6.4 (b)). Sample A shows a Lorentzian shape emphasizing the previously identified homogeneous broadening while sample B's shape is more Gaussian-like indicating the dominating presence of inhomogeneous broadening. Accordingly, dephasing times can be used to determine optically high quality samples in Ge/SiGe material systems. Here, sample A is the one with the highest quality, for it exhibits the longest dephasing time with 250 fs. Considering the intrinsic scattering time of 300 fs, this sample exhibits exceptional optical quality.

7 Conclusions

> *„As we all know, everthing was foretold by Aristotle or Jesus Christ. So it is only with timidly throbbing heart that your author dares to ask the deciding question: What might be novel in this article?“ U. Brosa [131]*

Perfluoropentacene (PFP) single crystals are an ideal model system to study the exciton dynamics after optical excitation. For the first time, it was possible to monitor singlet exciton fission crystal-axis resolved, due to the unique growth characteristics of PFP on the alkali-halide substrates NaF(100) and KCl(100). Here, this ultrafast process occurs between the slip-stacked molecules along the $\vec{b}$-axis of the crystal. These findings confirm theoretical works which predict strong inter-molecular coupling along this direction as well as enhanced singlet exciton fission for a slip-stacked geometry. Additionally, the coherent state of singlet and triplet excitons, the correlated triplet pair $^1(TT)$, is identified as an asymmetric Fano resonance polarized along the $\vec{a}$-axis. It emerges as a new absorption channel directly after optical excitation in pump-probe experiments. The resonance is attributed to the inter-triplet system transition $T_1 \rightarrow T_4$ at 2.25 eV which has been predicted previously by TD-DFT. The asymmetric Fano-like lineshape is a result of the interference of the transition amplitudes from the nine $^1(TT)$ sublevels into the excited T_4 state. As soon as the coherence is lifted, the induced transition is observed as a symmetric Voigt resonance.

During the fission process, 300 fs after excitation, the $^1(TT)$ relaxes into an excimer like state observed as broadband induced absorption along the $\vec{b}$-axis. This feature is absent along the $\vec{c}$-axis, showing the virtually exclusive coupling along the slip-stacked packing motif. Predominantly, the $^1(TT)$ recombines radiatively from the excimer-like state to the ground-state manifested in featureless luminescence 300 meV below the lowest exciton transition. The residual triplet excitons, which act as individual excitons after ≈15 ps, decay on a nanosecond timescale. The gained findings were successfully modeled with rate-equations taking into account all participating species.

In summary, the exciton dynamics in PFP occur exclusively along the $\vec{b}$-axis making PFP virtually a 1D system. Here, the opportunity arises to thoroughly study the rich and complex dynamics of interacting molecules in a slip-stacked arrangement. Furthermore, the comparison to other crystal structures have to be pursuit in order to learn more about the correlation between packing motif and exciton dynamics. For instance, on metal surfaces, PFP adopts a planar crystal structure without an herringbone angle, where the distance between slip-stacked molecules is reduced to 3.07 Å.[132] Consequently, the inter-molecular interaction should be further increased changing the exciton dynamics. In addition, synthesis and crystal growth of molecules with partial fluorinated shell offer the possibility to study herringbone crystal structures with changed angles and lateral displacement between slip-stacked molecules.

In Chapter 4 the PFP single crystals are utilized for the first determination of the Davydov-splitting in PFP. Since, the basis molecules adopt a nearly rectangular conformation yielding virtually vanishing transfer integrals, a Davydov-splitting of merely 25 meV is measured. It is a factor five lower than in Pentacene. Yet, due to the large transfer integrals within the $\vec{b}$-axis and the corresponding strong dipole coupling, H-aggregate (J-aggregate) like absorption is observed when the light is polarized parallel to the $\vec{c}$-axis ($\vec{b}$-axis). Intriguingly, these signatures are reduced when the sample is optically excited, indicating the loss of efficient coupling between molecules in the ground and excited state. The temperature dependent measurement revealed a red shift of the lowest exciton transition while the Davydov-splitting remains the same.

In Chapter 6 the dephasing times of excitonic resonances in Ge/SiGe quantum wells were analyzed by evaluation of the coherent oscillations' transients. This approach is a fast and flexible alternative to FWM experiments typically used to determine dephasing times. A dephasing time of 250 fs was extracted for the lowest-lying HH-E1 exciton resonance in the highest quality sample. This is in the order of previously reported intervalley scattering times. Consequently the phonon scattering from the Γ to the L valleys is the dominant dephasing mechanism for the coherent polarization in Ge. The reduced dephasing time of 130 fs at room temperature is a consequence of the temperature dependent phonon scattering rates which increase with temperature. Applying the developed methodology to samples with different linewidths shows that higher interface roughness and an increased number of structural defects further decrease the dephasing times, and an inhomogeneous broadening in the HH-E1 excitonic resonance is observed. Nevertheless, the supremum of sample quality in Ge/SiGe quantum wells is reached when the macroscopic dephasing time approaches the intrinsic scattering time of about 300 fs or a total FWHM of 4.4 meV at 7K.

As a concluding remark; all works concerning the study of PFP are interpreted with the means of an experimental solid-state physicist, hence, based on phenomenological methods. Rigorous quantum-mechanical calculations are necessary to confirm or disprove the stated hypotheses. I could go by James Joyce, *„A man of genius makes no mistakes; his errors are volitional and are the portals of discovery.“*, but I don't walk this way. So my hopes rely on the groups of L. Kronik and J. Neaton to reveal the nature of the excitons in PFP in more detail.

Literaturverzeichnis

[1] J. Bardeen and W. Brattain. The Transistor, A Semi-Conductor Triode. *Physical Review*, 74(2):230–231, July 1948.

[2] R. Hall, G. Fenner, J. Kingsley, T. Soltys, and R. Carlson. Coherent Light Emission From GaAs Junctions. *Physical Review Letters*, 9(9):366–368, November 1962.

[3] W. S. Boyle and G. E. Smith. Charge Coupled Semiconductor Devices. *Bell System Technical Journal*, 49(4):587–593, April 1970.

[4] D. E. Carlson and C. R. Wronski. Amorphous silicon solar cell. *Applied Physics Letters*, 28(11):671, 1976.

[5] Technik GalaxyS5. http://www.samsung.com/de/microsite/galaxys5/technische-daten.html, accessed 12.08.2014.

[6] H. Sirringhaus, T. Kawase, R. H. Friend, T. Shimoda, M. Inbasekaran, W. Wu, and E. P. Woo. High-Resolution Inkjet Printing of All-Polymer Transistor Circuits. *Science*, 290(5499):2123–2126, December 2000.

[7] F. C. Krebs, S. A. Gevorgyan, and J. Alstrup. A roll-to-roll process to flexible polymer solar cells: model studies, manufacture and operational stability studies. *Journal of Materials Chemistry*, 19(30):5442, 2009.

[8] B. Li, L. Wang, B. Kang, P. Wang, and Y. Qiu. Review of recent progress in solid-state dye-sensitized solar cells. *Solar Energy Materials and Solar Cells*, 90(5):549–573, March 2006.

[9] M. B. Smith and J. Michl. Singlet Fission. *Chemical Reviews*, 110(11):6891–936, November 2010.

[10] C. E. Swenberg and W. T. Stacy. Bimolecular radiationless transitions in crystalline tetracene. *Chemical Physics Letters*, 2(5):327–328, September 1968.

[11] E. J. Bowen, E. Mikiewicz, and F. W. Smith. Resonance Transfer of Electronic Energy in Organic Crystals. *Proceedings of the Physical Society. Section A*, 62(1):26–31, January 1949.

[12] A. S. Davydov. The Theory of Molecular Excitons. *Soviet Physics Uspekhi*, 7(2):145–178, February 1964.

[13] H. Haug and S. W. Koch. *Quantum Theory of the Optical and Electronic Properties of Semiconductors.* World Scientific, 4 edition, 2009.

[14] P. Y. Yu and M. Cardona. *Fundamentals of Semiconductors.* Springer Heidelberg, 2. edition, 1999.

[15] W. Barford. *Electronic and Optical Properties of Conjugated Polymers (International Series of Monographs on Physics).* Oxford University Press, USA, 2005.

[16] I. V. Hertel and C.-P. Schulz. *Atome, Moleküle und optische Physik.* Springer Heidelberg, 1. edition, 2010.

[17] C. Klingshirn. *Semiconductor Optics.* Springer Berlin Heidelberg, 3 edition, 2007.

[18] Wikpedia, Aromaticity, http://en.wikipedia.org/wiki/Aromaticity, accessed 20.06.2014.

[19] F. C. Spano. The spectral signatures of Frenkel polarons in H- and J-aggregates. *Accounts of chemical research*, 43(3):429–39, March 2010.

[20] T. Breuer, M. A. Celik, P. Jakob, R. Tonner, and G. Witte. Vibrational Davydov Splittings and Collective Mode Polarizations in Oriented Organic Semiconductor Crystals. *The Journal of Physical Chemistry C*, 116(27):14491–14503, July 2012.

[21] S. Sharifzadeh, P. Darancet, L. Kronik, and J. B. Neaton. Low-Energy Charge-Transfer Excitons in Organic Solids from First-Principles: The Case of Pentacene. *The Journal of Physical Chemistry Letters*, 4(13):2197–2201, July 2013.

[22] C. D. Spataru, S. Ismail-Beigi, R. B. Capaz, and S. G. Louie. Quasiparticle and Excitonic Effects in the Optical Response of Nanotubes and Nanoribbons. In *Topics in Applied Physics: Carbon Nanotubes*, volume 227, pages 195–227. Springer Berlin Heidelberg, 2008.

[23] Sahar Sharifzadeh, Ariel Biller, Leeor Kronik, and Jeffrey B. Neaton. Quasiparticle and optical spectroscopy of the organic semiconductors pentacene and PTCDA from first principles. *Physical Review B*, 85(12):125307, March 2012.

[24] M. Rohlfing and S. G. Louie. Electron-hole excitations and optical spectra from first principles. *Physical Review B*, 62(8):4927–4944, August 2000.

[25] W. Kohn and L. J. Sham. Self-Consistent Equations Including Exchange and Correlation Effects. *Physical Review*, 140(4A):A1133–A1138, November 1965.

[26] L. Hedin. New Method for Calculating the One-Particle Green's Function with Application to the Electron-Gas Problem. *Physical Review*, 139(3A):A796–A823, August 1965.

[27] M. C. Payne, T. A. Arias, and J. D. Joannopoulos. Iterative minimization techniques for ab initio total-energy calculations: molecular dynamics and conjugate gradients. *Reviews of Modern Physics*, 64(4):1045–1097, October 1992.

[28] N. Peyghambarian, S.W. Koch, and A. Mysyrowicz. *Introduction to Semiconductor Optics*. Prentice Hall, New Jersey, 1 edition, 1993.

[29] Pierluigi Cudazzo, Matteo Gatti, and Angel Rubio. Excitons in molecular crystals from first-principles many-body perturbation theory: Picene versus pentacene. *Physical Review B*, 86(19):195307, November 2012.

[30] A. Rinn. *Excitonic and excimeric features in monomeric and dimeric perylene crystals*. Master thesis, Philipps-Universität Marburg, 2013.

[31] J. H. Lambert. *Photometria sive de mensura et gradibus luminis, colorum et umbrae.* Eberhardt Klett, Augsburg, Germany, 1760.

[32] A. Beer. Bestimmung der Absorption des rothen Lichts in farbigen Flüssigkeiten. *Annalen der Physik und Chemie*, 86:78–88, 1852.

[33] J. Mooney and P. Kambhampati. Get the Basics Right: Jacobian Conversion of Wavelength and Energy Scales for Quantitative Analysis of Emission Spectra. *The Journal of Physical Chemistry Letters*, 4(19):3316–3318, October 2013.

[34] G. Weiser. Private Communication.

[35] M. Kira and S.W. Koch. *Semiconductor Quantum Optics.* Cambridge University Press, 1 edition, 2012.

[36] R. Binder, S. Koch, M. Lindberg, W. Schäfer, and F. Jahnke. Transient many-body effects in the semiconductor optical Stark effect: A numerical study. *Physical Review B*, 43(8):6520–6529, March 1991.

[37] C. Sieh, T. Meier, F. Jahnke, A. Knorr, S. W. Koch, P. Brick, M. Hübner, C. Ell, J. Prineas, G. Khitrova, and H. Gibbs. Coulomb Memory Signatures in the Excitonic Optical Stark Effect. *Physical Review Letters*, 82(15):3112–3115, April 1999.

[38] N. S. Köster, K. Kolata, R. Woscholski, C. Lange, G. Isella, D. Chrastina, H. von Känel, and S. Chatterjee. Giant dynamical Stark shift in germanium quantum wells. *Applied Physics Letters*, 98(16):161103, 2011.

[39] F. Träger, editor. *Lasers and Optics.* Springer, New York, 2007.

[40] M. B. Panish and H. C. Casey Jr. Temperature Dependence of the Energy Gap in GaAs and GaP. *Journal of Applied Physics*, 40(1):163, 1969.

[41] H. Haken and H. C. Wolf. *Molekülphysik und Quantenchemie.* Springer, 3. edition, 1998.

[42] M. C. R. Delgado, K. R. Pigg, D. A. da Silva Filho, N. E. Gruhn, Y. Sakamoto, T. Suzuki, R. M. Osuna, J. Casado, V. Hernández, J. T. L. Navarrete, N. G. Martinelli, J. Cornil, R. S. Sánchez-Carrera, V. Coropceanu, and J.-L. Brédas. Impact of perfluorination on the charge-transport parameters of oligoacene crystals. *Journal of the American Chemical Society*, 131(4):1502–12, February 2009.

[43] Y. Sakamoto, T. Suzuki, M. Kobayashi, Y. Gao, Y. Fukai, Y. Inoue, F. Sato, and S. Tokito. Perfluoropentacene: high-performance p-n junctions and complementary circuits with pentacene. *Journal of the American Chemical Society*, 126(26):8138–8140, July 2004.

[44] K. P. C. Vollhardt and N. E. Schore. *Organische Chemie*. Wiley-VCH Verlag GmbH, 4 edition, 2005.

[45] N. Kraus. *Absorptionsmessungen organischer Moleküle in der Gasphase*. Examensarbeit, Philipps-Universität Marburg, 2014.

[46] A. Hinderhofer, U. Heinemeyer, A. Gerlach, S. Kowarik, R. M. J. Jacobs, Y. Sakamoto, T. Suzuki, and F. Schreiber. Optical properties of pentacene and perfluoropentacene thin films. *The Journal of chemical physics*, 127(19):194705, November 2007.

[47] X. Zhang, Q.-S. Li, Y. Xie, and H. F. Schaefer. The lowest triplet electronic states of polyacenes and perfluoropolyacenes. *Molecular Physics*, 105(19-22):2743–2752, October 2007.

[48] F. Anger, J. O. Osso, U. Heinemeyer, K. Broch, R. Scholz, A. Gerlach, and F. Schreiber. Photoluminescence spectroscopy of pure pentacene, perfluoropentacene, and mixed thin films. *The Journal of chemical physics*, 136(5):054701, February 2012.

[49] M. Rei Vilar, M. Heyman, and M Schott. Spectroscopy of low-energy electrons backscattered from an organic solid surface: pentacene. *Chemical Physics Letters*, 94(5):522–526, February 1983.

[50] R. E. Smalley, L. Wharton, and D. H. Levy. Molecular optical spectroscopy with supersonic beams and jets. *Accounts of Chemical Research*, 10(4):139–145, April 1977.

[51] E. D. Becker and G. C. Pimentel. Spectroscopic Studies of Reactive Molecules by the Matrix Isolation Method. *The Journal of Chemical Physics*, 25(2):224, 1956.

[52] J. K. Trautman, J. J. Macklin, L. E. Brus, and E. Betzig. Near-field spectroscopy of single molecules at room temperature. *Nature*, 369(6475):40–42, May 1994.

[53] A. T. Amos and B. L. Burrows. *Advances in Quantum Chemistry.* Elsevier Science, 7 edition, 1973.

[54] N. S. Bayliss and E. G. McRae. Solvent Effects in Organic Spectra: Dipole Forces and the Franck-Condon Principle. *The Journal of Physical Chemistry*, 58(11):1002–1006, November 1954.

[55] S. Kera, S. Hosoumi, K. Sato, H. Fukagawa, S.-i. Nagamatsu, Y. Sakamoto, T. Suzuki, H. Huang, W. Chen, A. T. S. Wee, V. Coropceanu, and N. Ueno. Experimental Reorganization Energies of Pentacene and Perfluoropentacene: Effects of Perfluorination. *The Journal of Physical Chemistry C*, 117(43):22428–22437, October 2013.

[56] T. Breuer and G. Witte. Epitaxial growth of perfluoropentacene films with predefined molecular orientation: A route for single-crystal optical studies. *Physical Review B*, 83(15):155428, April 2011.

[57] K. Hummer and C. Ambrosch-Draxl. Electronic properties of oligoacenes from first principles. *Physical Review B*, 72(20):205205, November 2005.

[58] H. Yamagata, J. Norton, E. Hontz, Y. Olivier, D. Beljonne, J. L. Brédas, R. J. Silbey, and F. C. Spano. The nature of singlet excitons in oligoacene molecular crystals. *The Journal of chemical physics*, 134(20):204703, May 2011.

[59] Murilo Tiago, John Northrup, and Steven Louie. Ab initio calculation of the electronic and optical properties of solid pentacene. *Physical Review B*, 67(11):115212, March 2003.

[60] L. Sebastian, G. Weiser, and H. Bässler. Charge transfer transitions in solid tetracene and pentacene studied by electroabsorption. *Chemical Physics*, 61(1-2):125–135, October 1981.

[61] J. Helzel, S. Jankowski, M. El Helou, G. Witte, and W. Heimbrodt. Temperature dependent optical properties of pentacene films on zinc oxide. *Applied Physics Letters*, 99(21):211102, 2011.

[62] K. Hannewald, V. Stojanović, J. Schellekens, P. Bobbert, G. Kresse, and J. Hafner. Theory of polaron bandwidth narrowing in organic molecular crystals. *Physical Review B*, 69(7):075211, February 2004.

[63] W. Shockley and H. J. Queisser. Detailed Balance Limit of Efficiency of p-n Junction Solar Cells. *Journal of Applied Physics*, 32(3):510, 1961.

[64] P. W. Atkins. *Physikalische Chemie*. Oxford University Press, 3 edition, 1987.

[65] Ch. K. Rhodes, editor. *Excimer Lasers (Topics in Applied Physics)*. Springer, 1979.

[66] J. S. Cohen. Ground and excited states of Ne2 and Ne2+. I. Potential curves with and without spin-orbit coupling. *The Journal of Chemical Physics*, 61(8):3230, 1974.

[67] B. Schneider. Ground and excited states of Ne2 and Ne[sub 2][sup +]. II. Spectroscopic properties and radiative lifetimes. *The Journal of Chemical Physics*, 61(8):3240, 1974.

[68] T. H. Dunning and P. J. Hay. Electronic states of KrF. *Applied Physics Letters*, 28(11):649, 1976.

[69] Th. Förster and K. Kasper. Ein Konzentrationsumschlag der Fluoreszenz. *Zeitschrift für Physikalische Chemie*, 1(5_6):275–277, June 1954.

[70] B. Stevens and E. Hutton. Radiative Life-time of the Pyrene Dimer and the Possible Role of Excited Dimers in Energy Transfer Processes. *Nature*, 186(4730):1045–1046, June 1960.

[71] B. Stevens. Evidence for the Photo-Association of Aromatic Hydrocarbons in Fluid Media. *Nature*, 192(4804):725–727, November 1961.

[72] S. Shirai, S. Iwata, T. Tani, and S. Inagaki. Ab initio studies of aromatic excimers using multiconfiguration quasi-degenerate perturbation theory. *The journal of physical chemistry. A*, 115(26):7687–99, July 2011.

[73] H. Auweter, D. Ramer, B. Kunze, and H. C. Wolf. The dynamics of excimer formation in perylene crystals. *Chemical Physics Letters*, 85(3):325–329, January 1982.

[74] Holger Pröhl. *Optische Eigenschaften ultradünner PTCDA & TiOPc Einzel- und Heteroschichten*. Dissertation, TU Dresden, 2006.

[75] A. Furube, M. Murai, Y. Tamaki, S. Watanabe, and R. Katoh. Effect of aggregation on the excited-state electronic structure of perylene studied by transient absorption spectroscopy. *The journal of physical chemistry. A*, 110(20):6465–71, May 2006.

[76] B. Walker, H. Port, and H. C. Wolf. The two-step excimer formation in perylene crystals. *Chemical Physics*, 92(2-3):177–185, January 1985.

[77] E. v. Freydorf, J. Kinder, and M. E. Michel-Beyerle. On low temperature fluorescence of perylene crystals. *Chemical Physics*, 27(2):199–209, January 1978.

[78] K. O. Lee and T. T. Gan. Influence of substrate temperature on the optical properties of evaporated films of pentacene. *Chemical Physics Letters*, 51(1):120–124, October 1977.

[79] J. Burgos, M. Pope, Ch. E. Swenberg, and R. R. Alfano. Heterofission in pentacene-doped tetracene single crystals. *Physica Status Solidi (b)*, 83(1):249–256, September 1977.

[80] M. Schwoerer and H. C. Wolf. *Organic Molecular Solids*. Wiley-VCH Verlag GmbH, 2007.

[81] J. B. Birks, T. A. King, and I. H. Munro. The Photoluminescence Decay of Organic Crystals. *Proceedings of the Physical Society*, 80(2):355–361, August 1962.

[82] G. T. Wright. Absolute Quantum Efficiency of Photofluorescence of Anthracene Crystals. *Proceedings of the Physical Society. Section B*, 68(4):241–248, April 1955.

[83] A. Hammer and H. C. Wolf. Die Quantenausbeute der Fluoreszenz von Naphthalin-Kristallen. *physica status solidi (b)*, 33(1):K25–K28, 1969.

[84] I. B. Berlman. *Handbook of fluorescence spectra of aromatic molecules*. Academic Press, 1965.

[85] N. Geacintov, M. Pope, and F. Vogel. Effect of Magnetic Field on the Fluorescence of Tetracene Crystals: Exciton Fission. *Physical Review Letters*, 22(12):593–596, March 1969.

[86] A. A. Kazzaz and A. B. Zahlan. Temperature Dependence of Crystalline Tetracene Fluorescence. *The Journal of Chemical Physics*, 48(3):1242, 1968.

[87] L. D. A. Siebbeles. Organic solar cells: Two electrons from one photon. *Nature chemistry*, 2(8):608–9, August 2010.

[88] C. Jundt, G. Klein, B. Sipp, J. Le Moigne, M. Joucla, and A. A. Villaeys. Exciton dynamics in pentacene thin films studied by pump-probe spectroscopy. *Chemical Physics Letters*, 241(1-2):84–88, July 1995.

[89] W.-L. Chan, M. Ligges, A. Jailaubekov, L. Kaake, L. Miaja-Avila, and X.-Y. Zhu. Observing the multiexciton state in singlet fission and ensuing ultrafast multielectron transfer. *Science (New York, N.Y.)*, 334(6062):1541–5, December 2011.

[90] M. B. Smith and J. Michl. Recent advances in singlet fission. *Annual review of physical chemistry*, 64:361–386, January 2013.

[91] R. E. Merrifield. Theory of Magnetic Field Effects on the Mutual Annihilation of Triplet Excitons. *The Journal of Chemical Physics*, 48(9):4318, 1968.

[92] R. Kepler, J. Caris, P. Avakian, and E. Abramson. Triplet excitons and Delayed Fluorescence in Anthracene Crystals. *Physical Review Letters*, 10(9):400–402, May 1963.

[93] R. C. Johnson, R. E. Merrifield, P. Avakian, and R. B. Flippen. Effects of Magnetic Fields on the Mutual Annihilation of Triplet Excitons in Molecular Crystals. *Physical Review Letters*, 19(6):285–287, August 1967.

[94] R. P. Groff, R. E. Merrifield, and P. Avakian. Singlet and triplet channels for triplet-exciton fusion in anthracene crystals. *Chemical Physics Letters*, 5(3):168–170, March 1970.

[95] R. A. Keller. Excited triplet singlet intersystem crossing. *Chemical Physics Letters*, 3(1):27–29, January 1969.

[96] A. Rao, M. W. B. Wilson, J. M. Hodgkiss, S. Albert-Seifried, H. Bässler, and R. H. Friend. Exciton fission and charge generation via triplet excitons in pentacene/C60 bilayers. *Journal of the American Chemical Society*, 132(36):12698–703, September 2010.

[97] W. T. Pollard, S.-Y. Lee, and R. A. Mathies. Wave packet theory of dynamic absorption spectra in femtosecond pump probe experiments. *The Journal of Chemical Physics*, 92(7):4012, 1990.

[98] D. Polli, P. Altoè, O. Weingart, K. M. Spillane, C. Manzoni, D. Brida, G. Tomasello, G. Orlandi, P. Kukura, R. A. Mathies, M. Garavelli, and G. Cerullo. Conical intersection dynamics of the primary photoisomerization event in vision. *Nature*, 467(7314):440–3, September 2010.

[99] A. Chernikov, S. Schäfer, M. Koch, S. Chatterjee, B. Laumer, and M. Eickhoff. Probing carrier populations in ZnO quantum wells by screening of the internal electric fields. *Physical Review B*, 87(3):035309, January 2013.

[100] U. Fano. Effects of Configuration Interaction on Intensities and Phase Shifts. *Physical Review*, 124(6):1866–1878, December 1961.

[101] M. Pabst, B. Lunkenheimer, and A. Köhn. The Triplet Excimer of Naphthalene: A Model System for Triplet-Triplet Interactions and Its Spectral Properties. *The Journal of Physical Chemistry C*, 115(16):8335–8344, April 2011.

[102] Henning Marciniak, Igor Pugliesi, Bert Nickel, and Stefan Lochbrunner. Ultrafast singlet and triplet dynamics in microcrystalline pentacene films. *Physical Review B*, 79(23):1–8, June 2009.

[103] Paul M Zimmerman, Zhiyong Zhang, and Charles B Musgrave. Singlet fission in pentacene through multi-exciton quantum states. *Nature chemistry*, 2(8):648–52, August 2010.

[104] B. J. Walker, A. J. Musser, D. Beljonne, and R. H. Friend. Singlet exciton fission in solution. *Nature chemistry*, 5(12):1019–1024, December 2013.

[105] T. S. Kuhlman, J. Kongsted, K. V. Mikkelsen, K. B. Mø ller, and T. I. Sø lling. Interpretation of the ultrafast photoinduced processes in pentacene thin films. *Journal of the American Chemical Society*, 132(10):3431–3439, March 2010.

[106] C. Lange, G. Isella, D. Chrastina, F. Pezzoli, N. Köster, R. Woscholski, and S. Chatterjee. Spin band-gap renormalization and hole spin dynamics in Ge/SiGe quantum wells. *Physical Review B*, 85(24):1–5, June 2012.

[107] U. Bockelmann and G. Bastard. Interband absorption in quantum wires. I. Zero-magnetic-field case. *Physical Review B*, 45(4):1688–1699, January 1992.

[108] C. Lange, N. S. Köster, S. Chatterjee, H. Sigg, D. Chrastina, G. Isella, H. von Känel, M. Schäfer, M. Kira, and S. W. Koch. Ultrafast nonlinear optical response of photoexcited Ge/SiGe quantum wells: Evidence for a femtosecond transient population inversion. *Physical Review B*, 79(20):1–4, May 2009.

[109] J. Liu, X. Sun, R. E. Camacho-Aguilera, L. C. Kimerling, and J. Michel. Ge-on-Si laser operating at room temperature. *Optics letters*, 35(5):679–81, March 2010.

[110] P. Chaisakul, D. Marris-Morini, G. Isella, D. Chrastina, N. Izard, X. Le Roux, S. Edmond, J.-R. Coudevylle, and L. Vivien. Room temperature direct gap electroluminescence from Ge/Si0.15Ge0.85 multiple quantum well waveguide. *Applied Physics Letters*, 99(14):141106, 2011.

[111] Y.-H. Kuo, Y. K. Lee, Y. Ge, S. Ren, J. E. Roth, T. I. Kamins, D. A. B. Miller, and J. S. Harris. Strong quantum-confined Stark effect in germanium quantum-well structures on silicon. *Nature*, 437(7063):1334–6, October 2005.

[112] R. E. Camacho-Aguilera, Y. Cai, N. Patel, J. T. Bessette, M. Romagnoli, L. C. Kimerling, and J. Michel. An electrically pumped germanium laser. *Optics Express*, 20(10):11316–11320, 2012.

[113] L. Schultheis, J. Kuhl, A. Honold, and C. Tu. Ultrafast Phase Relaxation of Excitons via Exciton-Exciton and Exciton-Electron Collisions. *Physical Review Letters*, 57(13):1635–1638, September 1986.

[114] E. Göbel, K. Leo, T. Damen, J. Shah, S. Schmitt-Rink, W. Schäfer, J. Müller, and K. Köhler. Quantum beats of excitons in quantum wells. *Physical Review Letters*, 64(15):1801–1804, April 1990.

[115] D.-S. Kim, J. Shah, J. Cunningham, T. Damen, W. Schäfer, M. Hartmann, and S. Schmitt-Rink. Giant excitonic resonance in time-resolved four-wave mixing in quantum wells. *Physical Review Letters*, 68(7):1006–1009, February 1992.

[116] H. Wang, K. Ferrio, D. Steel, Y. Hu, R. Binder, and S. W. Koch. Transient nonlinear optical response from excitation induced dephasing in GaAs. *Physical Review Letters*, 71(8):1261–1264, August 1993.

[117] Q. Vu, H. Haug, W. Hügel, S. Chatterjee, and M. Wegener. Signature of Electron-Plasmon Quantum Kinetics in GaAs. *Physical Review Letters*, 85(16):3508–3511, October 2000.

[118] T. Rappen, U. Peter, M. Wegener, and W. Schäfer. Coherent dynamics of continuum and exciton states studied by spectrally resolved fs four-wave mixing. *Physical Review B*, 48(7):4879–4882, August 1993.

[119] T. Rappen, U.-G. Peter, M. Wegener, and W. Schäfer. Polarization dependence of dephasing processes: A probe for many-body effects. *Physical Review B*, 49(15):10774–10777, April 1994.

[120] J. Shah. *Ultrafast Spectroscopy of Semiconductors and Semiconductor Nanostructures*. Springer Berlin Heidelberg, 1996.

[121] M Joffre, D Hulin, a Migus, a Antonetti, C Benoit à la Guillaume, N Peyghambarian, M Lindberg, and S W Koch. Coherent effects in pump-probe spectroscopy of excitons. *Optics letters*, 13(4):276–8, April 1988.

[122] M. Lindberg and S. W. Koch. Effective Bloch equations for semiconductors. *Physical Review B*, 38(5):3342–3350, August 1988.

[123] S. W. Koch, N. Peyghambarian, and M. Lindberg. Transient and steady-state optical nonlinearities in semiconductors. *Journal of Physics C: Solid State Physics*, 21(30):5229–5249, October 1988.

[124] K. Kolata, N. S. Köster, A. Chernikov, M. J. Drexler, E. Gatti, S. Cecci, D. Chrastina, G. Isella, M. Guzzi, and S. Chatterjee. Dephasing in Ge/SiGe quantum wells measured by means of coherent oscillations. *Physical Review B*, 86(20):201303, November 2012.

[125] C. Lange, N. S. Köster, S. Chatterjee, H. Sigg, D. Chrastina, G. Isella, H. von Känel, B. Kunert, and W. Stolz. Comparison of ultrafast carrier thermalization in GaInAs and Ge quantum wells. *Physical Review B*, 81(4):1–6, January 2010.

[126] S. Tsujino, H. Sigg, G. Mussler, D. Chrastina, and H. von Känel. Photocurrent and transmission spectroscopy of direct-gap interband transitions in Ge/SiGe quantum wells. *Applied Physics Letters*, 89(26):262119, 2006.

[127] E. Gatti, E. Grilli, M. Guzzi, D. Chrastina, G. Isella, a. Chernikov, V. Bornwasser, N. Köster, R. Woscholski, and S. Chatterjee. Photoluminescence and ultrafast intersubband relaxation in Ge/SiGe multiple quantum wells. *Physical Review B*, 84(24):1–5, December 2011.

[128] G. Sun, L. Friedman, and R. Soref. Light-hole to heavy-hole acoustic phonon scattering rate. *Physical Review B*, 62(12):8114–8119, September 2000.

[129] S. Rudin, T. Reinecke, and B. Segall. Temperature-dependent exciton linewidths in semiconductors. *Physical Review B*, 42(17):11218–11231, December 1990.

[130] A. Giorgioni, E. Gatti, E. Grilli, A. Chernikov, S. Chatterjee, D. Chrastina, G. Isella, and M. Guzzi. Photoluminescence decay of direct and indirect transitions in Ge/SiGe multiple quantum wells. *Journal of Applied Physics*, 111(1):013501, 2012.

[131] U. Brosa. Diffraction of Electromagnetic Waves. *arXiv:0911.3663v2*, November 2009.

[132] I. Salzmann, A. Moser, M. Oehzelt, T. Breuer, X. Feng, Z.-Y. Juang, D. Nabok, R. G. Della Valle, S. Duhm, G. Heimel, A. Brillante, E. Venuti, I. Bilotti, C. Christodoulou, J. Frisch, P. Puschnig, C. Draxl, G. Witte, K. Müllen, and N. Koch. Epitaxial growth of π-stacked perfluoropentacene on graphene-coated quartz. *ACS nano*, 6(12):10874–83, December 2012.

Veröffentlichungen

- *Molecular packing determines singlet exciton fission in organic semiconductors*
  K. Kolata, T. Breuer, G. Witte and S. Chatterjee
  ACS Nano, 2014, 8 (7), pp. 7377-7383

- *Holes in germanium quantum wells: spin relaxation and temperature dynamics*
  K. Kolata, N. S. Köster, R. Woscholski, S. Imhof, A. Thränhardt, C. Lange, J. E. Sipe, F. Pezzoli, S. Cecchi, D. Chrastina, G. Isella, S. Chatterjee
  Phys. Stat. Sol. (c), 2013, 10 (9), pp. 1238-1241

- Dephasing in Ge/SiGe quantum wells measured by means of coherent oscillations
  K. Kolata, N. S. Köster, A. Chernikov, M. J. Drexler, E. Gatti, S. Cecci, D. Chrastina, G. Isella, M. Guzzi, S. Chatterjee
  Phys. Rev. B, 2012, 86 (20), pp. 201303

- *Hole system heating by ultrafast interband energy transfer in optically excited Ge/SiGe quantum wells*
  K. Kolata, S. Imhof, N. S. Köster, S. Cecchi, D. Chrastina, G. Isella, J. E. Sipe, A. Thränhardt and S. Chatterjee
  Phys. Rev. B, 2012, 85, pp. 165312

- *Temperature and pump power dependent photoluminescence characterization of MBE grown GaAsBi on GaAs*
  N. A. Riordan, C. Gogineni, S. R. Johnson, X. Lu, T. Tiedje, D. Ding, Y.-H. Zhang, R. Fritz, K. Kolata, S. Chatterjee, K. Volz, S. W. Koch
  Journal of Materials Science: Materials in Electronics, 23 (10), pp. 1799-1804

- *Giant dynamical Stark shift in germanium quantum wells*
  N. S. Köster, K. Kolata, R. Woscholski, C. Lange, G. Isella, D. Chrastina, H. v. Känel and S. Chatterjee
  Appl. Phys. Lett., 2011, 98, pp. 161103

- *Ultrafast transient gain in Ge/SiGe quantum wells*
  N. S. Köster, C. Lange, K. Kolata, S. Chatterjee, D. Chrastina, G. Isella, H. v. Känel, H. Sigg, M. Schäfer, M. Kira and S. W. Koch
  Phys. Stat. Sol. (c), 2011, 8, pp. 1109-1112

- *Evidence of two disorder scales in Ga(AsBi)*
  S. Imhof, C. Wagner, A. Chernikov, M. Koch, K. Kolata, N. S. Köster, S. Chatterjee, S. W. Koch, X. Lu, S. R. Johnson, D. A. Beaton, T. Tiedje, O. Rubel and A. Thränhardt
  Phys. Stat. Sol. (b), 2011, 248, pp. 851-854

- *Clustering effects in Ga(AsBi)*
  S. Imhof, A. Thränhardt, A. Chernikov, M. Koch, N. S. Köster, K. Kolata, S. Chatterjee, S. W. Koch, X. Lu, S. R. Johnson, D. A. Beaton, T. Tiedje and O. Rubel
  Appl. Phys. Lett., 2010, 96 (13), pp. 131115

Danksagung

„Deo Gratias“

Es wird gesagt, dass irgendwann auch die schönste Zeit vorbeigeht. Das Gute ist, man weiß erst ganz am Ende, was die schönste Zeit war. Dennoch kann ich bereits jetzt sagen, dass meine Promotionszeit sowohl eines der größten Geschenke, als auch eines der größten Herausforderungen war. Von daher gilt mein erster Dank selbstverständlich der Person, die mir diese einzigartige Erfahrung ermöglicht hat: PD Dr. Sangam Chatterjee. Ganz so, wie bei der Nationalhymne eines längst verflossenen Staates war es nicht, aber bei seinen Qualitäten hätte sich sicherlich auch der Größte noch etwas abgucken können. Seine unnachahmliche Art, auch die schwierigsten Situationen zu meistern, und den Fokus, in jeder Situation, auf das Wesentliche zu richten, haben einen nie aufstecken lassen. Danke für alles.

Prof. X. Y. Zhu pflegt zu sagen, *„It's all about the sample“*. Dem kann ich mich uneingeschränkt anschließen. Deswegen geht mein zweiter Dank an Tobias Breuer und Prof. Gregor Witte. Ohne die einzigartigen PFP Proben würde ich vielleicht heute mit Licht auf Fische schießen, oder auf Unkraut, oder auf Bierdeckel und mich bis heute Fragen, was ich eigentlich nach der Einleitung in meine Arbeit schreiben soll.

Einer der bekanntesten Physiker, Isaac Newton, wußte, wo er sich zu bedanken hatte: *„Wenn ich weiter sehen konnte, so deshalb, weil ich auf den Schultern von Riesen stand.“*. Ob ich jemals die Schultern erreichte, vermag ich nicht zu urteilen, aber sie brachten mir das Sehen bei: Niko Köster, Alexey Chernikov, Benjamin Ewers und Kapil Kohli.

Ein großer Dank geht auch an Nils Rosemann, Michael Drexler, Jan Kuhnert, Niklas Krauth, Andre Rinn, Thomas Ahlich und Robin Döring, die mich, wenn immer nötig, tatkräftig unterstützten und so manch experimentell enttäuschenden Labortag mit spannenden Debatten würzten.
Ein besonderer Dank gilt den Leuten, die nach Benjamin *„etwas Richtiges gelernt haben“*. Das ist allen voran unser Techniker Rüdiger Rink, der immer zwei offene Ohren hatte, wenn es mal wieder klemmte. Nicht zu vergessen sind die Elektronik- und die Feinmechanikwerkstatt, für die immer gilt *„Yes we can!“*.
Meinem Bruder und meinen Eltern danke ich für die bedingungslose Unterstützung und die allzeit geöffnete Pforte. Jede Zusammenkunft ist für mich ein Ereignis.
Mein größter Dank gilt meiner Frau Phaedra. Sie weiß, dass die Promotion für mich vor allem eine große Herausforderung war. Ohne deine Liebe, deine Ausdauer und deinem motivierenden *„Ganbatte!“* wäre das hier nicht möglich gewesen.
Te amaré por siempre.

„That’s all Folks!“